Bone Adaptation: Roles of Fluid Flow and Pore Pressure

A Thesis Submitted
In Partial Fulfillment of the Requirements
for the Degree of

DOCTOR OF PHILOSOPHY

by

"Sanjay Singh" (2017MEZ0012)



DEPARTMENT OF MECHANICAL ENGINEERING INDIAN INSTITUTE OF TECHNOLOGY ROPAR

October, 2024

Sanjay Singh: Bone Adaptation: Roles of Fluid Flow and Pore pressure

Copyright © 2024, Indian Institute of Technology Ropar

All Rights Reserved

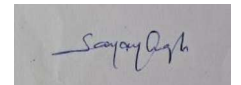
DEDICATED

TO

Aarya S Chaudhary

Declaration of Originality

I hereby declare that the work which is being presented in the thesis entitled **Bone Adaptation**: Role of Fluid Flow and Pore Pressure has been solely authored by me. It presents the result of my own independent investigation/research conducted during the time period from August 2017 to April 2024. Thesis submission under the supervision of Dr. Satwinder Jit Singh, Assistant Professor, Department of Mechanical Engineering, Indian Institute of Technology, Ropar, and Dr Jitendra Prasad, Associate Professor, Department of Mechanical Engineering, Indian Institute of Technology, Ropar. To the best of my knowledge, it is an original work, both in terms of research content and narrative, and has not been submitted or accepted elsewhere, in part or in full, for the award of any degree, diploma, fellowship, associateship, or similar title of any university or institution. Further, due credit has been attributed to the relevant state-of-the-art collaborations (if any) with appropriate citations acknowledgments in line with established ethical norms and practices. I also declare that any idea/data/fact/source stated in my thesis has not been fabricated/falsified/misrepresented. All the principles of academic honesty and integrity have been followed. I fully understand that if the thesis is found to be unoriginal, fabricated, or plagiarized, the Institute reserves the right to withdraw the thesis from its archive and revoke the associated degree conferred. Additionally, the Institute also reserves the right to appraise all concerned sections of society of the matter for their information and necessary action (if any). If accepted, I hereby consent for my thesis to be available online in the Institute's Open Access repository, inter-library loan, and the title & abstract to be made available to outside organizations.



Signature

Name: Sanjay Singh

Entry Number: 2017MEZ0012

Program: PhD

Department: Mechanical Engineering
Indian Institute of Technology Ropar

Rupnagar, Punjab 140001

Date: 1th October 2024

Acknowledgments

Earning a doctorate and writing a dissertation is long and undoubtedly not done single-handedly. I consider myself incredibly fortunate to be surrounded by the great people around me who encouraged me and helped me throughout my PhD journey.

First and foremost, I want to extend my gratitude to everyone at the Biomechanical Creativity and Innovation Lab. Dr. Subham Badhiyal, Dr. Chander Sen, Dr. Ajay Goyal, Himanshu Shekhar, and Gagan Chaudhary, your patience, assistance, and the fun I had with you all for the last six and half years have been valuable. Each of you has listened to me during the highs and lows of my Ph.D. journey, and I am very grateful for that. While I know these gestures cannot be fully repaid, I hope to be there for each of you in your time of need.

I pay my sincere and heartfelt appreciation to my research supervisors, Dr. Jitendra Prasad and Dr Satwinder Jit Singh: your unwavering persistence and commitment to nurturing free thinking have played an instrumental role in my growth as a researcher. Without your guidance, support, and motivation, this Ph.D. research work may not be possible. Your vision, honesty, and enthusiasm have deeply influenced me. I will forever admire your logical and optimistic approach to word mentorship.

Thank you for your time and guidance to my doctoral committee, Dr. Navin Kumar, Dr. Srikant Sekhar Padhee, Dr. Anshu Dhar Jayal, and Dr. Nirmal Raj Gopinathan. Everyone has their fingerprints on this work, which is much better than I hoped. I am also thankful to Indian Institute of technology Ropar for providing me with the resources and facilities necessary for conducting my research.

Above all, I must thank my wife, Monica Singhal; this dissertation has only been made possible through your selflessness and support. Thank you for sharing your life with me. I hope I have made you proud.

The part of the figures in Chapter 1 (bone anatomy and cells) were adapted from Server Medical Art (Servier; https://smart.servier.com/), licensed under a Creative Commons Attribute 4.0 Unported Licence.

Sanjay Singh

October 2024

Certificate

This is to certify that the thesis entitled **Bone Adaptation: Role of Fluid Flow and Pore Pressure**, submitted by **Sanjay Singh (2017mez0012)** for the award of the degree of **Doctor of Philosophy** of Indian Institute of Technology Ropar, is a record of bonafide research work carried out under my (our) guidance and supervision. To the best of my knowledge and belief, the work presented in this thesis is original and has not been submitted, either in part or full, for the award of any other degree, diploma, fellowship, associateship, or similar title of any university or institution.

In my (our) opinion, the thesis has reached the standard of fulfilling the requirements of the regulations relating to the degree.

Signature of the Supervisor

Dr. Satwinder Jit Singh

Department of Mechanical Engineering

Indian Institute of Technology Ropar

Rupnagar, Punjab 140001

Date: 1th October 2024

H

Signature of the Supervisor

Dr. Jitendra Prasad

Department of Mechanical Engineering

Indian Institute of Technology Ropar

Rupnagar, Punjab 140001

Date: 1th October 2024

Lay Summary

Bone loss is a big problem, especially as people age or cannot correctly use their muscles and bones. As the bone gets weaker, they are more likely to break. There are many reasons why bone starts to weaken; however, the most likely one is not moving around enough, i.e., loss of mechanical environment.

Researchers have found that fluid flows through tiny channels in our bones when we move, which helps keep our bones strong. Similarly, they also notice that pressure is created in tiny channels inside the bone during the movement, which might keep our bone strong. However, how these things work together to keep our bones healthy is unclear.

This study intended to determine how fluid flow and pore pressure affect bone health. We devised a new idea to determine the mineral apposition rate, which measures how fast new bone forms. We found that this rate is linked to the energy lost by bone during mechanical loading.

To test this idea, we used a computer model of bone and simulated how fluid flow and pressure build up inside it when the load is applied. We used fluid flow and pressure data to calculate the energy lost and coupled it with the mathematical model derived to estimate the new bone formation. We found that just one of these two things alone is not enough to make new bone on both surfaces of the bone. However, when they considered both (i.e., energy lost due to fluid flow and pore pressure), we saw they work together to help bones stay strong.

Abstract

Bone loss is a serious health problem associated with old age and bone/muscle disuse. Classic examples such as elderlies, astronauts, patients having spinal cord injuries, etc., show the symptoms of bone loss and are vulnerable to fracture risk. Several factors are responsible for bone resorption, such as loss of mechanical environment, hormonal deficiency, genetics, and nutrition. In the last few decades, mechanical loading and pharmacological agents proved themselves as a solution as they reverse this degenerative process, encourage new bone formation, and reduce resorption. However, long-term use of these pharmacological agents is expensive and has side effects such as pain, nausea, etc. Therefore, mechanical loading holds promise as a less costly and nonpharmacological means to mitigate bone loss.

In vivo and in silico studies have shown that load-induced fluid flow in lacunae canalicular network (LCN) inhibits bone loss and promotes new bone formation, suggesting that load-induced interstitial fluid flow (IFF) in LCN may be a primary stimulus as it exerts shear and drags forces on osteocytes. Accordingly, most of the current mathematical models consider fluid flow as a stimulus for osteogenesis. However, these models fail to predict new bone formation simultaneously at both the periosteal and endocortical surfaces. To the best of our knowledge, no unifying principle relates new bone formation (simultaneously at both surfaces) with its mechanical environment. Besides IFF, it has also been shown that pore pressure generated under physiological loading conditions is adequate to enable osteocytes to respond. Despite the importance of IFF and Pore pressure, their exact roles have not yet been established. In order to fill the research gap, this thesis investigates the role of fluid flow and pore pressure on site-specific new bone formation induced by exogenous mechanical loading. A novel derivation of mineral apposition rate (MAR) in terms of dissipation energy density has been introduced, hypothesizing that the Mineral Apposition Rate (MAR) is proportional to the

square root of the dissipation energy density minus its reference value. Dissipation energy density is selected as a stimulus due to its capacity to incorporate both fluid flow and pore pressure.

Computational implementation of the mathematical model has been carried out through a poroelastic finite element analysis, where the bone is assumed to be porous and filled with fluid, with a boundary condition that the periosteum is impermeable to the fluid and the endosteal surface maintains a reference zero pressure. The fluid velocity and pore pressure estimated from the above analysis are used to calculate the dissipation energy density. This new mathematical model tested the role of fluid flow and pore pressure individually and in combination to predict cortical bone adaptation.

The results indicate that fluid flow or pore pressure alone as a stimulus cannot predict osteogenesis at both cortical surfaces. In contrast, in combination, fluid flow and pore pressure closely fit site-specific new bone formation on both surfaces. It affirms that more than one mechanical stimulus is required to predict load-induced osteogenesis. The model has also been tested for another in vivo loading protocol and has been found precise in predicting new bone distribution. As a bottom line, the resulting model is the first of its kind, as it has been able to correctly predict MAR at both endocortical and periosteal surfaces. This study thus significantly advances the modeling of cortical bone adaptation to exogenous mechanical loading.

Based on the findings, an overall bone formation model is also developed, directly measuring the average bone formation rate (BFR) on both cortical surfaces. This model further substantiates the role of fluid flow and pore pressure in bone adaptation.

Keywords: Site-specific mineral apposition rate (MAR), Bone Formation Rate (BFR), Dissipation energy density, Interstitial fluid flow, Pore pressure, and Endocortical and Periosteal surfaces.

List of Publications from Thesis

Journal

 S. Singh, S. J. Singh, and J. Prasad, "Derivation, Validation, and Prediction of Loading-Induced Mineral Apposition Rate at Endocortical and Periosteal Bone Surface Based on Fluid Velocity and Pore Pressure," *Bone Reports*, vol. 19, Dec. 2024, doi: https://doi.org/10.1016/j.bonr.2023.101729.

Conference Proceeding

- S. Singh, "Workshop on Understanding the Methodologies and Basics of Animal Research (UMBAR-2019)," Nov. 26-Dec. 2, CSIR-IMECH, Chandigarh, India.
- S. Singh, S. J. Singh, and J. Prasad, "Investigating the Difference in Cortical Bone Adaptation at Endocortical and Periosteal Surfaces by Fluid Flow Analysis," ASME International International Mechanical Engineering Congress & Exposition Proceeding (IMECHE-2022), vol. 5, doi: https://doi.org/10.1115/IMECE2021-71220.
- 3. S. Singh, S. J. Singh, and J. Prasad, "Bone Adaptation: Role of Interstitial Fluid Flow and Pore Pressure, " *X International Conference on Computational Bioengineering (ICCB 2023)*, Sep. 20-22, TU Wien (Vienna University of Technology), Austria.

Table of Contents

Declaration of Originalityiv
Acknowledgmentsv
Lay Summaryviii
Abstractix
List of Publications from Thesisxii
List of Figuresxvii
List of Tablesxx
Notations and Abbreviationsxxi
Chapter 1 – Introduction
1.1 Motivation1
1.2 Bone Anatomy and Physiology
1.3 Mechanobiology of Bone
1.4 Mathematically Relating Fluid Flow With Bone Adaptation14
1.5 Unresolved Issue
1.6 Organization of Thesis
Chapter 2 – Unraveling the Role of Dissipation Energy in Bone Mineralization: A Novel
Derivation of Mineral Apposition Rate
Abstract
2.1 Introduction
2.2 Basic Terminology Used in Bone Modeling
2.2.1 Mineralizing Surface (MS)20

2.2.2 Mineral Apposition Rate (MAR)	21
2.2.3 Bone Formation Rate (BFR)	22
2.3 Dissipation Energy Density at the Tissue Level	22
2.4 Derivation of Mineral Apposition Rate (MAR)	23
2.5 Summary and Discussion	26
Chapter 3 – Predicting Site-Specific Cortical Bone adaptation: Role of Fluid flow	28
Abstract	28
3.1 Introduction	28
3.2 Methods	31
3.2.1 Finite Element Model	31
3.2.2 Bone Geometry	31
3.2.3 Porosity and Permeability of Bone	31
3.2.4 Permeability of Bone Surface	33
3.2.5 Loading and Boundary Conditions	33
3.2.6 Other Details	34
3.2.7 Dissipation Energy Density	36
3.2.8 Osteogenesis as a Function of Fluid Flow	38
3.2.9 Statistical Analysis	39
3.3 Results	40
3.3.1 Osteogenesis as a Function of Fluid Velocity	41
3.4 Discussion	47

3.5 Conclusion	44
Chapter 4 – Predicting Site-Specific Cortical Bone Adaptation: The Role of	Pore Pressure
Alone and in Combination with Fluid Flow	45
Abstract	45
4.1 Introduction	46
4.2 Methods	50
4.2.1 Finite element model	50
4.2.2 Dissipation Energy Density	51
4.2.3 Osteogenesis as a Function of Pore Pressure	55
4.2.4 Osteogenesis as a Function of Fluid Flow and Pore Pressure	56
4.3 Results	56
4.3.1 Osteogenesis as a Function of Pore Pressure	57
4.3.2 Osteogenesis as a Function of Pore Pressure and Fluid Flow	59
4.4 Simplified Model	60
4.4.1 Prediction Example	61
4.4.2 Sensitivity Analysis	62
4.5 Discussion	64
4.6 Conclusion	68
Chapter 5 – Overall Bone Adaptation Model	69
5.1 Introduction	69
5.2 Materials and Methods	71
5.2.1 Finite Element Model	71

5.2.2 Dissipation Energy Density	71
5.2.3 Estimation of Bone Formation Rate	73
5.3 Results and Discussion	76
5.4 Conclusion	82
Chapter 6 – The Outcome of the Work	84
6.1 Introduction	84
6.2 Specific Contributions	85
6.3 Future Scope	86
Appendix A	88
References	92

List of Figures

Figure 1.1 Schematic diagram of the macroscopic to microscopic bone anatomy4
Figure 1.2 Schematic diagram of cellular components of bone
Figure 2.1 Schematic diagram of the trabecular bone structure showing (a) single and double
labels and (b) the mineralizing surface (yellow label)
Figure 2.2 Schematic diagram of the trabecular bone structure showing (a) single and double
labels and (b) the mineral apposition (yellow label)21
Figure 2.3 Kelvin Voigt's model is a mechanical analog of a viscoelastic material22
Figure 2.4 Bone adaptation algorithm flowchart. 27
Figure 3.1 Mechanical loading of bone leads to the transmission of load to the cellular level
via fluid flow in lacunae canalicular porosity
Figure 3.2 Pictorial representation of (a) 8-week-old C57BL/6 mouse tibia with (b) an
idealized cross section at section a-a' (adapted from Barmen et al. (95)), (c) A simplified
prismatic beam developed with a cross-section similar to the section at a-a'
Figure 3.3 Finite-element meshing of the prismatic beam having a cross-section similar to the
midsection of a mouse tibia
Figure 3.4 Cross-section of the mid diaphysis of 8-week-old C57Bl/6J mouse tibia showing
zone of influence (solid circular arc), line a-a', and radial lines (red, dashed lines) (adapted from
Fig 4(b) of Berman et al. (95))
Figure 3.5 (a) Longitudinal strain distribution adapted from Barmen et al. (95), and (b) velocity
distribution (mm/sec) on the bone cross-section
Figure 3.6 Dissipation energy density (DED) due to fluid velocity along the radial line a-a' on
the anterior side of the mid-cross section of the beam (see Fig. 3.4), progressing from the
endocortical surface (ES - Node 1) to the periosteal surface (PS - Node 8)41

Figure 3.7 (a) In vivo, new bone formation at the cortical surfacers for mid-strain loading
protocol (adapted from Berman et al. (95)), and the corresponding numerically predicted new
bone distribution as a function of (b) fluid flow
Figure 4.1 Schematic diagram of canaliculus, longitudinal osteocyte process passing through
the fluid-filled canaliculus and attachments fo the process, (a) before and (b) after deformation
(p and v represent pore pressure and fluid velocity, respectively)50
Figure 4.2 (a) Longitudinal strain distribution adapted from Barmen et al. (95), (b) velocity
distribution (mm/sec), and (c) pressure distribution (MPa) on the bone cross-section57
Figure 4.3 Dissipation energy density (DED) due to fluid velocity and pore pressure along the
radial line a-a' on the anterior side of the mid-cross section of the beam (see Fig. 3.4 of Chapter
3), progressing from the endocortical surface (ES - Node 1) to the periosteal surface (PS - Node
8)58
Figure 4.4 (a) In vivo, new bone formation at the cortical surfaces for mid-strain loading
protocol (adapted from Berman et al. (95)), and the corresponding numerically predicted new
bone distribution as a function of (b) pore pressure only, and (c) pore pressure with fluid flow.
59
Figure 4.5 (a) The distribution of new bone in vivo at cortical surfaces for mid-strain loading
protocol (adapted from Berman et al. (95)). (b) The corresponding computationally estimated
new bone distribution using a simplified model is also illustrated
Figure 4.6 (a) In vivo new bone distribution at cortical envelops for high strain loading
protocol (adapted from Berman et al. (95)) and (b) corresponding computationally estimated
new bone distribution using the simplified model
Figure 4.7 Plots showing BFR as a function of (a) remodeling rate A and (b)
threshold/reference parameter ψref , which in turn is also shown in (c) as a function of number
of loading cycles N 64

Figure 5.1 Pictorial representation of (a) C57BL/6 mouse tibia with (b) an idealized cross
section at section a-a' (adapted from Srinivasan et al. (99)). (c) A simplified beam developed
with a cross-section similar to the section at a-a'
Figure 5.2 The finite element meshed beam has a cross-section similar to the midsection of the
mouse tibia
Figure 5.3 Trapezoidal loading waveform (a) with rest and (b) without rest insertion75
Figure 5.4 Three-dimensional fluid flow patterns when the tibia is under a loading inducing
1000 μ ε at 1Hz frequency for the cantilever bending
Figure 5.5 Variation of velocity with time at a node on endocortical surface for the trapezoidal
cyclic loading (protocol 1) (a) and rest inserted trapezoidal cyclic loading (protocol 4) (b)78
Figure 5.6 Comparison between the BFR – mathematical model and the BFR(PS) – in vivo
for the periosteal surface. PS stands for the periosteal surface
Figure 5.7 Comparison between the BFR – mathematical model and the BFR (ES) – In vivo
at the endocortical surface. ES Stands for endocortical Surface
Figure 5.8 Illustration depicting (a) fluid velocity and (b) pore pressure at a node (54732) on
the endocortical surface and node (54927) on the periosteal surface for protocol 182
Figure A1 (a) Schematic diagram of the bar of height h supporting constant compressive stress
and (b) the equivalent Kelvin-Voigt model considering the bar to be viscoelastic (E and $\boldsymbol{\eta}$ are
the Young's modulus and viscosity of the material, respectively)

List of Tables

Table 3.1 Material Properties used for simulation (adapted from (Zang and Cowin (119)) and		
(Cowin (107))	35	
Table 5.1 Loading protocols adapted from Srinivasan et al. (99)	75	
Table 5.2 Loading protocols adapted from Srinivasan et al. (150)	76	

Notations and Abbreviations

LCN - Lacunae Canalicular Network

BFR - Bone Formation Rate

 MAR_i – Mineral apposition rate at the node of interest, $\frac{\mu m}{day}$

i – Node of interest

 DE_v – Dissipation energy density due to fluid flow per unit cycle, $\frac{N\mu m}{\mu m^3}$

 DE_p – Dissipation energy density due to pore pressure per unit cycle, $\frac{N\mu m}{\mu m^3}$

 DE_{ref} – Reference/threshold value of dissipation energy density per unit cycle, $\frac{N\mu m}{\mu m^3}$

 $\overline{(DE_v)}_i$ – Modified dissipation energy density per unit cycle due to fluid flow at a given node i after considering the zone of influence, $\frac{N\mu m}{\mu m^3}$

 $\overline{\left(DE_p\right)_i}$ – Modified dissipation energy density per unit cycle due to pore pressure at a given node i after considering the zone of influence, $\frac{N\mu m}{um^3}$

 n_p – Porosity*

 v_{fl} – Fluid velocity at nodes, $\frac{\mu m}{s}$

p – Pressure at the nodes, $\frac{N}{\mu m^2}$

 ${\varphi_v}_i$ – Total dissipation energy density due to fluid flow, ${{
m N}\mu{
m m}\over {
m \mu m}^3}$

 ${\phi_p}_i$ – Total dissipation energy density due to pore pressure, $\frac{{\rm N}\mu{\rm m}}{\mu{\rm m}^3}$

 ψ_{ref} – Reference/threshold MAR in the absence of exogenous mechanical loading, $\frac{\mu m}{day}$

N – Number of loading cycles

d – Number of loading days

*Bone as a poroelastic as well as a viscoelastic material has been explained in Appendix A (See Pages 88-91). In addition, their equivalence is also discussed.

Chapter 1 – Introduction

1.1 Motivation

Osteoporosis is a prevalent metabolic bone disorder that poses a significant health concern globally due to its association with severe bone loss, which ultimately leads to fracture risk. Osteoporosis is generally classified as primary and secondary osteoporosis. Primary osteoporosis is associated with aging, whereas secondary osteoporosis is in one way or another related to other health problems, such as bone disuse due to paralysis (1), microgravity (2), long-term bed rest (3)(4), and glucocorticoid induction (5)(6). These individuals show the symptoms of osteoporosis and are vulnerable to fracture risk due to compromised bone strength.

What unites all cases of secondary osteoporosis is that they all lose their mechanical environment in one way or another. During daily activity, three forces are subjected to lower limbs: weight-bearing due to gravity, ground reaction forces, and loading due to muscle contraction during locomotion. When one or more of these forces diminishes, it leads to secondary or disuse osteoporosis. For instance, in the case of an astronaut, ground reaction forces (GRFs) on the lower limb are reduced, and muscle contraction is not restricted. Similarly, in the case of long-term bed rest, GRFs are absent, and muscle contraction is reduced. In the case of Spinal Cord Injury (SCI) patients, both ground reaction forces and muscle contraction are missing.

Studies on astronauts and SCI patients have provided valuable insight into bone loss patterns. The MIR spacecraft cosmonaut shows a total bone loss of 0.3% from the skeleton (7). The data from DXA assessment of International Space Station (ISS) crew members show bone loss from the lumber spine (0.8-0.9%/month) and hip (1.2-1.5%/month) (8), the skeletal sites where most osteoporotic fractures occur in elderly. Similarly, in the case of SCI patients, bone loss starts

just after the injury, predominantly in load-bearing bones such as the proximal tibia and distal femur, which are trabecular-rich sites (9). In contrast, cortical-rich sites are relatively spared (10). Wilmet et al., in their one-year-long study on SCI Patients, observed a rapid decrease in BMC at a rate of ~4%/month in the areas rich in trabecular bone and ~2%/month in areas rich in compact bone (11). However, no bone loss is recorded at the lumber spine despite having trabecular bone (9). This might be due to the continuous spine loading while sitting in a wheelchair.

Meanwhile, it is essential to note that while the level of bone loss may not elevate the fracture risk immediately, it could predispose individuals to fractures later in life. Consequently, preventing bone loss has become a focus of current research efforts. Over the years, it has been observed that mechanical loading serves as a countermeasure for this bone loss (12)(13). For example, Haapasalo et al. (12) showcased significant side-to-side differences among tennis players, favoring the dominant (playing) arm. These differences are evident in bone parameters, including Bone Mineral Content (BMC) (14%–27%) and Total Cross-sectional Area (Tot.Ar) (16%–21%), Cortical Area (Co.Ar) (12%–32%), Bone Strength Index (BSI) (23%–37%), Principal moment of Inertia (I_{min} (33%–61%), and I_{max} (27%–67%)) at all measured bone sites. Therefore, understanding the underlying mechanism by which mechanical loading controls bone adaptation became necessary to build new strategies to minimize bone loss and lower fracture risk, which is the thrust of this thesis. However, before delving into the topic, it is crucial to understand the basics of bone anatomy and physiology and our current understanding of bone adaptation.

1.2 Bone Anatomy and Physiology

The bones in the skeleton serve various functions, such as providing structural and lever support for muscles to allow movement and locomotion of the body, acting as a protector of

internal organs, reservoir for calcium and phosphate ions, growth factors, and cytokines, and creating an environment for the hematopoiesis in the marrow cavity (14). Bone needs stiffness and toughness to fulfill these demands.

The bones can be categorized into two different tissue types, i.e., cortical (or compact) and cancellous (or trabecular) bones, as demonstrated in Fig. 1.1. The cortical bone is densely packed tissue consisting of an array of osteons or a Haversine system. Each osteon has a central canal housing blood vessels and nerves surrounded by the concentric lamellae of bone tissue. The outer layer of the osteon, the cement line, has around 5 μm of mineralized bone (15). The uniformly spaced cavities in the osteons are called lacunae and are connected via branching canaliculi to form a continuous network of interconnected cavities. The high mass per unit volume of cortical bone endows it with great compressive strength. The trabecular bone is a honeycomb structure of trabecular plates and rods interspersed in the bone marrow compartment (Fig. 1.1). These trabecular plates and rods are also composed of osteons known as bone packets, which are saucer-shaped and consist of layers of lamellae. The low matrix mass per unit volume of trabecular bone reduces its strength to one-tenth of cortical bone (16). The cortical-to-trabecular bone ratio varies with the skeletal site and decides the function of bone (17). For example, in the femoral diaphysis, the ratio is 95:5, reflecting the high strength and rigidity of the long bone required for weight bearing. Whereas, in the femoral head, the ratio of cortical to cancellous bone is 50:50, which shows that the femoral head plays a lesser yet significant mechanical role by providing internal support, i.e., helping distribute load and energy absorption.

The bone has an outer and inner covering known as periosteum and endosteum. The periosteum consists of two layers: the outer layer is fibrous, and the inner layer, which is in direct contact with the bone, is called the cellular or cambium layer. The fibrous layer consists of fibroblast, collagen, and elastin fibers, whereas the cambium layer consists of microvessels, Mesenchymal

stem cells, which can differentiate into osteoblasts and chondrocytes, etc. (18)(19). The endosteum is a thin sheath on the endocortical surface, and the trabeculae of the bone consist of bone lining cells and osteoblasts. This thin sheath membrane encloses the bone marrow (20).

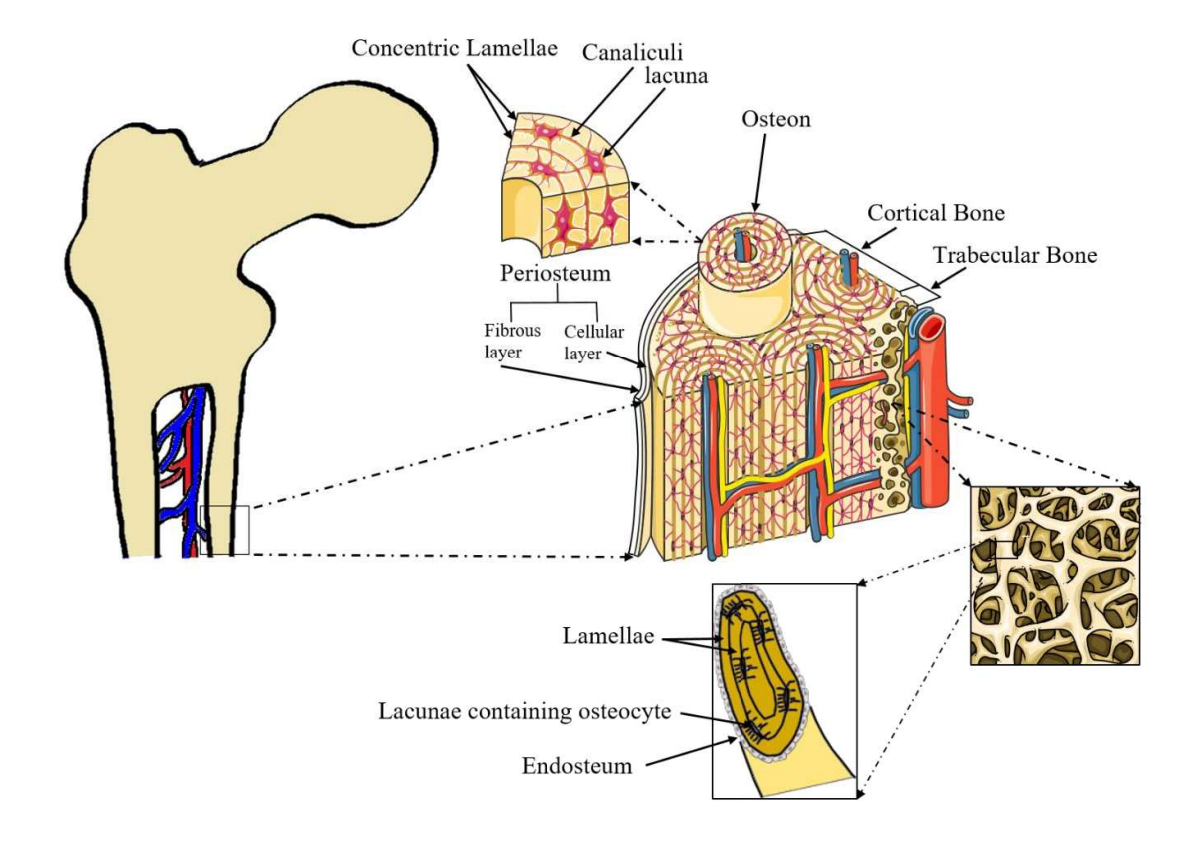


Figure 1.1 Schematic diagram of the macroscopic to microscopic bone anatomy.

The bone matrix in both cortical and cancellous bone tissues is a composite material consisting of organic and inorganic components. The organic portion constitutes about 20% of the bone's wet weight and is predominantly made up of type I collagen (90%) with smaller amounts of collagen type III, V, X, and XII (21). Collagen fibers, which have a rope-like structure, are formed by the spontaneous grouping of collagen fibrils. Each collagen fibril consists of two α 1 and one α 2 polypeptide chains, synthesized within osteoblasts to create a triple-helix procollagen molecule (22). These procollagen molecules are secreted by osteoblasts and subsequently converge together to create collagen fibrils.

The inorganic matrix makes up about 60%-70% of bone's wet weight and acts as a reservoir for calcium, phosphorus, sodium, and magnesium (21). These ions form calcium hydroxyapatite [Ca₁₀PO₄(OH)₂] crystal structure around and within the collagen fibers. Collagen provides bone with flexibility, while the mineral added to the collagen gives bone its stiffness. Thus, varying the amount and distribution of collagen and minerals allows bone to balance its flexibility and stiffness according the needs.

The cellular component of the bone has bone-resorbing cells (osteoclasts) and bone-forming cells (Osteoblasts, osteocytes, and bone lining cells), as shown schematically in Fig. 1.2. The osteoclasts are multinucleated cells derived from the mononuclear cells of HSCs origin under the influence of several factors, such as macrophage-colony stimulating factor (M-CSF), which is secreted from the osteoprogenitor cells and the osteoblast (23), and receptor activator of nuclear factor kappa beta ligand (RANK-L), secreted by osteoblast, osteocytes, and stromal cells (24). The preosteoclast precursors (mononuclear cells) fuse to form a multinucleated immature osteoclast in the presence of M-CSF, which binds to the cFMS receptor in preosteoclasts and induces proliferation (25), and RANK-L, which binds to the RANK receptor on the preosteoclasts (26). The continued existence of RANK-L is essential for the differentiation of immature osteoclasts to mature osteoclasts. This RANK-L/RANK interaction promoted the secretion of NFATc1 and DC-STAMP. The NFATc1 interactions with factors such as PU.1, cFos, and MITF result in tartrate-resistant acid phosphatase (TRAP) secretion, which is crucial for osteoclast activity (27). OPG (osteoprotegerin) is another factor secreted by osteoblasts, stromal cells, and periodontal fibroblasts, which competitively occupy the RANK-L binding site RANK on preosteoclasts and inhibit osteoclastogenesis (28). It means that cells of MSC origin control osteoclastogenesis. The process of bone resorption is initiated when the mature osteoclast is attached to the bone matrix by integrins and creates a sealed compartment between its ruffled border membrane and extracellular bone matrix. The

osteoclast's polarization achieves this whole sealing process, in which the cytoskeleton rearranges to form the F-actin ring and isolates the ruffled border (29). Vacuolar-type H⁺-ATPase in the ruffled edge of osteoclast acidifies the compartment to dissolve the hydroxyapatite crystal, consequently exposing the bone's organic matrix. The exposed organic matrix further degrades with the secretion of TRAP, cathepsin K, and matrix metalloproteinase-9 (MMP-9) from the osteoclast (30).

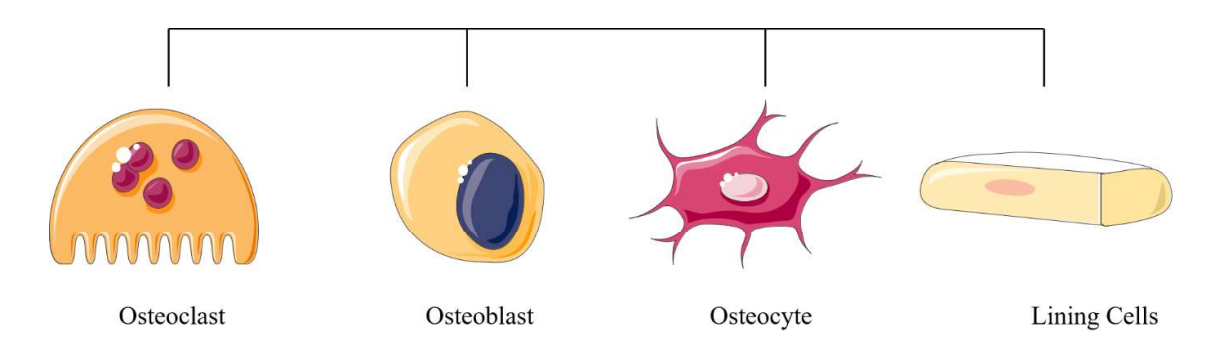


Figure 1.2 Schematic diagram of cellular components of bone.

Osteoblasts are derived from the MSCs in the bone marrow stroma and periosteum. MSCs can differentiate into different cells, such as osteoblasts, adipocytes, chondrocytes, and myocytes. To move precursor cells towards osteoblast lineage, secretion of genes, transcription factors runt-related transcription factor-2 (Runx2), distal-less homeobox-5 (D1x5), and msh homeobox homologue-2 (Msx2) are essential (31)(32). The differentiation of immature osteoblasts to mature osteoblasts requires the expression of Runx2, osterix (Osx), and several components of the Wnt signaling pathway (31)(33)(34). Osteoblast starts bone formation with the secretion of collagenous (collagen type I) and noncollagenous proteins (osteocalcin (OCN), bone sialoprotein (BSP) I/II, and proteoglycan). The mineralization of osteoid starts with releasing the matrix vesicles from the osteoblast, containing calcium ions and phosphate compounds. These matrix vesicles are attached to the bone matrix's organic component, proteoglycan. The enzymes secreted by osteoblast degrade the proteoglycan, which results in

the nucleation of calcium and phosphate ions in the matrix vesicles. These nucleated hydroxyapatite crystals are then released into the body fluid supersaturated with Ca²⁺ and PO⁴⁻ ions, which further helps in the continuous proliferation of new crystals (35)(36).

During the secretion of osteoid (unmineralized matrix), some osteoblasts get embedded and start changing their morphology and structure, such as decreasing their size, the rough endoplasmic reticulum, and the Golgi apparatus. It increases the ratio of the nucleus to the cytoplasm, corresponding to a decrease in protein synthesis (37). These cells gradually develop the cytoplasmic processes and express the E11, the early osteocyte marker. At this stage, these cells are called immature osteocytes. With the mineralization of the bone matrix, these immature osteocytes begin to mature and express several genes, including dentin matrix protein-1 (DMP-1), matrix extracellular phosphoglycoprotein (MEPE), and sclerostin (SOST) (38)(39)(40). Osteocytes are the most abundant cells in the bone, comprising 90% - 95% of total bone cells. For decades, osteocytes were believed to be passive cells (41). However, developing new technologies, such as bone cell isolation and culture, animal models, etc., leads to a better understanding of osteocytes. Osteocytes reside in lacunae, whereas their processes cross canaliculi. The processes of these osteocytes connect via gap junction to each other and osteoblast and bone lining cells on the bone surface, creating a system that facilitates the transmission of the biochemical signal. This lacuna canalicular system is filled with interstitial fluid, which also helps transmit biochemical signals, mechanosensation, and waste products. In addition, these cells get the nutrients and oxygen supply from the blood vessels passing nearby (42).

1.3 Mechanobiology of Bone

In bone, the external load is not borne by the cells, but by the extracellular matrix, it produces.

Bones can sustain this load without failure because the cells can regulate the mass and architecture according to functional requirements. Hence, bone can be termed as a

mechanically sensitive tissue that adapts its mass and architecture to its mechanical environment (43).

It was in the mid-1800s when von Meyer and Culmann postulated for the first time that the trabeculae were aligned with stress trajectories (44). At the 1866 Society of Natural Science conference in Zurich, Von Meyer demonstrated the arched architecture of sagittally sectioned human first metatarsal and calcaneus, with Culmann observing how the pattern of trabecular architecture resembled the stress trajectory produced by the functional loading. Culman drew an analogy between the trabecular pattern and stress trajectory in the short cantilever beam. Von Meyer and Culmann also compared the trabecular architecture of the coronal section of a human proximal femur with the mathematically constructed stress trajectory in a solid curved beam resembling the femur subjected to single-legged stance loading.

However, Julius Wolff set a law famously known as Wolff's Law, which states:

"Every change in the form and function of bone or their function alone is followed by certain definite changes in their internal architecture, and equally definite alteration in their external conformation, following mathematical laws."

It was Thomson who, for the first time, proposed that mechanical deformation, i.e., strain, is a direct cause of bone adaptation and stated that (45):

"the very important physiological truth [is] that a condition of strain, the result of a stress, is a direct stimulus to growth itself."

In 1964, Harold Frost introduces the mechanostate theory which states that strain in the bone must surpass the threshold of 1500-2500 µE range (setpoint of minimum effective strain) to initiate bone modeling (46). Moreover, Harold Frost also highlighted the difference between bone modeling and remodeling. Bone remodeling, a process involving coordinated action of osteoclast and osteoblast, is initiated by micro cracks that lead to osteocytes apoptosis. Whereas

bone modeling, where osteoclast and osteoblast function independently, adapts structure by changing bone size and shape. This thesis focuses specifically on the bone modeling process, particularly on new bone formation by osteoblasts at the cortical surfaces. Therefore, throughout the thesis, the term bone adaptation will refer to bone modeling only.

The most important finding is that the dynamic strain, not static strain, is responsible for bone adaptations (47)(48). In addition, Rubin and Lanyon, through their isolated avian ulna model, also showcased that bone modeling is also a linear function of strain magnitude (49). The dynamic nature of loading required for bone adaptation implies that the bone responds to various loading parameters beyond strain magnitude, such as frequency of loading waveform and strain rate (50)(51). For instance, Rubin and Mcleod demonstrated that a low magnitude load used at 1 Hz could not maintain the bone mass; however, if applied at a higher frequency, such as 20 Hz, it can significantly induce osteogenesis at both cortical surfaces (50). Turner et al. also illustrated using the rat tibia model that the loading frequency must be 0.5 Hz or higher to induce the osteogenic response (52). However, this relationship between frequency and osteogenesis does not hold beyond 10 Hz (53). In addition, Turner et al. (51), based on the rat tibia four-point loading model, show that osteogenesis increases as the strain rate increases. To incorporate these facts (bone adaptation being a function of strain rate, strain magnitude, and loading frequency) into a mathematical framework, Turner et al. (54) demonstrated that strain rate is directly proportional to the product of frequency and peak strain magnitude for a simplified cylindrical beam. Extending this theory to the rat ulna model and accordingly hypothesize that the stimulus required for bone osteogenesis can be expressed by:

$$S = k_1 \sum_{i=0}^{\infty} \varepsilon_i f_i \tag{1.1}$$

where ε , f, k_1 , and S are the strain amplitude, loading frequency, proportionality constant, and strain stimulus, respectively. One thing to remember is that the above equation is valid till the

frequency of 2 Hz because, at higher frequencies, bone cells become less sensitive to loading (55). However, for most practical purposes, loading frequencies remain within 2 Hz.

Further loading parameters influencing bone adaptation are loading duration and rest interval between loading bouts. The skeletal adaptation does not increase linearly with the number of loading cycles (56)(57). As the loading duration increases, bone formation tends to saturate. Rubin and Lanyon best illustrated this phenomenon through their isolated avian ulna model, showing that bone formation does not significantly increase beyond 36 loading cycles (56). Similarly, Umemura et al., in their study in which rats were grouped into jump groups according to the number of jumps per day, demonstrated that five jumps per day are sufficient to induce a significant increase in cortical area. In contrast, a hundred jumps per day did not significantly increase the cortical area compared to the ten jumps per day. If the bone response saturates quickly with the number of loading cycles, asking how long the bone will take to resensitize is reasonable. Robling et al. conducted an experiment in which a rat tibial four-point loading model was used to investigate bone saturation and resensitization (58). They categorized participants into four groups based on the different loading protocols and a separate control group, which did not receive any loading. The first group received six bouts, each comprising sixty cycles (60x6), with a two-hour break between sessions. The second group underwent four bouts, each of ninety cycles (90x4), with a rest of three hours between each bout. The third group experienced two bouts, each involving one hundred and eighty cycles (180x2), with a six-hour break between sessions. Lastly, the fourth group gets one bout of 360 daily cycles (360x1). The loading protocol lasted for five days at a 54 N peak load of 2 Hz. All the loading groups showed significant bone formation compared to the control group. However, the groups (60x6) and (90x4) were found to be more osteogenic than the (360x1)group. The results showed that the rest of 2-3 hours between loading bouts is necessary to resensitize the bone again. However, a question remains: how much gap is ideal between each

loading bout? To understand this, Robling et al. did another experiment that varied the recovery time between the four loading bout of ninty cycles/bout (59). They used 0, 0.5, 1, 2, 4, and 8 hours as the recovery period between loading bouts. The results showed more than 100% bone formation rate in 8-hour recovery groups compared to the 0-hour and 0.5-hour groups. Accordingly, 8 hours of recovery is sufficient to resensitize the bone after a loading bout.

It is also shown that apart from recovery time after every loading bout, the rest between individual loading cycles can enhance the bone's osteogenic response (60). They used the avian ulna model and applied 100 cycles/day at 2 Hz with a rest interval of 10 seconds between loading cycles. They observed that at the periosteal surface, the bone formation rate is higher in the case of rest insertion compared to the bone formation data from the loading conditions where no rest is inserted between loading cycles.

The tissue-level strains typically remain below 0.2% (2000 microstrains), and the in vitro experiment with bone cells indicates that cellular-level strains more significant than 0.5% (5000 microstrains) are necessary to elicit intracellular signaling (61). Additionally, Nicolella et al. (62), using a digital image correlation strain measurement technique, demonstrated that microscopic strains near irregularities, such as lacunae and canaliculi (mean strain measured approximately 7900 μ E, maximum strain measures is 39000 μ E), were significantly higher than the global strain (approximately 2000 μ E). The authors themselves noted that the areas with such high strains resembled micro-damage around osteocyte lacuna, suggesting that such elevated strains may act as precursors to micro cracks and potentially trigger the remodeling process. However, this thesis focuses on the bone modeling process, specifically on new bone formation at the cortical surfaces. Hence, strain cannot be considered as a stimulus for new bone formation during the bone modeling process.

Insights from the in-vitro studies and all the factors related to dynamic strain mentioned above are forcing us to believe that load-induced fluid flow likely drives bone adaptation (bone modeling). In the mid-nineties, a theory emerged known as the fluid shear stress (FSS) hypothesis, which demonstrated that despite having small tissue strain, Fluid Shear Stress (FSS -8 to 30 dyne/cm² under physiological loading) generated on the osteocyte cell process due to load-induced fluid flow in the lacune canalicular network (LCN) is sufficient to initiate cellular signaling that can trigger bone adaptation (63). More recent work suggested that substantial drag forces are generated on the tethering fibers, which connect the cell process to the mineralized bone, which may contribute more than the FSS (64)(65)(66). For instance, You et al. (64) developed a strain amplification hypothesis. They intuitively said that tethering fibers are attached to the osteocyte process at one end and to the mineralized tissue at the other. When the mechanical load is applied to the bone, it generates the pressure gradient in the LCN, which, in turn, the load induces fluid flow. This fluid flow in the pericellular matrix creates hydrodynamic forces, which put the tethering elements in tension, hence radial strain in the osteocyte process. This model predicted an amplification of 10 to 100 times in the cellular level strains depending on the load applied to the bone tissue.

Han et al. (65) introduced a more realistic model based on the ultrastructural measurements conducted by You et al. in 2004 (67). However, neither the models by You et al. (64) nor Han et al. (65) incorporate the molecules that are the likely initiator of intracellular signaling. This gap is addressed by Wang et al. (66), where apart from tethering fibers, they incorporated the integrin-based focal adhesion complex. The model comprises a rigid conical projection connected to the osteocyte process via $\alpha_{\nu}\beta_{3}$ integrin. In addition, tethering fibers are also connected to the central actin filament allowing axial sliding relative to each other. The model predicted a substantial axial strain of approximately 6% in the osteocyte process in response to a loading of 1000 μ E at 10 HZ and 100 cycles which is 10 times more than Han et al. (65). This

strain developed is sufficient to open stretch-activated ion channels and initiate electrical signaling.

The question of how these mechanical signals (FSS, hoop stress, and axial strain in osteocyte processes) are transmitted to the cytoskeleton at the cellular level persists. However, recent findings have given us some clues about it. For example, Weinbaum et al. (63) demonstrated that the cell process is more likely to be stimulated because the pericellular space is much tighter in canaliculi than in lacunae, which leads to two orders of higher shear stress on the osteocyte process with respect to the osteocyte's cell body. In addition, an in vitro study by Burra et al. (68) also suggested that dendritic processes are the mechanotransducers that open the hemichannels. Moreover, tethering elements are also present in canaliculi, the primary source of stain amplification, as suggested by You et al. (64). The membrane-spaning glycoprotein, called integrin, is attached extracellularly to the collagen of the organic matrix (69). In contrast, intracellularly, it is attached to the cytoskeleton, which connects to the nuclear membrane (70). This complex is known as the extracellular matrix- integrin-cytoskeleton axis. The cytoskeleton, which is always in tension, also creates tension in the extracellular matrixintegrin-cytoskeleton axis. Hence, any deformation on the cell membrane due to extracellular fluid flow leads to extra tension in the cytoskeleton and transmits the fluid shear stresses to the nucleus to alter protein synthesis (71). Another possibility of biomechanical coupling could be facilitated by the mechanosensitive cation-selective channel (MSCC) (72). Following the loadinduced fluid flow, there is a rapid increase in the concentration of Ca²⁺ ions, which further depends on the extracellular Ca²⁺ entry and intracellular Ca²⁺ release from the endoplasmic reticulum. The influx of extracellular Ca²⁺ occurs through the MSCCs, which are activated by the deformation in the cell membrane due to fluid flow. When the gadolinium blocker blocks these channels, the concentration of Ca²⁺ ions reduces by approximately 30 %, which verifies the role of these ion channels (72).

When the mechanical stimulus is translated into biochemical signals, it must be conveyed to the cells (osteoblasts and osteoclasts) responsible for bone adaptation. In response to the increased Ca²⁺, vesicles containing ATPs are released, which bind to purinergic (P2) receptors. The activation of P2 receptors leads to the release of intracellular Ca²⁺ through a phospholipase C (PLC)-phosphatidylinositol bisphosphate (PIP2)-inositol triphosphate (IP3) pathway. The downstream mechanism following the P2 activation and subsequent rise in intracellular Ca²⁺ concentration is not fully understood. However, P2 signaling upregulates the Cox-2 expression, releasing prostaglandin (73)(74). Prostaglandin have effect on both the bone formation and bone resorption by regulating the proloferation and differentiation of osteoblast and osteoclast.

1.4 Mathematically Relating Fluid Flow With Bone Adaptation

Although it is believed that the fluid flow stimulates the osteocytes in bone during mechanical loading, minimal effort has been made to correlate this fluid flow with bone adaptation. The primary physical effects of fluid flow are pressure gradient, fluid velocity, and viscous dissipation. Researchers have explored these effects as a stimulus to understand bone adaptation better.

For instance, Kumar et al. utilized viscous dissipation energy density as a stimulus to capture the impact of fluid flow on new bone formation (75). They employed a general growth law model to mathematically relate the new bone formation with dissipation energy density. Their model accurately predicts osteogenesis at the periosteal surface of mice tibia, though it was not tested to predict osteogenesis at the endocortical surface. Similarly, Pereira et al., using an axial tibial loading model, developed a mathematical framework that correctly predicted the changes in cortical thickness as a function of fluid velocity but did not address osteogenesis at both cortical surfaces individually (76). Then, Carriero et al. investigated the new bone formation at both surfaces relative to fluid velocity. The model successfully predicted the new bone formation at the endocortical surface but not on the periosteal surface (77). Prasad and Goyal

also developed an analytical model that uses strain to predict new bone formation on periosteal and endocortical surfaces (78). In this model, they assumed bone to be viscoelastic to capture the interstitial fluid flow effect. Their approach successfully predicted the outcome of time-dependent parameters such as frequency and rest insertion on periosteal osteogenesis. This capability was not achieved by previously developed elasticity-based models, which did not estimate. However, their model falls short in anticipating endocortical osteogenesis despite considering viscoelasticity. Supporting the fluid flow hypothesis, van Tol et al. (79) demonstrated that fluid flow is a more accurate predictor of bone adaptation than strain. Their research also highlighted the influence of lacunae canalicular architecture and vascular porosity on fluid flow. Yet, even in their model, new bone distribution did not change monotonically with fluid velocity.

1.5 Unresolved Issue

Although much has been resolved regarding the load-induced fluid flow and its role in bone adaptation, it remains unclear why fluid flow as a stimulus cannot predict new bone formation simultaneously at both the periosteal and endosteal surfaces. Hence, the primary objective of this thesis is to develop a mathematical framework that relates bone adaptation with mechanical loading.

In particular, the following questions are addressed:

- "Is fluid flow as a stimulus sufficient to capture the effect of load-induced fluid flow on both the periosteal or endocortical surfaces?"
- or should we look for another stimulus to predict bone adaptation?"
- "If that is the case, what physical stimuli should be considered to establish an in silico model to predict site-specific new bone formation on both cortical surfaces?"

1.6 Organization of Thesis

The entire thesis has been documented in six chapters.

Chapter 1 introduces the motivation behind the research work, followed by the literature review on bone adaptation, including *in vivo*, *in vitro*, and *in silico* models.

Chapter 2 discusses the development of a novel mathematical framework that relates Mineral Apposition Rate (MAR) with dissipation energy density. The model hypothesis is that the mineral apposition rate is directly proportional to the square root of dissipation energy density minus the reference/threshold.

Chapter 3 discusses the role of fluid flow in predicting Mineral Apposition Rate (MAR) at both cortical surfaces. A poroelastic finite element model of bone based on an *in vivo* study adapted from literature is used to estimate the fluid velocity, which in turn is used to calculate dissipation energy density due to viscous fluid flow. The calculated dissipation energy density due to fluid flow serves as a stimulus in the mathematical framework developed in Chapter 2. This chapter shows that fluid flow alone can anticipate the site-specific new bone formation at the endocortical surface. However, it underestimates the site-specific bone formation rate at the periosteal surface. The developed model also shows that dissipation energy density is a more significant stimulus that can incorporate all the factors that affect bone adaptation, such as strain magnitude, number of loading cycles, rest insertion, etc.

Chapter 4 discusses the role of pore pressure alone and in combination with fluid flow to predict site-specific bone adaptation at both cortical surfaces. The poroelastic finite element model of bone used here is the same as in Chapter 3. However, this time, it is used to estimate both the pore pressure and fluid velocity, which in turn is used to calculate the corresponding dissipation energy density. The model is tested for two cases: (i) pore pressure alone and (ii) pore pressure in conjugation with fluid flow. For case (i), the mathematical model predicts the opposite of

what fluid flow alone has indicated in Chapter 3, i.e., pore pressure predicts the site-specific bone adaptation at the periosteal surface; however, it underestimates it at the endocortical surface. For case (ii), the model can accurately predict the site-specific new bone distribution at both cortical surfaces, showing that apart from fluid velocity, pore pressure is also required to indicate the site-specific new bone formation at both cortical surfaces.

Chapter 5 discusses the development of a new mathematical model designed to directly predict the Bone Formation Rate (BFR). Chapters 3 and 4 demonstrated that fluid flow, in conjugation with pore pressure, is essential for estimating site-specific osteogenesis. Based on these insights, a new mathematical model is developed to estimate BFR by considering dissipation energy density due to fluid velocity and pore pressure as stimuli.

Chapter 6 discusses this work's summary, conclusions, and future scope.

Chapter 2 – Unraveling the Role of Dissipation Energy in Bone

Mineralization: A Novel Derivation of Mineral Apposition Rate

Declaration: Some of the contents of this chapter are published in Bone Reports under the title 'Derivation, validation, and prediction of loading-induced mineral apposition rates at endocortical and periosteal bone surfaces based on fluid velocity and pore pressure.' https://doi.org/10.1016/j.bonr.2023.101729

Abstract

The chapter establishes the quantitative model to predict new bone formation at both cortical surfaces in response to mechanical stimuli, which is crucial for understanding bone adaptation. We introduce an innovative derivation of mineral apposition rate as a function of dissipation energy density due to mechanical loading. We choose dissipation energy density as a stimulus as it represents the comprehensive temporal and spatial factors influencing bone adaptation. Bridging the gap between mechanical loading and bone (re)modeling will lead to the development of new interventions to maintain skeletal integrity.

2.1 Introduction

The bone (re)modeling process is highly complex as it involves the sensing and transmission of mechanical signals by osteocytes, which helps recruit bone-forming cells (Osteoblast) to produce newly mineralized tissue (80)(81). The mathematical models try to reproduce the main characteristics of this process while keeping the model simplified. As briefly described in Chapter 1, Section 1.4 of this dissertation, limited attention has been given to establishing a quantitative model that can accurately predict new bone formation in response to mechanical stimuli. Some of these are those of Tiwari and Prasad (82), Prasad and Goyal (78), Pereria et al. (76) etc. Tiwari and Prasad (82) use the growth law to model bone adaptation and highlight that shear or fluid shear strain might be responsible for the new bone formation near the neutral

axis, as suggested in several in vivo studies. Prasad and Goyal (78) developed a new strain-based mathematical model that used the viscoelasticity theory to capture interstitial fluid flow's effect on new bone formation on the periosteal surface. They successfully predicted the outcome of time-dependent parameters such as frequency and rest insertion on periosteal osteogenesis, which previously developed elasticity-based models did not estimate. Hence, the mathematical model can provide valuable insight into the interplay between mechanical forces, cellular activity, and bone architecture.

This Chapter introduces an innovative derivation of Mineral Apposition Rate (MAR) in terms of dissipation energy density while considering bone as a viscoelastic material. The derivation suggests that MAR is proportional to the square root of dissipation energy density minus a reference value, forming the central hypothesis and elucidating energy dissipation's role in regulating bone mineralization. We choose dissipation energy density as a stimulus in this derivation because it is a scalar quantity and convenient. Unlike other stimuli, dissipation energy density encompasses all the spatial and temporal factors influencing bone adaptation, including strain magnitude, loading waveform, frequency, rest insertion, etc. (83)(84). In addition, several in vitro studies show that strain (85), canalicular fluid flow (86)(87), and pore pressure (88)(89) are the mechanical stimuli that elicit responses from the osteocytes, and dissipation energy density has a potential to incorporate all of them. By selecting dissipation energy density as a stimulus, the derivation aims to capture the comprehensive impact of mechanical forces on bone (re)modeling, providing a holistic framework for understanding bone adaptation mechanics.

Through this derivation, we try to contribute to a deeper understanding of biological mechanisms governing bone (re)modeling with the potential to develop novel treatments for bone loss and related disorders. Bridging the gap between mechanical stimuli and bone

(re)modeling outcomes may pave the way for targeted interventions to preserve skeletal integrity and function.

2.2 Basic Terminology Used in Bone Modeling

Before going into the derivation details, we will first understand the basic terminology of histomorphometry relevant to bone (re)modeling, such as Mineralizing Surface, Bone formation Rate, and Mineral Apposition Rate, which are described below:

2.2.1 Mineralizing Surface (MS)

It represents the extent of the bone surface that is mineralizing at a given point in time. It is given by the total extent of the labeled surface from label administration at that time (Fig. 2.1).

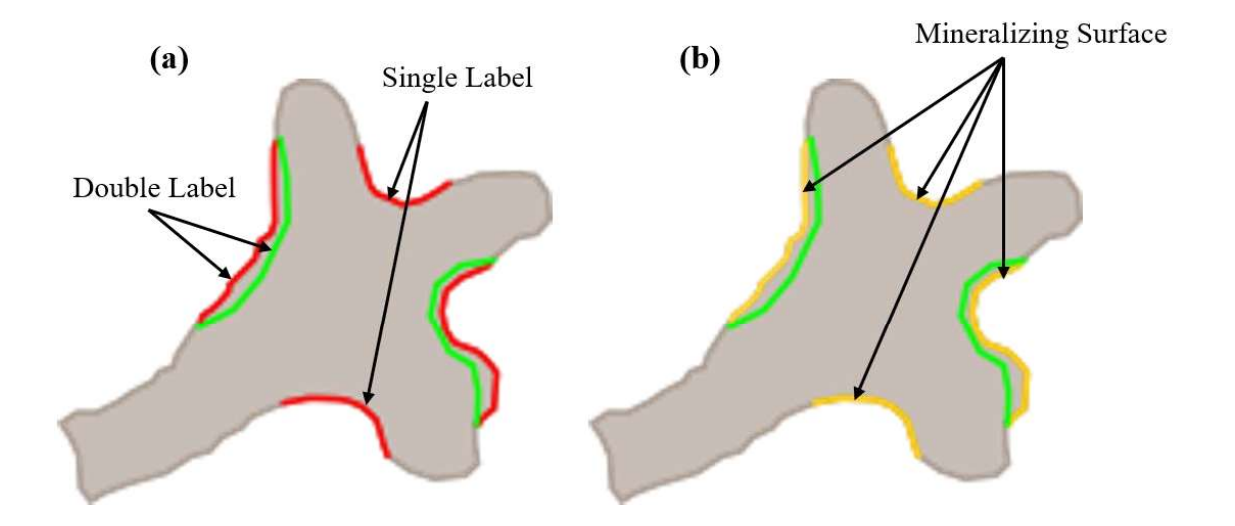


Figure 2.1 Schematic diagram of the trabecular bone structure showing (a) single and double labels and (b) the mineralizing surface (yellow label).

The mineralizing surface is generally expressed as mineralizing surface (MS) per unit bone surface (BS) can be estimated by the formulation as given below (90):

$$\frac{MS}{BS} = 0.5 * \frac{sLS}{BS} + \frac{dLS}{BS} \tag{2.1}$$

where $\frac{MS}{BS}$, $\frac{SLS}{BS}$, $\frac{dLS}{BS}$ are mineralizing surface, single-labeled surface, and double-labeled surface, respectively.

The MS/BS is measured in μ m/ μ m units and typically expressed as a percentage.

2.2.2 Mineral Apposition Rate (MAR)

The term Mineral Apposition Rate measures the site-specific new bone formation. It is estimated as the distance between the corresponding edges of two consecutive labels divided by the time between the labeling periods as given below (90):

$$MAR = \frac{Ir.L.Th}{Ir.L.T} \tag{3.2}$$

where *MAR*, *Ir. L. Th*, and *Ir. L. T* are the Mineral apposition rate, Interlabel thickness, and Interlabel time, respectively.

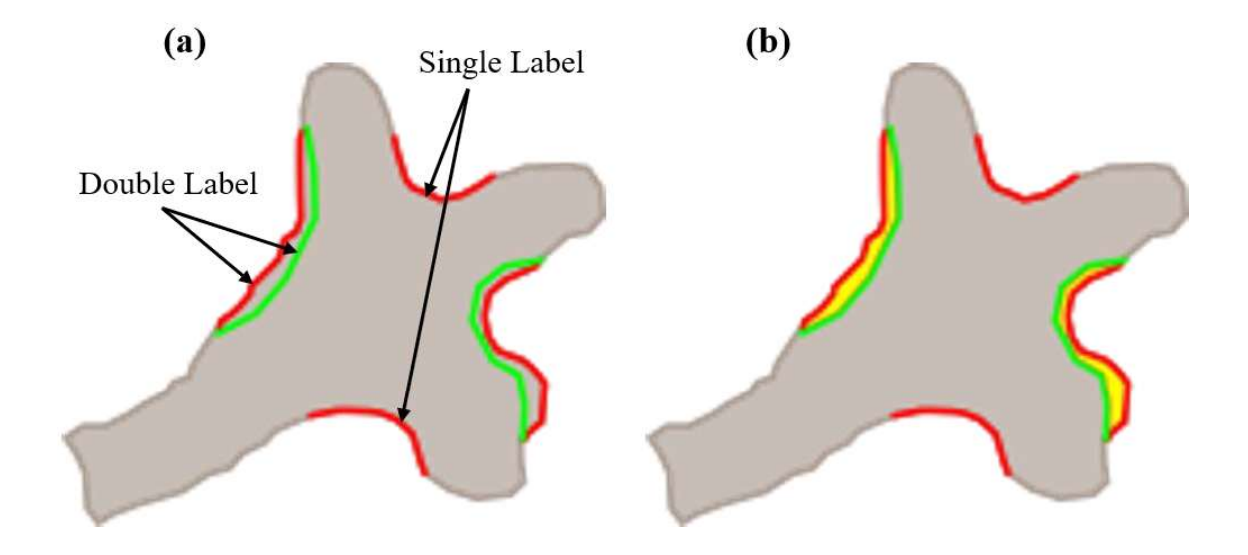


Figure 2.2 Schematic diagram of the trabecular bone structure showing (a) single and double labels and (b) the mineral apposition (yellow label).

2.2.3 Bone Formation Rate (BFR)

Bone Formation Rate represents the volume of mineralized bone formation per unit time. It is calculated as a product of the Mineral Apposition Rate and Mineralizing Surface/Bone Surface as given below (90):

$$BFR = MAR * \frac{MS}{BS}$$
 (2.3)

2.3 Dissipation Energy Density at the Tissue Level

The theory of viscoelasticity can be used to interpret bone's mechanical behavior (91). It considers bone tissue a single phase and uses Kelvin-Voigt's models as its mechanical analog, where an elastic spring and a viscous dashpot are attached in parallel, as schematically shown in Fig. 2.3. The governing equation for the deformation behavior of this model is as follows (92):

$$\sigma(t) = E\varepsilon(t) + \eta \dot{\varepsilon}(t) \tag{2.4}$$

where E and η are Young's modulus and the viscosity of the material.

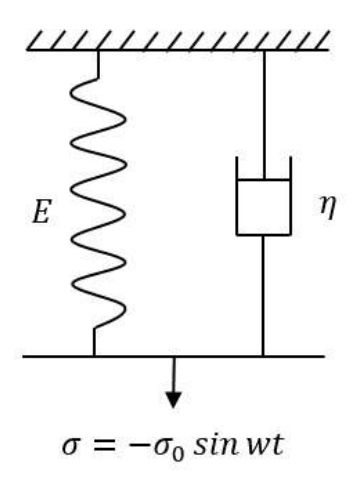


Figure 2.3 Kelvin Voigt's model is a mechanical analog of a viscoelastic material (91).

Considerable damping properties are found in bone, suggesting that bone will lose a fraction of the strain energy imposed on it under mechanical loading called dissipation energy. In the

context of bone, this dissipation energy can contribute to forming new bone or mineral apposition (75). The dissipation energy density per loading cycle of a cyclic load ($\sigma = \sigma_0 \sin \omega t$) at tissue level is given by (93),

$$DE_0 = \int_0^T \sigma \dot{\varepsilon} dt \tag{2.5}$$

From Eq. (2.4), the strain comes out to be

$$\varepsilon = \frac{\frac{\sigma_0}{\eta}}{\sqrt{\left(\frac{E}{\eta}\right)^2 + \omega^2}} \sin(\omega t - \emptyset)$$
(2.6)

By substituting Eq. (2.6) with Eq. (2.5), we get

$$DE_0 = \pi G_0^{"} \left(\frac{\sigma_0}{|G_0^*|} \right)^2 \tag{2.7}$$

where $G_0'' = \eta \omega$ and $G_0^* = E + iG_0''$ are loss and complex moduli of bone, respectively.

2.4 Derivation of Mineral Apposition Rate (MAR)

We need to relate the dissipation energy density to the Mineral Apposition Rate (MAR). We simplified the bone to be a homogeneous viscoelastic material to derive the approximate relation between MAR and dissipation energy density. The loading on the bone is also simplified to be purely axial.

When an exogenous harmonic force is applied to the bone, the overall response of the bone for increasing the bone cross-sectional area (A_c) (for example, per day) may be assumed to be similar to that of a first-order control system, i.e.

$$A_c = A_i e^{-\beta t} + A_f (1 - e^{-\beta t})$$
 (2.8)

or

$$\frac{dA_c}{dt} = \beta (A_f - A_c) \tag{2.9}$$

where A_c , A_i , and A_f are the bone's current, initial, and final cross-sectional areas, respectively. β is an unknown function of loading parameters such as the number of load cycles N, etc. (to be determined), and t is the time. This is based on the fact that bone area increases initially (upon application of exogenous loading) and saturates after sustained loading (46)(94).

It is desired to express dA_c/dt (i.e., the rate of change in bone cross-sectional area with respect to time) in terms of dissipation energy density. The tissue-level dissipation energy density per cycle of a sinusoidal loading of amplitude F_0 , is as follows:

$$DE_0 = \pi G_0'' \left(\frac{F_0}{A_c |G_0^*|} \right)^2 \tag{2.10}$$

where $G_0^*(\omega) = G_0'(\omega) + iG_0''(\omega)$ is the complex modulus (as a function of forcing frequency) for the bone tissue corresponding to in-vivo conditions. $G_0'(\omega)$ and $G_0''(\omega)$ respectively, are the corresponding storage and loss moduli.

If there are N cycles of the load being applied per day for d number of days per week, the total dissipation energy density may be given by

$$\varphi = DE_0.N.d = \pi G_0'' \left(\frac{F_0}{A_c |G_0^*|} \right)^2 Nd$$
 (2.11)

or

$$A_c \sqrt{\varphi} = \sqrt{\pi G_0'' N d} \cdot F_0 / |G_0^*|$$
 (2.12)

If the same loading protocol is maintained for the same bone, then for the bone cross-section in consideration:

$$A_c\sqrt{\varphi} = \gamma = A_i\sqrt{\varphi_i} = A_f\sqrt{\varphi_f}$$
 (2.13)

where γ is assumed to be a constant for a given loading protocol, neglecting any unmineralized bone area. The subscript i refers to the 'initial condition', i.e., the time immediately after the exogenous loading on bone starts. Subscript f refers to the 'final condition', i.e., the time by which the bone cross-section is completely adapted to the exogenous loading. Equation (2.13) indicates that as the cross-sectional area of bone increases under the given loading, energy dissipated by the bone will decrease. Furthermore, with the continued loading, the energy dissipation will progressively decrease until it reaches the threshold value (φ_f), beyond which there will be no further increase in the area. Equation (2.13) may be applied to Eq. (2.9) to obtain the following:

$$\frac{dA_c}{dt} = \gamma \beta \left(\frac{1}{\sqrt{\varphi_f}} - \frac{1}{\sqrt{\varphi}} \right) = \frac{\beta A_c}{\sqrt{\varphi_f}} \left(\sqrt{\varphi} - \sqrt{\varphi_f} \right)$$
 (2.14)

In experimental studies, the site-specific Mineral Apposition Rate (MAR) is approximately calculated for 'initial conditions' (i.e., within 2-3 weeks of initiation of exogenous loading). Hence, Eq. 2.14 may be rewritten as:

$$\left(\frac{dA_c}{dt}\right)_i = \frac{\beta A_i}{\sqrt{\varphi_f}} \left(\sqrt{\varphi_i} - \sqrt{\varphi_f}\right) \tag{2.15}$$

The whole bone may be divided into many sectors, the area of each of which may be used to calculate local MAR (i.e., new bone thickness per unit time) as follows:

$$MAR = \frac{1}{s_i} \left(\frac{dA_c}{dt} \right)_i = \frac{\beta \tau_i}{\sqrt{\varphi_f}} \left(\sqrt{\varphi_i} - \sqrt{\varphi_f} \right)$$
 (2.16)

where s_i is the circumferential length for the sector in consideration and A_i may now be considered as the sector area. The ratio of A_i and s_i is the cortical thickness (τ_i) for the sector. The simplified approximate version of Eq. (2.16) may be given by:

$$MAR = A(\sqrt{\varphi_i} - \sqrt{\varphi_f}) = A\sqrt{\varphi_i} - \psi_{ref}$$
 (2.17)

where A is a constant. φ_f may also be termed a universal threshold value. $\psi_{ref} = A\sqrt{\varphi_f}$ is again a function of N and d. The function β is given below:

$$\beta = \frac{A\sqrt{\varphi_f}}{\tau_i} \tag{2.18}$$

2.5 Summary and Discussion

This chapter presents a novel quantitative model that predicts new bone formation in response to mechanical stimuli by introducing a unique derivation of the Mineral Apposition Rate (MAR) in terms of dissipation energy density. By considering bone as a viscoelastic material, the model captures the intricate relation between mechanical loading, energy dissipation, and bone mineralization.

The efficacy of the mathematical framework developed in section 2.4 in predicting site-specific new bone formation at both the cortical surfaces (periosteal and endocortical surfaces) is yet to be confirmed. To validate this hypothesis, the next chapter involves constructing a finite element analysis model based on the mid-strain loading protocol employed in vivo study by Berman et al. (95), coupled with the mathematical model developed in section 2.4. Furthermore, the following chapters also explore whether fluid flow alone is adequate to stimulate new bone formation at both cortical surfaces or if an additional stimulus, alone or in combination with fluid flow, is necessary to predict mineral apposition rate at both cortical surfaces. Figure 2.4 illustrates the bone adaptation algorithm that will be used in the upcoming chapters.

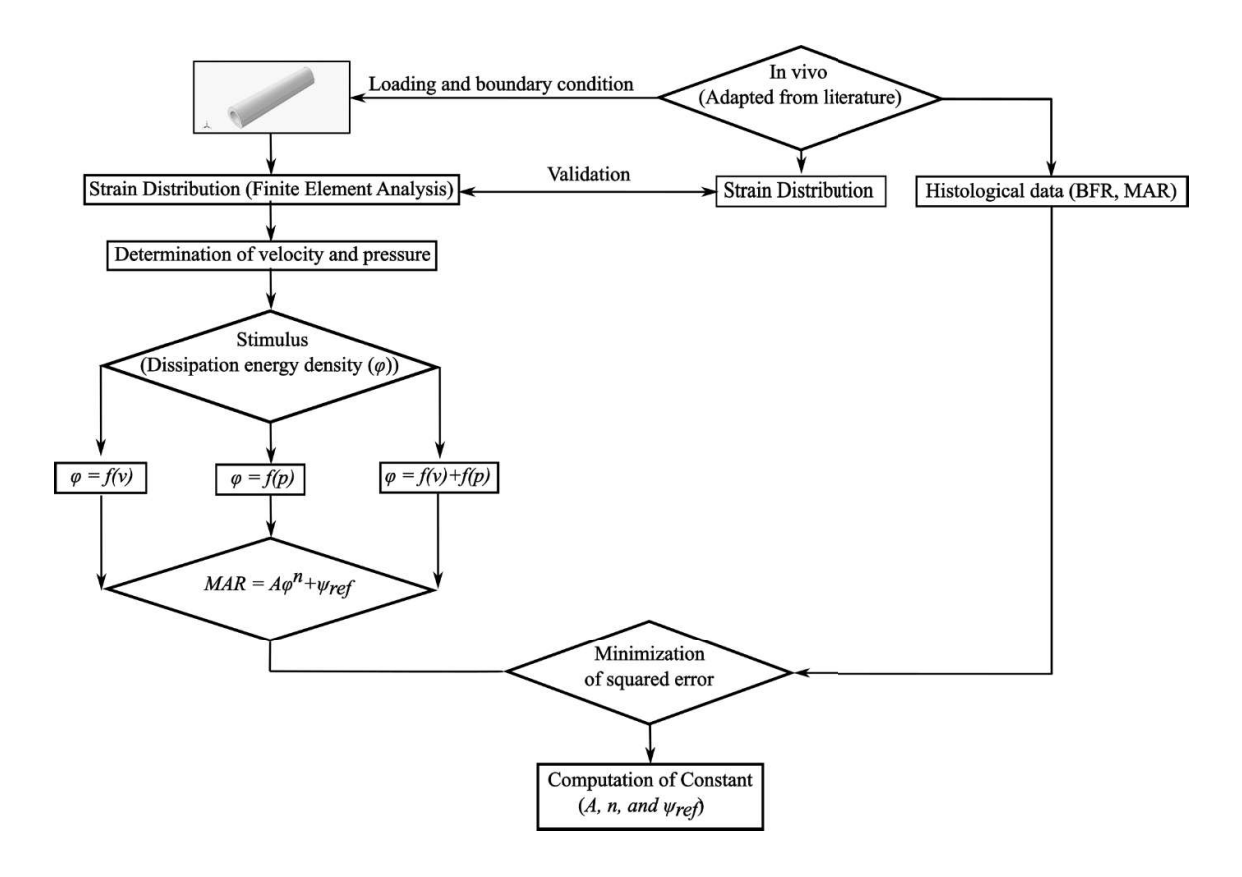


Figure 2.4 Bone adaptation algorithm flowchart.

The MAR is a critical parameter in assessing bone health, as it measures the mineralization rate of bone tissue. Overall, incorporating dissipation energy into the measurement of mineral apposition rate represents a significant advancement in our understanding of the complex process of bone mineralization. It may lead to the development of new diagnostic tools for bone-related diseases, such as osteoporosis. The potential application of this novel derivation in bone health research might be significant (96). However, despite its advantages, the derived model has limitations, such as its focus solely on measuring the Mineral Apposition rate (MAR) for lamellar bone formation without accounting for woven bone formation and bone resorption.

Chapter 3 – Predicting Site-Specific Cortical Bone adaptation:

Role of Fluid flow

Abstract

Osteoporosis affects healthy bone by disrupting its (re)modeling process, ultimately reducing mechanical properties. Mechanical loading has been shown to mitigate this bone loss by stimulating osteogenesis and reducing resorption. The strain is considered a primary stimulus for osteogenesis; however, the literature on in vivo studies highlighted that tissue strain cannot elicit a response from osteocytes, leading to new bone formation on the endocortical and periosteal surfaces. It suggests that another stimulus, such as load-induced fluid flow, may drive bone formation behavior on both surfaces. The permeability of the lacune-canalicular structure regulates the fluid flow and might be responsible for distinct fluid flow distribution at the cortical surfaces. Accordingly, this study presents a poroelasticity-based computational model that estimates the fluid velocity and the dissipation energy density due to fluid flow, coupled with a novel mathematical framework derived in Chapter 2. The model accurately predicts the new bone formation at the endocortical surface but underestimates at the periosteal surface. The model proposes that fluid flow alone is insufficient to simultaneously predict the behavior of the periosteal and endocortical surfaces.

Keywords: Mineral Apposition Rate, Bone Formation Rate, Lacune canalicular porosity, dissipation energy density, permeability, etc.

3.1 Introduction

Finding the reasons for bone adaptation to mechanics has been an object of research for the last 45 years. Initially, the mechanical strain-based stimulus was thought to be responsible for bone adaptation (56)(97)(98). For example, Rubin and Lanyon show that dynamic loading encourages new bone formation in a region of high mechanical strain (56). Several

mathematical models have been developed considering strain or strain energy density as a stimulus for bone adaptation (78)(82)(99)(100). For example, the strain-based computational model developed by Prasad and Goyal (78) predicts the new bone sites on the periosteal surface for different loading scenarios. However, this model has not anticipated endocortical osteogenesis. Similarly, Tiwari and Prasad (82) developed a computational model for an in vivo cantilever loading protocol. It made a good prediction for periosteal bone apposition; however, they highlighted that strain alone could not predict the new bone formation at the endocortical surface. This implies that other secondary stimuli derived from mechanical loading contribute to bone adaptation at the cortical surface, apart from strain. This lack of correlation between site-specific new bone formation at both cortical surfaces and strain proposes that other or secondary stimuli, such as fluid flow, maybe a potential stimulus of osteogenesis.

In fact, in the growing body of research data, fluid flow through the lacunae canalicular bone network has been shown to sense the mechanical environment, suggesting a prominent role in bone adaptation (75)(101). Lacunae canalicular porosity, which permeates the bone tissue, is a porous network of micro-sized lacune connected by canaliculi channels. Osteocytes reside in the lacunae; their processes pass through the canaliculi channels and are combined to form a cellular network, as shown in Fig. 3.1. The high stiffness of bone does not let osteocytes stretch significantly to sense the mechanical deformation of bone, resulting in the hypothesis of the strain amplification theory that involves fluid flow in the Lacunae Canalicular Network (LCN) (63). This hypothesis states that LCN porosities also deform when bone deformation occurs, resulting in a flow of interstitial fluid that exerts shear stress on the osteocytes. Moreover, in vitro studies have also confirmed that fluid flow has the potential to stimulate osteogenic activities at the cellular level (102)(61). Fluid flow through LCN was demonstrated experimentally by Knothe et al. using a tracer method, which shows that load-induced fluid

flow enhances the transport of tracers compared to diffusion (103). Even some fluid flow-based numerical studies suggested that bending-induced fluid flow may potentially predict new bone formation at both cortical surfaces (76)(77).

Accordingly, we conducted the finite element analysis, which simulated the experimental data of Berman et al. (95) and utilized the theory of poroelasticity to estimate the fluid velocity. This estimated fluid velocity calculates dissipation energy density, a stimulus of osteogenesis. This finite element-based model is coupled to the novel mathematical formulation derived in Chapter 2, predicting new bone formation at the periosteal and endosteal surfaces. Note that the derivation of MAR is based on a simplified viscoelastic beam with axial loading only. We hypothesize that this derivation can be extended to the microscopic bone, where osteocytic cells reside in the pore and experience fluid flow. Accordingly, φ_i in Eq. (2.17) is the dissipation energy density due to fluid flow.

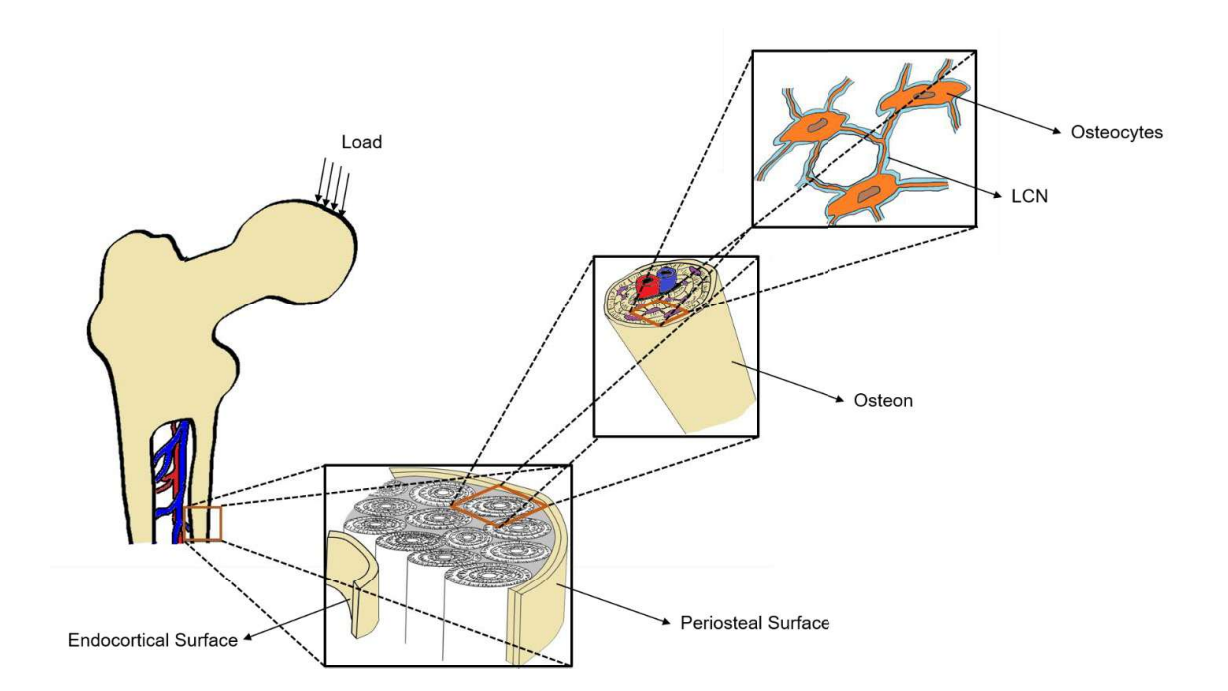


Figure 3.1 Mechanical loading of bone leads to the transmission of load to the cellular level via fluid flow in lacunae canalicular porosity.

3.2 Methods

3.2.1 Finite Element Model

We used the poroelastic finite element model to compute fluid velocity and pore pressure in the bone for a given loading. The commercial ABAQUS software (Dassault Systèmes, Simulia Corp.) was used for this purpose.

3.2.2 Bone Geometry

Analysis of the whole bone would have been ideal. However, the poroelastic modeling of an entire bone is computationally very costly in terms of the simulation time. In addition, quite a few works in the literature have studied bone response on the mid-cross section of the bone; for example, studies by Berman et al. (95), Willie et al. (104), Birkhold et al. (105), Srinivasan et al. (99), Weatherhold et al. (106), etc. In view of this, as shown in Fig. 3.2, we used a prismatic beam of 5 mm in length with a cross-section similar to that of a tibial mid-diaphysis, located 45% of the total bone length from the proximal growth plate of an 8-week-old mouse. The cross-section has been adapted from Berman et al. (95).

3.2.3 Porosity and Permeability of Bone

The cortical bone displays distinct porosities across scales, including vascular, lacune canalicular, and collagen apatite porosity (107). The osteonal and Volkmann canals (order 20 µm), which contain the vasculature, nerves, and bone fluid, are called vascular porosity (PV). The bone fluid pressure in the PV cannot generally exceed the local blood pressure as the vessels would collapse. All the space in the lacunae and the canaliculi is called the lacunae canalicular porosity (order 0.1 µm). The porosity within the space between collagen and hydroxyapatite crystallites is called collagen apatite porosity (order 10 nm). The fluid movement in this space is negligible due to the interaction with the ionic crystals.

We focused on lacunae canalicular porosity only as it is believed to play a crucial role in bone adaptation due to osteocytes in lacunae and their processes in canaliculi (63). For simplicity, we assume the porosity to be homogeneous, and accordingly, the continuum theory of poroelasticity has been used for analysis.

Even though bone intrinsic permeability has been extensively explored in the last decade, the computational and experimental estimation of intrinsic permeability ranges between $10^{-18} - 10^{-22}$ m² and $10^{-22} - 10^{-25}$ m², respectively (108)(109)(110)(63)(111). Experimentally measuring the relaxation time provides a means of determining the permeability value (112)(110). Pereira et al. (76) estimated the intrinsic permeability of order 10^{-22} m² for the previously estimated relaxation time of 6.76 sec by Zhou et al. (113). For this simulation, the permeability of the bone was considered to be $3x10^{-22}$ m², which is approximately the geometric mean of the entire range of permeability values $(10^{-25} - 10^{-18}$ m²) found in the literature. This order of permeability $(10^{-22}$ m²) confirms both experimental and theoretically derived values.

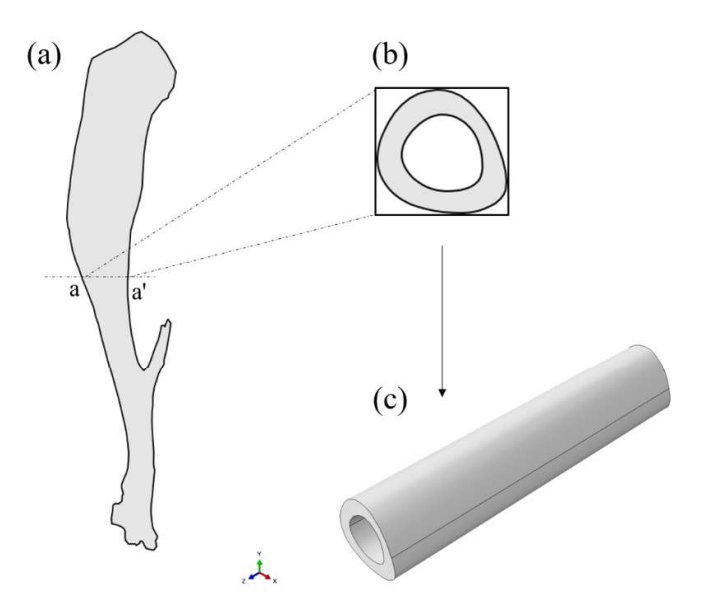


Figure 3.2 Pictorial representation of (a) 8-week-old C57BL/6 mouse tibia with (b) an idealized cross section at section a-a' (adapted from Berman et al. (95)), (c) A simplified prismatic beam developed with a cross-section similar to the section at a-a'.

3.2.4 Permeability of Bone Surface

There is no consensus about the permeability of the periosteum. Evans et al. have experimentally determined the permeability of the periosteum to be 10⁻¹⁷ m² ex-situ and thus suggested that the periosteum be highly permeable (114). Carriero et al. (77) have used the permeability measured by Evans et al. (114) and shown that periosteal permeability of an order of 10⁻¹⁷ m² (which is more than the permeability of the bone) significantly overestimates the periosteal adaptation. In contrast, Li et al. have indicated that the periosteum (external bone surface) is impermeable (115). Steck et al. characterized the periosteum as relatively impervious and the endosteum (inner surface of the bone) as relatively permeable (116). Price et al. (117) also experimentally measured the high circumferential fluid velocity in situ, which according to Zhou et al. (113) indicates the periosteum's very low (negligible) permeability. Given the above studies, we assumed the permeability of the periosteum negligible. Endocortical surfaces, on the other hand, are considered fully permeable in accordance with the literature.

3.2.5 Loading and Boundary Conditions

To predict the site-specific new bone formation at both cortical surfaces, we modeled the invivo study by Berman et al. (95). This study was chosen because it provides data on new bone formation at both the periosteal and endocortical surfaces. The loading was referred to as a mid-strain regimen, where 8-week-old C56BL/6J mice were subjected to axial loading of 10.6 N, engendering 2050 με on the anteromedial periosteal surface of the midsection. The loading profile consists of 4 haversine waveforms at a frequency of 2 Hz followed by a rest of 3 seconds at the maximum load and repeated the loading profile 55 times a day. The loading was applied for 14 days, with three days of loading followed by a rest of one day. We simulated the above loading protocol by setting zero displacements to the nodes at one end of the beam and eccentric compressive loading at the other to induce the strains on the beam's mid-cross-section, similar

to the tibial midsection strains in the experimental setup. The load was applied to create a maximum axial strain of 2050 μE at the anteromedial surface and a posterior-to-anterior axial strain ratio of 1.5-2 (118).

The boundary conditions of impermeable and permeable periosteal and endosteal surfaces, respectively, were implemented in the model by setting zero pressure, i.e., (p = 0), and zero flow, i.e., $(\nabla p. r = 0)$ at the endocortical and periosteal surfaces, respectively. Along with these conditions, the beam's two ends are also set as impermeable $(\nabla p. x = 0)$ as the end cross-sections are not expected to affect the primarily planer fluid flow at the mid-section of the beam, where all the measurements are done.

3.2.6 Other Details

After conducting the convergence study, the beam is meshed with 81600 C3D8RP (Continuous 3 Dimensional 8-noded Reduced-integration Pore-pressure hexahedral) elements with an average distance of 21 µm between the nodes, about 15% of the cortical thickness, as shown in Fig. 3.3. A minimum time increment (step size) of 2x10⁻³ sec was used for guaranteed convergence. The material properties presented in Table 3.1 were taken directly from Zang and Cowin (119) and Cowin (107), except for the permeability of the bone.

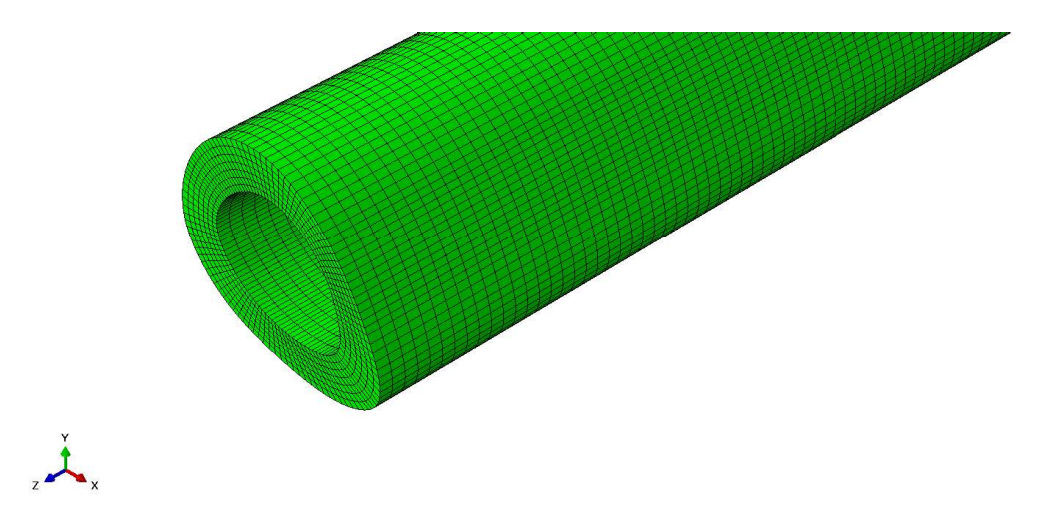


Figure 3.3 Finite-element meshing of the prismatic beam having a cross-section similar to the midsection of a mouse tibia.

Table 3.1 Material Properties used for simulation (adapted from (Zang and Cowin (119)) and (Cowin (107)).

Property	Bone	Units
Young Modulus (E)	12000	MPa
Drained Poisson Ratio (v)	0.3	
Bulk Modulus Solid (k _s)	17000	MPa
Bulk Modulus Liquid (k _f)	2300	MPa
Porosity (n _p)	5%	
Intrinsic Permeability	3x10 ⁻²²	m ²
Specific Weight (γ)	9.8×10^3	Nm ⁻³
Dynamic Viscosity (μ)	8.9x10 ⁻²	Pa s

3.2.7 Dissipation Energy Density

3.2.7.1 Dissipation Energy Density – Due to Fluid Flow

The energy dissipated due to the viscous nature of fluid over a loading cycle time period (T) can be considered a stimulus and is defined as (83):

$$DE_{v} = \int_{0}^{T} \frac{1}{2} (n_{p} \boldsymbol{v}_{fl}) \cdot \left(\frac{\boldsymbol{k}}{\mu}\right)^{-1} \cdot (n_{p} \boldsymbol{v}_{fl}) dt$$
(3.1)

where DE_v is the dissipation energy density per cycle due to the fluid flow, n_p is the porosity, v_{fl} is the fluid velocity, k is the intrinsic permeability of the cortical bone tissue, and μ is the kinematic viscosity of the fluid in LCN. The value of DE_v is computed at the integration point of each element.

3.2.7.2 Zone of Influence

Osteocytes form the network structure in bone by connecting their processes via gap junctions (120). The processes of osteocytes also form the gap junctions with osteoblasts/lining cells on the bone surface. It suggests that the osteocytes in the LCN detect the mechanical cues, convert them into biochemical signals, and transmit them to the osteoblasts on the periosteal and endocortical surfaces through diffusion (41). This communication is implemented in Prasad and Goyal as diffusion (78). However, it has been modeled differently in the existing models, where a spherical zone of influence is considered instead (83)(75)(121). We considered the zone of influence for its simplicity, shown schematically in Fig. 3.4, which suggests that osteocytes closer to the bone surface contribute more than the osteocytes away from the surface. Averaging was weighted with the exponential function w(x).

$$w(x) = \exp(-5|x|/R) \tag{3.2}$$

where |x| is the distance between the node of interest i at the surface (where total dissipation energy density is being computed) and the integration point of the elements in the zone of influence (contributing to the total dissipation energy density at the node of interest).

We assessed the effect of various R values, viz – $100 \, \mu m$, $150 \, \mu m$, and $170 \, \mu m$, on new bone distribution. The most optimal fit was observed at $150 \, \mu m$. As a result, we chose to adopt R as $150 \, \mu m$, a measure that approximately coincides with the cortical thickness of mouse middiaphysis.

The modified stimulus due to fluid flow at node i is calculated as a weighted average over the finite region (spherical zone of influence of radius 150 μm), assuming all elements have approximately the same volume:

$$\overline{(DE_v)_i} = \frac{\int DE_v w(x) dV}{\int w(x) dV} = \frac{\sum_{j=1}^n (DE_v)_j (w(x))_j}{\sum_{j=1}^n (w(x))_j}$$
(3.3)

where j represents the j^{th} element lying inside the zone of influence, and V is the volume of the zone of influence.

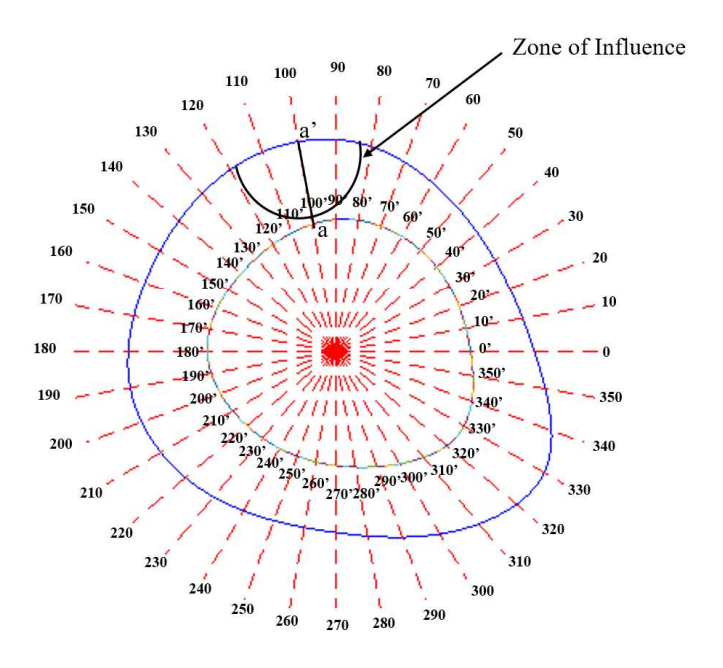


Figure 3.4 Cross-section of the mid diaphysis of 8-week-old C57Bl/6J mouse tibia showing zone of influence (solid circular arc), line a-a', and radial lines (red, dashed lines) (adapted from Fig. 4(b) of Berman et al. (95)).

3.2.8 Osteogenesis as a Function of Fluid Flow

To measure the site-specific new bone formation, we divided the circumference of the midcross section of the beam into 360 points by the radial lines passing through the centroid of the cross-section. The lines intersecting the periosteal and the endocortical rim were numbered i =1 - 360 and i = 0' - 360' in an anti-clockwise direction, respectively. For clarity, these lines are shown as dashed red lines at every ten degrees in Fig. 3.4. At these intersection points at periosteal and endosteal surfaces, we estimated the site-specific osteogenesis or site-specific mineral apposition rate (MAR). In addition, the bone formation rate (BFR) is computed from the mineral apposition rate (MAR), as done by Prasad and Goyal (78). Following Eq. (2.17), we hypothesized that the quantity that predicts the spatial new bone thickness per unit of time on the considered section and surface (endocortical and periosteal) is given by

$$MAR_{i} = A(\varphi_{v_{i}})^{n} - \psi_{ref}, where \begin{cases} \varphi_{v_{i}} = \overline{DE_{v_{i}}} * N * d \\ \psi_{ref} = A(DE_{ref} * N * d)^{n} \end{cases}$$
(3.4)

where MAR_i is the mineral apposition rate at a given node i and φ_{v_i} is the corresponding stimulus due to fluid flow. A is the remodeling rate to be determined, N is the number of loading cycles, and d is the number of loading days. The power of n is another constant to be determined, which, according to Eq. (2.16), is expected to be around 0.5. ψ_{ref} may be considered as the reference MAR existing in the absence of exogenous mechanical loading. DE_{ref} is the threshold/reference value of dissipation energy density for one cycle, and $\overline{DE_{v_i}}$ which is the actual dissipation energy density due to the external loading must exceed it (i.e., the reference) for new bone formation to occur. Equation (3.4) can fit the MAR data for the endocortical surface as follows.

$$MAR_{i}^{es} = A(\varphi_{v_{i}}^{es})^{n} - \psi_{ref} \text{ where } \begin{cases} \varphi_{v_{i}}^{es} = \overline{DE_{v_{i}}}^{es} * N * d \\ \psi_{ref} = A(DE_{ref} * N * d)^{n} \end{cases}$$
(3.5)

where es represents the endocortical surface.

The unknown model parameters, i.e., A, n, and ψ_{ref} can be estimated by minimizing the error squared between the predicted mineral apposition rate (MAR_i^{es}) and the corresponding experimental value $(r.MAR_i^{es})$ at nodes i on the endocortical surface using Eq. (3.6).

$$F(A, n, \psi_{ref}) = \sum_{i=1'}^{361'} (r.MAR_i^{es} - MAR_i^{es})^2$$
 (3.6)

Here $r.MAR_i^{es}$ stands for "relative MAR", calculated by subtracting the natural MAR of contralateral bones from the MAR of the loaded bone. Thus, $r.MAR_i^{es}$ represents the MAR attributed solely to the mechanical loading.

The estimated MAR at a given node i is then multiplied by the time interval (t) between the two calcine labels, as obtained from an in-vivo study by Berman et al. (95). A line with a length equal to $(MAR_i * t)$ is drawn perpendicular to the surface on the same node. The exact process is repeated for all the other nodes on both periosteal and endocortical surfaces. Finally, the endpoints of all the lines are connected to form the surface of the newly formed surface.

3.2.9 Statistical Analysis

The statistical analyses are the same as those adopted by Prasad and Goyal (78). To compare the numerical predictions to the experimental data, the total new bone area formed per unit of time is obtained by integrating the MAR (i.e., new bone thickness formed per unit of time) over the circumference of each of the two bone surfaces at the cross-section under study. The bone formation rate per unit bone surface (BFR/BS), or simply, bone formation rate (BFR), is obtained by dividing the new bone area formation rate by the total perimeter of the surface in consideration. Then, the Student's t-test (a one-sample, two-tailed t-test) was used to compare the bone formation rate (BFR) predicted by the mathematical model to the corresponding experimental value. The mineral apposition rate (MAR) is recorded on a circular scale, and therefore, Watson's U² test is used to compare the experimental and simulated MAR

(122)(123). The Student's t-test and Watson's U² test were carried out using MATLAB (MathWorks Inc.) programming.

3.3 Results

The model simulates osteogenesis as a function of fluid flow alone at cortical surfaces. The computed strain distribution (Fig. 3.5a) for the mid-strain loading protocol of Berman et al. (95) shows that the maximum strain induced at the anteromedial surface is 2056 μ E, which is close to the experimental strain of 2050 μ E. The velocity is negligible at the periosteal surface, which reaches the maximum at the endocortical surface (see Fig. 3.5b). The simulation is done for multiple loading cycles. There is an initial transient during the first 2-3 cycles, beyond which fluid flow and pore pressure gain steady-state and follow sinusoidal profiles with the same frequency as the applied load (83). We estimated the dissipation energy density $(\overline{(DE_v)_i})$ for one cycle at the end of the initial transient, as given by Eq. (3.3) for fluid flow. Then, the results were extrapolated according to the number of loading cycles and the number of days in the experimental protocols to calculate the total dissipation energy density (φ_{v_i}).

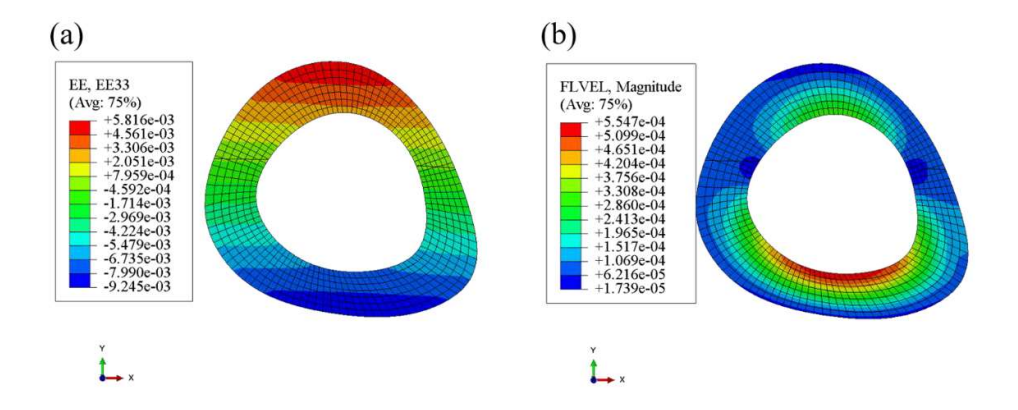


Figure 3.5 (a) Longitudinal strain distribution adapted from Berman et al. (95), and (b) velocity distribution (mm/sec) on the bone cross-section.

Figure 3.6 shows the plot of dissipation energy density due to fluid flow along the cortical thickness (shown by line a-a' in Fig. 3.4) of the beam mid-cross section. The dissipation energy

density due to fluid flow follows the trend of the fluid velocity, i.e., it is maximum at the endocortical surface and reaches its minimum value at the periosteal surface.

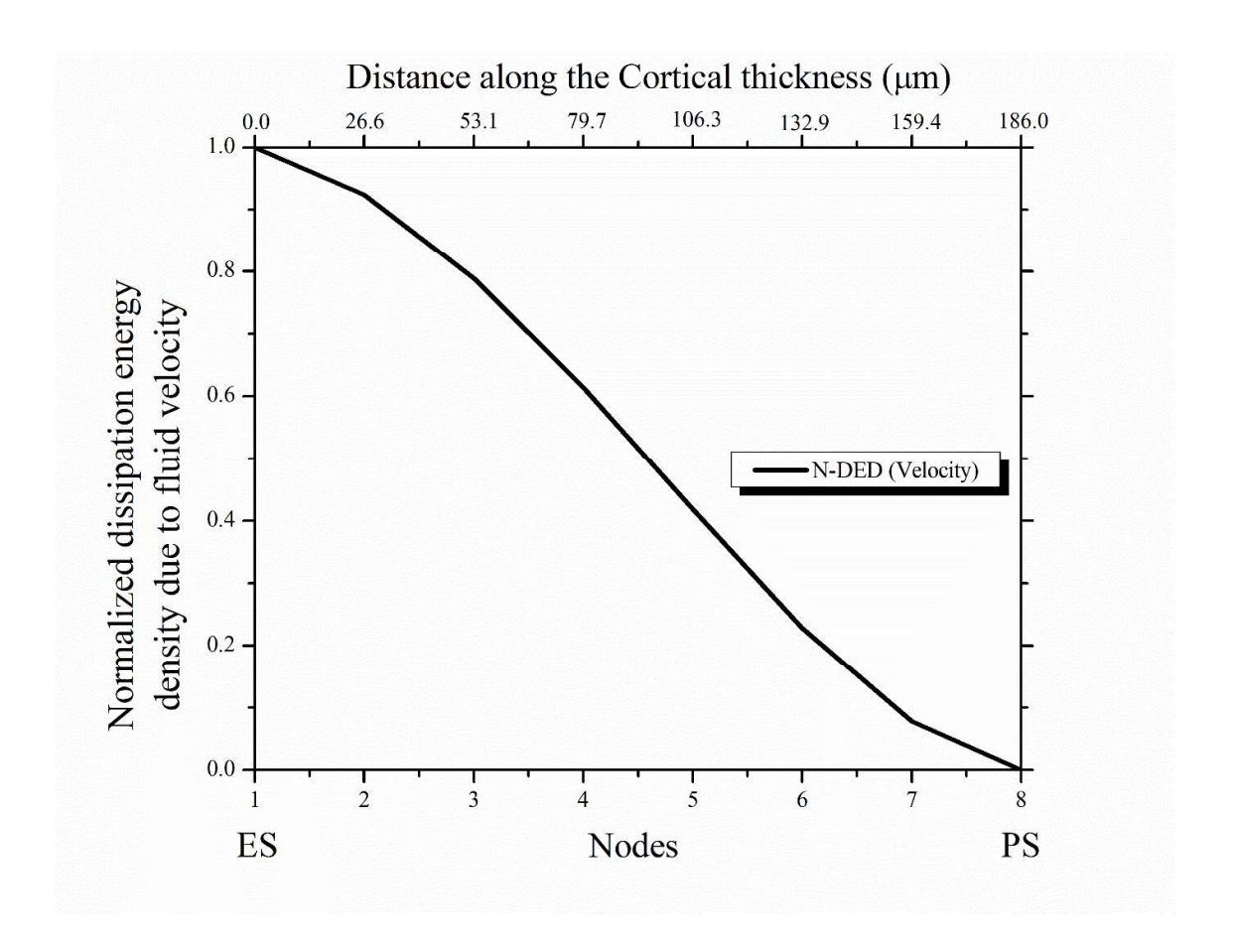


Figure 3.6 Dissipation energy density (DED) due to fluid velocity along the radial line a-a' on the anterior side of the mid-cross section of the beam (see Fig. 3.4), progressing from the endocortical surface (ES - Node 1) to the periosteal surface (PS - Node 8).

3.3.1 Osteogenesis as a Function of Fluid Velocity

The potential of fluid flow to predict osteogenesis at both cortical surfaces has been investigated here. The values of parameters that fit the observed new bone thickness at the endocortical surface of Berman et al. and relate to the dissipation energy density only due to fluid flow are as follows (95): $A = 184.94 \ \mu \text{m}/\sqrt{\text{N}/\text{day}}$, $n = 0.40 \ \text{and} \ \psi_{ref} = 0.37 \ \mu \text{m}^3/\mu \text{m}^2/\text{day}$. Corresponding to the computed ψ_{ref} , DE_{ref} comes out to be $3.86 \times 10^{-10} \ \text{N}\mu \text{m}/\mu \text{m}^3$. Similar to

the in vivo new bone distribution at the endocortical surface (Fig. 3.7a), the model also predicted the site-specific new bone formation at the anterior and posterior sides of the endocortical surface (Fig. 3.7b). The BFR calculated by the model is $0.63 \, \mu m^3/\mu m^2/day$ at the endocortical surface, which is not significantly different from the experimental BFR of $0.59 \pm 0.14 \, \mu m^3/\mu m^2/day$ (p-value = 0.81, t-test). Additionally, the statistical significance of site-specific MAR at the endocortical surface is measured using Watson's U² test, which shows that the computed MAR is not significantly different from the experimental MAR (p-value = 0.59, Watson's U² test). However, the predicted BFR of $0.07 \, \mu m^3/\mu m^2/day$ at the periosteal surface is significantly different from the experimental BFR of $0.93 \pm 0.16 \, \mu m^3/\mu m^2/day$ (p-value = 0.00043, t-test). The site-specific new bone distribution at the periosteal surface (see Fig. 3.7b) is also significantly different from the experimental MAR (p-value = 0.0015, Watson's U² test).

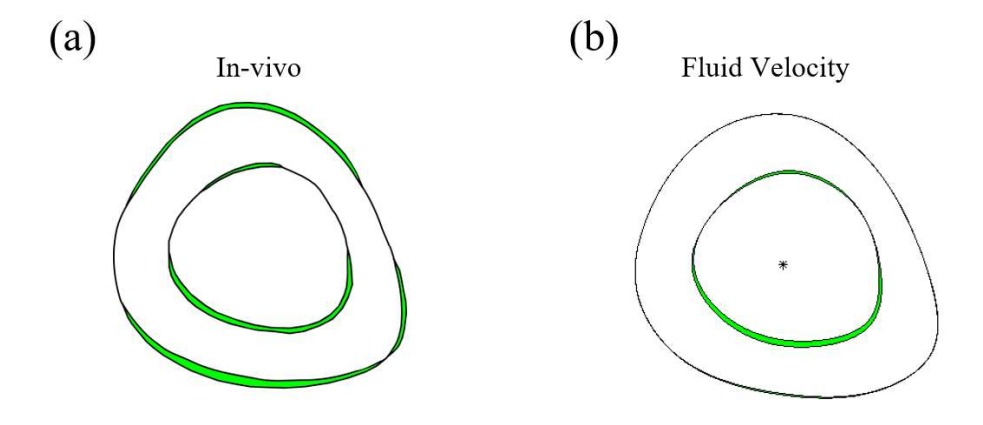


Figure 3.7 (a) In vivo, new bone formation at the cortical surfacers for mid-strain loading protocol (adapted from Berman et al. (95)), and the corresponding numerically predicted new bone distribution as a function of (b) fluid flow.

3.4 Discussion

We employed a finite element analysis of bone based on the in vivo study by Berman et al. (95) to predict the fluid velocity, which was subsequently used to estimate the dissipation

energy density. This is followed by estimating new bone distribution at the cortical surfaces through a novel mathematical framework. The maximum fluid velocity at a peak load of 2050 μ E (medial surface) is 0.55 μ m/s, which is of a similar order to the velocity measured by other *in-silico* models (76)(77). For instance, Pereira et al. (76) predicted an axial load-induced fluid velocity of 0.15 μ m/s, while Carriero et al. (77) estimated it to be around 0.1 μ m/s. The difference in maximum fluid velocity is because of the difference in permeability of the periosteum; we have taken this permeability to be zero, whereas the two referred studies have taken it to be 10^{-17} m². We could not find a study in the literature where fluid velocity was estimated with zero periosteal permeability.

It is evident from the results of the developed mathematical framework (based on dissipation energy density due to viscous fluid flow) that fluid flow alone as a stimulus predicts osteogenesis only at the endocortical surface. Conversely, it underestimates the site-specific bone formation at the periosteal surface. This was because of the drained and undrained conditions, respectively, of the endocortical and periosteal surfaces, resulting in high fluid flow and negligible fluid flow at the two surfaces (Fig. 3.7b, c) (112)(124). The above observation follows the existing literature. For instance, the Carriero et al. (77) study highlights that the fluid flow correctly predicts the new bone distribution at the endocortical surface only. In addition, this study agrees with the previous research by Tiwari et al. that a single stimulus is insufficient to predict new bone distribution at both cortical surfaces (82).

Past research has suggested that different mechanical stimuli initiate different mechanisms of mechanotransduction. For example, tissue strain induced interstitial fluid flow, exerting drag forces on the tethering fibers that attach osteocyte cell processes to mineralized tissue, generating strain in the osteocyte process and releasing different signaling molecules such as prostaglandin (PGE2) and NO to communicate with osteoblasts to initiates new bone formation (81). Hence, incorporating fluid flow may be helpful. However, the results indicate that fluid

flow cannot induce new bone formation at both cortical surfaces. Thus, this indicates a necessity for integrating another stimulus to forecast osteogenesis accurately at both cortical surfaces.

Discovering another stimulus, whether independently or in conjugation with fluid flow, capable of predicting new bone formation at both cortical surfaces has posed a significant challenge. Therefore, the next chapter delves into exploring these secondary stimuli that have the potential to carve a desired site-specific new bone formation.

3.5 Conclusion

This study presents a poroelasticity-based mathematical model based on dissipation energy density due to viscous fluid flow to measure the site-specific bone distribution (MAR) at both the cortical surfaces (periosteal and endocortical). The model predicts new bone distribution at the endocortical surface but underestimates the periosteal surface. The key finding is that fluid flow is negligible at the periosteal surface, and hence, something other than fluid flow must induce new bone formation.

Chapter 4 – Predicting Site-Specific Cortical Bone Adaptation:

The Role of Pore Pressure Alone and in Combination with Fluid

Flow

Declaration: Some of the contents of this chapter are published in Bone Reports under the title 'Derivation, validation, and prediction of loading-induced mineral apposition rates at endocortical and periosteal bone surfaces based on fluid velocity and pore pressure.' https://doi.org/10.1016/j.bonr.2023.101729

Abstract

The capacity of bone to optimize its structure in response to mechanical loads has been widely observed. The mechanical load acting on a bone at the macroscopic level influences the bone cells, particularly osteocytes within the lacunae canalicular network (LCN). Osteocytes are responsive to various physical signals, including strain, interstitial fluid flow, and pore pressure. However, physiological tissue strain is known to be typically smaller than that required to induce bone formation directly. On the other hand, as per evidence provided by studies from the literature, models based on fluid flow alone cannot simultaneously predict bone formation at both the periosteal and endocortical surfaces. This suggests that another component of the osteocyte's mechanical environment, such as pore pressure, may play an essential role in bone adaptation alone or in combination with other stimuli, such as tissue strain or interstitial fluid flow. In vitro experiments have also confirmed that osteocytes respond to cyclic pore pressure and, thus, have a mechanism to sense the pressure, possibly because of its viscoelasticity.

The central hypothesis, mathematically derived in Chapter 2, shows that the Mineral Apposition Rate (MAR) is proportional to the square root of the dissipation energy density minus its reference value. Dissipation energy density, being irreversible work done per unit

volume, has been successfully used as a more significant stimulus to incorporate all of the parameters of mechanical environments of the LCN, such as waveforms of both fluid velocity and pore pressure, the number of loading cycles. This hypothesis has been successfully tested/validated for both endocortical and periosteal surfaces with respect to an in-vivo study on mouse tibia, which is available in the literature. The constant of proportionality and the reference/threshold value of the dissipation energy density are determined through a nonlinear curve fitting.

Computational implementation of the mathematical model has been done through a poroelastic finite element analysis of bone, where the bone is assumed to be porous and filled with fluid, with a boundary condition that the periosteum is impermeable to the fluid and the endosteal surface maintains a reference zero pressure. This work also provides evidence for these assumptions to be true based on the state-of-the-art literature on related experimental studies. The currently developed model shows that the bone uses these conditions (assumptions) to its advantage, as the greater stimulus, i.e., the dissipation energy due to both fluid flow and pore pressure, are of a similar order at both the surfaces and hence osteogenesis of the same order at both the surfaces.

As a bottom line, the resulting model is the first of its kind, as it has been able to correctly predict MAR at both endocortical and periosteal surfaces. This study thus significantly advances the modeling of cortical bone adaptation to exogenous mechanical loading.

Keywords: Site-specific mineral apposition rate (MAR), Dissipation energy density, Interstitial fluid flow, Pore pressure, and Endocortical and Periosteal surfaces.

4.1 Introduction

Three papers in the late 1900s paved the way for load-induced fluid flow in LCN as the primary stimulus for bone adaptation (125)(126)(63). Weinbaum et al. hypothesized that fluid shear on

osteocyte processes in LCN initiates a cellular response (63). Cowin et al. suggested LCN as the site of the strain-generated potential (125). Klein-Nulend et al. (126), in their in vitro study, showed osteocyte sensitivity to fluid flow shear stresses. Based on these theories, fluid flow is believed to predict new bone formation, and accordingly, several fluid flow-based computational models emerged. For instance, Kumar et al. (83) devised a viscous dissipation energy-based mathematical model to predict new bone formation using a solid rectangular beam rather than the actual bone. Subsequently, Kumar et al. (75) tested this model for the adaptation of rat ulna. However, during validation against experimental data, the focus was solely on the periosteal surface and did not include validation on the endocortical surface. Dissipation energy density used in that, however, proved very useful and intuitive to incorporate almost all types of mechanical stimuli. Periera et al. (76) introduced the fluid velocity-based mathematical model to anticipate changes in cortical thickness, which does not provide quantitative details of the new bone formation individually at the periosteal and endocortical surfaces. Carriero et al. (77) tried to correlate the peak fluid velocity to the new bone formation; however, the peak fluid velocity and the new bone formation do not coincide at the endocortical surface. On the other hand, periosteal surface bone formation was greatly overestimated, which (according to the authors) was a result of using the high permeability value of the periosteum in accordance with the ex-situ measurement of permeability by Evans et al. (114), who had also found the periosteum permeability to be stress-dependent and direction-dependent. Therefore, it is also difficult to implement this highly nonlinear behavior of the periosteal permeability in the bone adaptation model.

Tol et al. (79) also developed a fluid velocity-based theoretical model. Here, new bone formation is also not found to vary monotonically with the fluid velocity at the periosteal and endosteal surfaces. To our knowledge, there is no example in the literature where both endocortical and periosteal bone surfaces can be predicted simultaneously by fluid flow alone.

It is, therefore, essential to understand the mechanical environment of osteocytes inside the LCN and re-analyze it.

Osteocytes residing in LCN are enveloped by fluid and anchored to mineralized tissue through tethering fibers. Additionally, these processes are connected to the projection protruding from the canalicular wall through $\alpha_v \beta_3$ integrin molecules, as depicted in Fig. 4.1a (127). Tissue strain in the whole bone under the physiological loading is typically less than 0.2% (128)(56). However, this strain must be an order higher for any intracellular response to occur (61). When the mechanical load is applied to the bone, it induces a pressure gradient, leading to canalicular fluid flow. This fluid flow, in turn, exerts drag forces on these tethering fibers. This drag stretches the osteocyte's process membrane outward, resulting in radial strain and leading to the deformation of the canalicular process, as illustrated in Fig. 4.1b (66). Intuitively, pore pressure is also expected to radially stretch/compress the osteocyte's process, depending on the tensile/compressive environment. Thus, osteocytes will sense the combined effect of fluid flow and pore pressure. The multitude of in vitro studies confirms that fluid flow stimulation prompts osteocytes to release biomolecules (Prostaglandin E2, Ca2+, etc.), culminating in osteogenesis (86)(126)(87). Some in vitro studies demonstrate that besides interstitial fluid flow, cyclic pore pressure also has the potential to induce osteogenesis (86)(126)(129)(89). Weinbaum et al. (63) and Scheiner et al. (124) respectively established that fluid flow on the osteocyte process and pore pressure generated under physiological loading conditions are adequate for osteocyte stimulation. Given the limitation of fluid flow alone, investigating a combination of fluid flow and pore pressure became imperative.

The chapter 2 introduces an innovative approach for deriving the Mineral Apposition Rate (MAR), considering bone as a viscoelastic material and utilizing dissipation energy as a critical factor. The derivation proposes that MAR is directly proportional to the square root of dissipation energy density minus a reference value, thus forming the central hypothesis to be

verified. Moreover, it is established that whether the material is characterized as viscoelastic or poroelastic, its deformation behavior will remain consistent (refer to Appendix A). Hence, dissipation energy density will remain the same regardless of whether the material is classified as viscoelastic or poroelastic. To validate this hypothesis, the dissipation energy density is computed based on the results (fluid velocity and pore pressure) of the Finite Element Analysis of the mouse tibia, which has been modeled as a poroelastic material. This dissipation energy density stemming from fluid flow and pore pressure, individually or in combination, is utilized to determine whether pore pressure alone or in tandem is necessary for predicting MAR at both cortical surfaces.

Additionally, a nonlinear curve fitting determines the constant of proportionality and the reference/threshold value of the dissipation energy density. The model successfully predicts the MAR obtained by the experiment at both endocortical and periosteal surfaces. Furthermore, the model also successfully predicts new bone formation for different load magnitudes.

The work advances the understanding of load-induced bone adaptation by establishing: (i) Pore pressure can also induce new bone formation, unlike the existing notion that fluid flow alone causes new bone formation, (ii) Pore pressure in combination with fluid velocity is a better predictor of MAR than fluid velocity alone, (iii) Dissipation energy density is a suitable stimulus as it can combine different types of stimuli such as fluid velocity and pore pressure into one scalar value. (iv) MAR is proportional to the square root of the dissipation energy minus a reference value. (v) The assumption that the periosteal surface is impermeable may be valid based on the literature and the outcomes of the developed model.

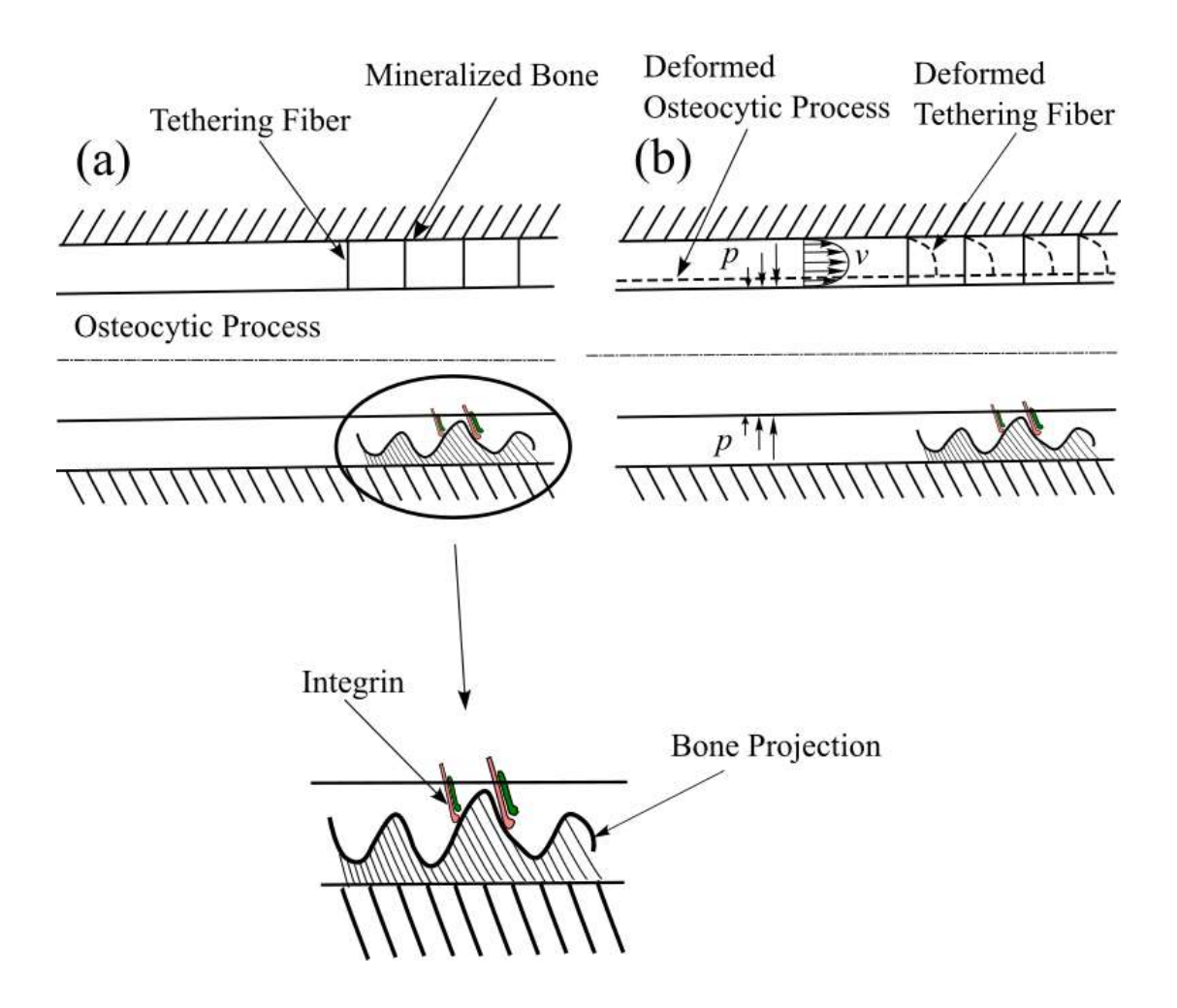


Figure 4.1 Schematic diagram of canaliculus, longitudinal osteocyte process passing through the fluid-filled canaliculus and the attachments of the process, (a) before and (b) after deformation (p and v represent pore pressure and fluid velocity, respectively).

4.2 Methods

4.2.1 Finite element model

We use the same poroelasticity-based model used in the previous chapter. However, for clarity, it is explained briefly here. We used a tabular beam of 5 mm in length with a cross-section similar to the 8-week-old mice's tibial mid-diaphyseal cross-section located 45% of the total bone length from the proximal growth plate of an 8-week-old mouse, which was adapted from Berman et al. (95). We used the finite element method to solve this problem in commercial ABAQUS software (Dassault Systèmes Simulia Corp.). The beam's outer and inner surfaces

corresponded to the periosteal and endocortical surfaces of mice tibia and, based on previous experiments, are defined as impermeable (115) and permeable (107). These boundary conditions were implemented in the model by setting the flow boundary condition, i.e., (p =0), and zero flow boundary condition, i.e., $(\nabla p. r = 0)$ at the endocortical and periosteal surface, respectively. The zero flow boundary condition was imposed by default on the endocortical surface. After conducting the convergence study, the beam was meshed with 81600 C3D8RP (Continuous 3 Dimensional 8-noded Reduced-integration Pore-pressure hexahedral element) elements. The material properties used in the simulations are presented in Table 3.1 in Chapter 3 and were taken directly from Zang and Cowin (119), except for the permeability of the bone. In this simulation, we consider only lacune canalicular porosity because it is believed that porosity at this scale, due to osteocytes in the lacunae and its processes in canaliculi, is essential for bone adaptation (63). The intrinsic permeability of LCN for this simulation was considered $3x10^{-22}$ m². To simulate the mid-strain loading protocol from the *in-vivo* study done by Berman et al., (95) eccentric loading was applied to the simplified beam, with the opposite end fixed as described in Section 3.2.5 of Chapter 3, ensuring it generates 2050 με at the anteromedial periosteal surface.

4.2.2 Dissipation Energy Density

4.2.2.1 Dissipation Energy at the Cellular Level

As discussed in the Introduction section, there are three cellular stimuli: pore pressure, tissue strain, and fluid flow. The energy dissipated at the tissue level under the action of the load can be considered as a combination of energy dissipation due to (i) viscous fluid flow, (ii) pore pressure, and (iii) strain exerted on the osteocytes. Hence, dissipation energy may be formulated as follows:

$$DE = |av + b\varepsilon + cp|^2 \tag{4.1}$$

where v, ε , and p are the fluid velocity, tissue-level volumetric strain, and pore pressure. a, b, and c are the constants. |x| denotes the amplitude of the quantity x.

However, the mechanical strain needed to activate the bone cells in culture is 10-100 times larger than the in-vivo bone strain (61). Hence, the effect of tissue-level strain on osteocytes is minimal and can be neglected. Thus, Eq. (4.1) may be rewritten as:

$$DE = |av + cp|^2 \tag{4.2}$$

As the periosteal and endocortical surfaces are assumed to be ideally impermeable and permeable, respectively, the fluid velocity is assumed to be negligible at the periosteal surface, whereas pore pressure is assumed to be zero at the endocortical surface. Accordingly, the final equation is the following:

$$DE = |av|^2 + |cp|^2 (4.3)$$

The above relation is also approximately true between endocortical and periosteal surfaces, as the pore pressure and fluid velocity are approximately orthogonal to each other because of the boundary conditions and the relation between them (130). The variation of pressure along the cortical thickness may be assumed to be approximately varying sinusoidally with a node at the endocortical surface and a peak at the periosteal surface, in accordance with the literature (130)(131)(119). The fluid velocity (e.g., a cosine function) is proportional to the gradient of the pore pressure (e.g., a sine function), and the resultant of the two (av and cp) can be obtained as the square root of the summation of the squares of amplitudes of the two (av and cp), in accordance with Eq. (4.3). Thus, the tissue-level total dissipation energy density will be a combination of dissipation energy density due to the fluid flow and that due to the pore pressure.

4.2.2.2 Dissipation Energy Density – Due to Fluid Flow Alone

The adaptation model, where bone formation is considered only, is as follows: In the literature, it has been shown that shear stresses on osteocytes can be a potential candidate for mechanotransduction. Therefore, the energy of the fluid in lacunae canalicular porosity getting dissipated due to its viscous nature under the application of load can be considered as a stimulus to capture the fluid flow on bone formation, as shown by Kumar et al. (83).

$$DE_v = \int_0^T \frac{1}{2} (n_p v_{fl}) \cdot \left(\frac{\mathbf{k}}{\mu}\right)^{-1} \cdot (n_p v_{fl}) dt$$

$$\tag{4.4}$$

where DE_v is the dissipation energy density per cycle due to the fluid flow, n_p is the porosity, v_{fl} is the fluid velocity, k is the intrinsic permeability of the cortical bone tissue, and μ is the kinematic viscosity of the fluid in LCN. The value of DE_v is computed at the integration point of each element.

4.2.2.3 Dissipation Energy Density – Due to Pressure Alone

Osteocytes, like other cells, can be modeled as a viscoelastic material that shows time-dependent behavior (132)(133)(134)(135). The pore pressure acting on the osteocyte varies along its thin and long osteocytic processes. This pressure acts only radially, allowing the cell process to expand/contract radially and longitudinally (even if an incompressibility condition, i.e., Poisson's ratio of 0.5, is applied), which will cause viscoelastic dissipation. In viscoelastic material, the hysteretic loss (dissipation energy density for one cycle) can be expressed as

$$DE = \pi G'' \left(\frac{\sigma_0}{|G^*|}\right)^2 \tag{4.5}$$

where $G^* = G' + iG''$ and σ_0 are the complex modulus of osteocyte and stress amplitude induced, respectively (93).

Assuming stress amplitude induced inside an osteocyte (σ_o) to be directly proportional to pressure amplitude (p_0) acting on the surface of the osteocyte, i.e., $\sigma_o \propto p_0$, dissipation energy density due to pressure acting on osteocytes can be estimated as

$$DE_p = cp_0^2 (4.6)$$

where c is the proportionality constant that needs to be determined. The value of DE_p is also computed at the integration point of each element

4.2.2.4 Zone of Influence

Osteocytes form the network structure in bone by connecting their processes via gap junction (120). The processes of osteocytes also form the gap junction with osteoblast and lining cells on the bone surface. These osteocytes detect the mechanical cues, convert them into biochemical signals, and transmit them to the osteoblasts via gap junctions to form new bone (41). Simulated this global behavior of osteocytes by considering the concept of the zone of influence, which suggests that osteocyte's contribution closer to the surface is greater than the contribution of osteocytes away from the surface (121). For simplicity, a spherical zone of influence was considered, and averaging was weighted with the exponential function w(x).

$$w(x) = \exp(-5|x|/R) \tag{4.7}$$

where |x| is the distance between the node of interest i at the surface (where total dissipation energy density is being computed) and the integration point of the elements in the zone of influence (contributing to the total dissipation energy density at the node of interest).

The value of R was set equal to 150 μ m, as in section 3.3.7.2. Therefore, the updated stimulus for bone adaptation at node i is defined by

The modified stimulus resulting from fluid flow and pore pressure at node i is determined by computing a weighted average across the finite region (spherical zone of influence of radius 150 μ m), assuming uniform element volumes:

$$\overline{(DE_v)_i} = \frac{\int DE_v w(x) dV}{\int w(x) dV} = \frac{\sum_{j=1}^n (DE_v)_j (w(x))_j}{\sum_{j=1}^n (w(x))_j}$$
(4.8)

$$\overline{\left(DE_p\right)}_i = \frac{\int DE_p w(x) dV}{\int w(x) dV} = \frac{\sum_{j=1}^n \left(DE_p\right)_j (w(x))_j}{\sum_{j=1}^n (w(x))_j} \tag{4.9}$$

where j represents the j^{th} element lying inside the zone of influence, and V is the volume of the zone of influence.

4.2.3 Osteogenesis as a Function of Pore Pressure

Several in vitro and in vivo studies have shown that hydrostatic pressure is essential in bone maintenance (136)(89). Hence, similar to the previous chapter, a site-specific model is developed to predict osteogenesis at the cortical surfaces; however, this time with pore pressure as a stimulus. To predict new bone formation, we modeled the same in vivo study by Berman et al. (95) as done in the previous chapter. The quantity that estimated the new bone distribution as a function of fluid pore pressure is given by:

$$MAR_{i} = A\left(\varphi_{p_{i}}\right)^{n} - \psi_{ref}, where \begin{cases} \varphi_{p_{i}} = \overline{DE_{p_{i}}} * N * d \\ \psi_{ref} = A\left(DE_{ref} * N * d\right)^{n} \end{cases}$$
(4.10)

where φ_{p_i} is the total dissipation energy density due to pore pressure at a given node i.

As the pore pressure is assumed to be zero at the endocortical surface (which will result in a negligible dissipation energy density), the values of the parameters A, n, and ψ_{ref} are estimated by fitting the new bone distribution at the periosteal surface as:

$$F(A, n, \psi_{ref}) = \sum_{i=1}^{361} (r.MAR_i^{ps} - MAR_i^{ps})^2$$
 (4.11)

where ps denotes the periosteal surface. $r.MAR_i^{ps}$ is the relative site-specific experimental MAR at a given node i, while MAR_i^{ps} is the computationally estimated site-specific MAR at the same node i.

4.2.4 Osteogenesis as a Function of Fluid Flow and Pore Pressure

We use the same in vivo data as in subsection 4.2.3 to estimate the site-specific new bone thickness at cortical surfaces as a function of fluid flow and pore pressure. The quantity that predicts the site-specific new bone formation at both surfaces is given by Eq. (4.12).

$$MAR_{i} = A \left(\varphi_{v_{i}} + \varphi_{p_{i}} \right)^{n} - \psi_{ref}, where \begin{cases} \varphi_{v_{i}} = \overline{(DE_{v})_{i}} * N * d \\ \varphi_{p_{i}} = \overline{(DE_{p})_{i}} * N * d \\ \psi_{ref} = A \left(DE_{ref} * N * d \right)^{n} \end{cases}$$
(4.12)

Due to the different permeability of the cortical envelope, the fluid flow and fluid pore pressure will dominate on the endocortical and periosteal surfaces, respectively. Therefore, the value of parameters, i.e., A, c, n, and ψ_{ref} are estimated by minimizing the error squared between the predicted mineral apposition rate (MAR_i) and the corresponding experimental value $(rp. MAR_i)$ of the periosteal and endocortical surfaces using Eq. (4.13).

$$F(A, c, n, \psi_{ref}) = \sum_{i=1}^{720} (r. MAR_i - MAR_i)^2$$
 (4.13)

4.3 Results

The model depicts osteogenesis as a function of pore pressure alone and pore pressure with fluid flow at cortical surfaces. The computed strain distribution (Fig. 4.2a) closely matches the experimental data with fluid velocity peaking at the endocortical surface (Fig. 4.2b). In contrast, pressure is zero at the endocortical surface and reaches the maximum at the periosteal surface (Fig. 4.2c). Figure 4.3 shows the plot of dissipation energy density due to fluid flow and pore pressure along the cortical thickness (shown by line a-a' in Fig. 3.4 of chapter 3) of

the beam mid-cross section. The dissipation energy density due to fluid flow and pore pressure aligns with corresponding fluid velocity and pore pressure across the cortical thickness.

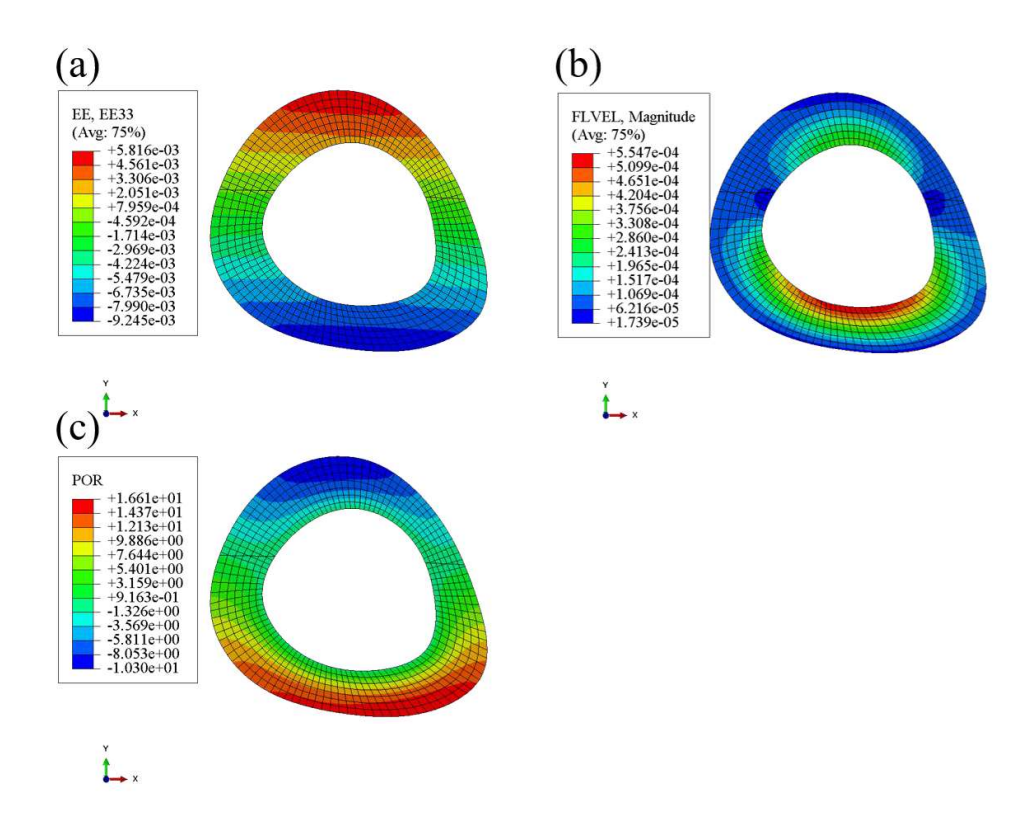


Figure 4.2 (a) Longitudinal strain distribution adapted from Berman et al. (95), (b) velocity distribution (mm/sec), and (c) pressure distribution (MPa) on the bone cross-section.

4.3.1 Osteogenesis as a Function of Pore Pressure

The osteogenic potential of pore pressure alone has been investigated here. The value of parameters that fit the MAR data on the periosteal surface comes out to be as follows: $Ac^n = 2.06$, n = 0.52, and $\psi_{ref} = 0.08 \,\mu\text{m}^3/\mu\text{m}^2/\text{day}$. c cannot be computed separately; hence, Ac^n is determined. The value of DE_{ref} is $3.56 \times 10^{-6} \,\text{N}\mu\text{m}/\mu\text{m}^3$. Pore pressure as a stimulus in the model predicts the new bone formation at the periosteal surface (Fig. 4.4b). However, it fails to model osteogenesis completely at the endocortical surface. The BFR/BS estimated at the periosteal and endocortical surface is $0.99 \,\mu\text{m}^3/\mu\text{m}^2/\text{day}$ (p-value = 0.71, t-test) and 0.22

 μ m³/ μ m²/day (p-value = 0.03, t-test). The corresponding experimental values are 0.93 ± 0.16 μ m³/ μ m²/day and 0.59 ± 0.14 μ m³/ μ m²/day. As shown in Fig. 4.4b, site-specific distribution at the periosteal surface is not significantly different from the experimental distribution (p-value = 0.89, Watson's U² test). However, the new bone distribution at the endocortical surface does not come close to the in vivo bone distribution (p-value = 0.04, Watson's U² test).

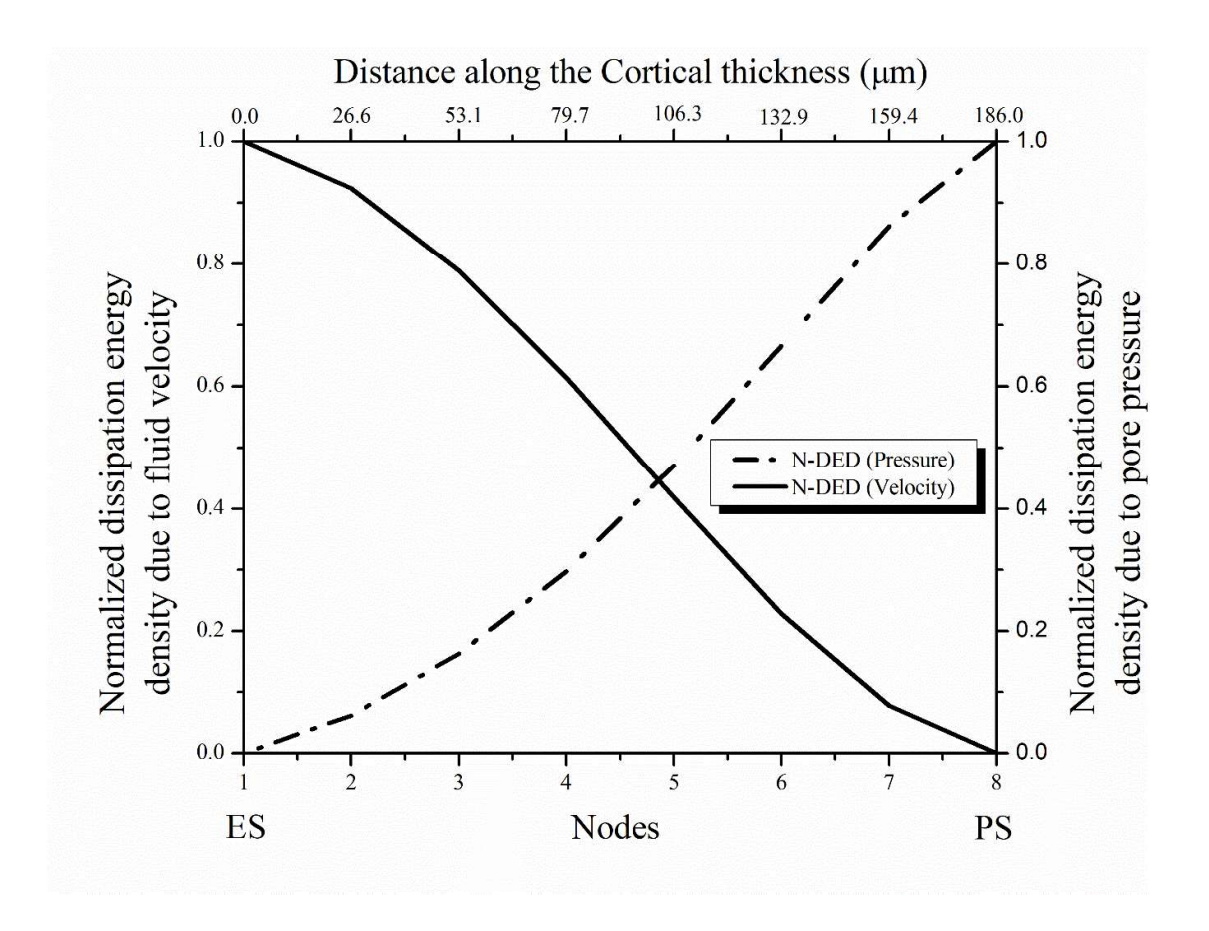


Figure 4.3 Normalised dissipation energy density (DED) due to fluid velocity and pore pressure along the radial line a-a' on the anterior side of the mid-cross section of the beam (see Fig. 3.4 of Chapter 3), progressing from the endocortical surface (ES - Node 1) to the periosteal surface (PS - Node 8).

4.3.2 Osteogenesis as a Function of Pore Pressure and Fluid Flow

The values of the parameters A, c, n, and ψ_{ref} which fit the new bone thickness and dissipation energy density due to both fluid flow and pore pressure are as follows: $A = 503.94 \,\mu\text{m}/\sqrt{\text{N}/\text{day}}$, $c = 1.85 \times 10^{-5}$, n = 0.49, and $\psi_{ref} = 0.25 \,\mu\text{m}^3/\mu\text{m}^2/\text{day}$. DE_{ref} is estimated to be $4.61 \times 10^{-10} \,\text{N}\mu\text{m}/\mu\text{m}^3$.

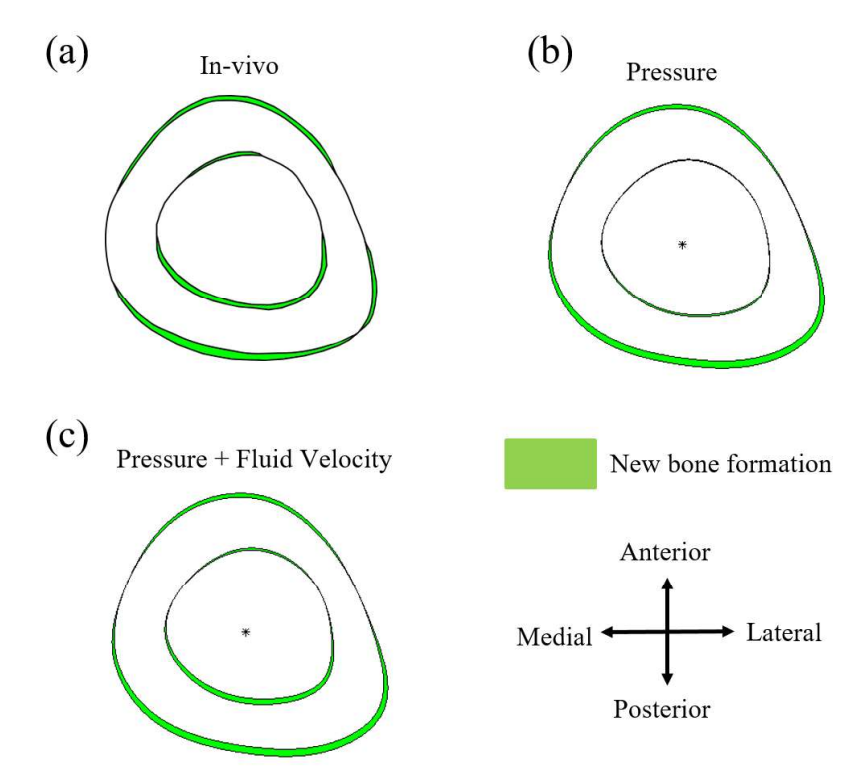


Figure 4.4 (a) In vivo, new bone formation at the cortical surfaces for mid-strain loading protocol (adapted from Berman et al. (95)), and the corresponding numerically predicted new bone distribution as a function of (b) pore pressure only, and (c) pore pressure with fluid flow.

The osteogenesis results at the cortical surface improve when fluid flow and fluid pressure are considered together (Fig. 4.4c). The computed BFR/BS of 0.97 $\mu m^3/\mu m^2/day$ and 0.63 $\mu m^3/\mu m^2/day$ at the periosteal and endocortical surfaces are not significantly different from the experimental BFR of 0.93 \pm 0.16 $\mu m^3/\mu m^2/day$ (p-value = 0.78, t-test) and 0.59 \pm 0.14

 μ m³/ μ m²/day (*p*-value = 0.83, t-test) at the corresponding surfaces. The distribution of the newly formed bone in the experimental study and that predicted by the mathematical model at both surfaces are also not significantly different (*p*-value = 0.95 at the periosteal surface, and *p*-value = 0.71 at the endocortical surface, Watson's U² test) (Fig. 4.4c).

4.4 Simplified Model

In contemporary mathematical models, bone adaptation is commonly presumed to be proportional to either strain energy density or dissipation energy density (100)(75)(82). However, this foundational assumption may be inappropriate, as in vivo research has revealed that bone adaptation evinces a linear dose-response association with strain (56). This implies that bone adaptation may be more appropriately modeled as being proportional to the square root of dissipation energy density (137). This is supported by the derivation of MAR in Chapter 2, where MAR is shown to vary with the square root of dissipation energy density. In the FEA model with unconstrained n (see section 3.3.3), too, the value of exponent n comes out to be 0.497 and thus may act as another validation for MAR to be approximately proportional to the square root of dissipation energy density. Therefore, for the sake of simplicity and in accordance with the derived Eq. (2.16), we assumed the value of n to be 0.5 and tested the hypothesis, whether the site-specific mineral apposition rate at both periosteal and endocortical surface is directly proportional to the square root of dissipation energy density (above its reference value), i.e.,

$$MAR_{i} = A\sqrt{(\varphi_{v_{i}} + \varphi_{p_{i}})} - \psi_{ref}, where \begin{cases} \varphi_{v_{i}} = \overline{(DE_{v})_{i}} * N * d \\ \varphi_{p_{i}} = \overline{(DE_{p})_{i}} * N * d \\ \psi_{ref} = A\sqrt{DE_{ref} * N * d} \end{cases}$$
(4.14)

Similar to that in section 3.3.3, when n=0.5, the values of parameters, i.e., A and ψ_{ref} come out to be 509.33 μ m/ \sqrt{N} /day and 0.23 μ m³/ μ m²/sec, respectively. The value of DE_{ref} calculated to be 3.89x10⁻¹⁰ N- μ m/ μ m³. The BFR estimated at the periosteal surface by the

simplified model is $0.97~\mu m^3/\mu m^2/sec$, which is significantly similar to the BFR of $0.93\pm0.16~\mu m^3/\mu m^2/sec$ obtained experimentally (p-value = 0.81, t-test). According to the Watson U² test, the simplified model's estimation of new bone distribution at the periosteal surface, as depicted in Fig. 4.5b, is not significantly distinct from the actual new bone distribution in vivo, as shown in Fig. 4.5a (p-value = 0.95, Watson U²-test). Similarly, the BFR computed on the endocortical surface by the simplified model is $0.63~\mu m^3/\mu m^2/sec$ (Fig. 4.5b), which is not significantly different from the in vivo BFR of $0.59\pm0.14~\mu m^3/\mu m^2/sec$ (p-value = 0.82, t-test). The Watson U² test also shows that simulated bone distribution at the endocortical surface (Fig. 4.5b) is not significantly different from the in vivo new bone distribution, as shown in Fig. 4.5a (p-value = 0.67, Watson U²-test).

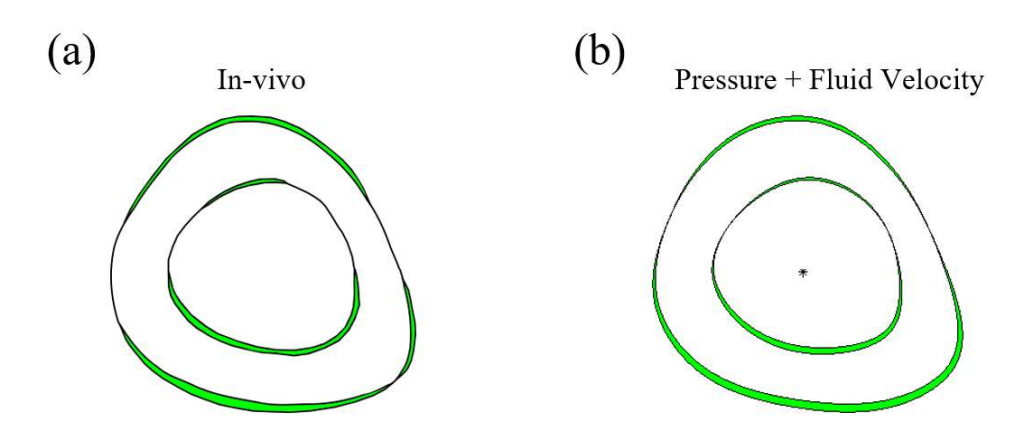


Figure 4.5 (a) The distribution of new bone in vivo at cortical surfaces for mid-strain loading protocol (adapted from Berman et al. (95)). (b) The corresponding computationally estimated new bone distribution using a simplified model is also illustrated.

4.4.1 Prediction Example

To verify the robustness of the model, we solved a high-strain loading example taken from Berman et al. (95). The difference is that instead of 2050 μE , 2400 μE is applied at the anteromedial site. The value of parameters A, n, c, and DE_{ref} remains the same as in section

3.4. The predicted BFR at the periosteal surface is $1.56 \, \mu m^3/\mu m^2/\text{sec}$, which is close to the experimental BFR of $1.67 \pm 0.15 \, \mu m^3/\mu m^2/\text{sec}$ (p-value = 0.49, t-test). Similarly, corresponding to the experimental BFR of $1.01 \pm 0.11 \, \mu m^3/\mu m^2/\text{sec}$ at the endocortical surface, the BFR measured from the model is $1.02 \, \mu m^3/\mu m^2/\text{sec}$, which is close to the experimental BFR (p-value = 0.96, t-test). The new bone distribution at both the cortical surfaces, i.e., MAR (Fig. 4.6b), is not significantly different from the experimental new bone formation at the middiaphysis (Fig. 4.6a) (p-value = 0.44 and p-value = 0.08 for periosteal and endosteal surfaces, Watson's U² test). However, the model underestimates the new bone distribution at the anterior side of the endocortical surface.

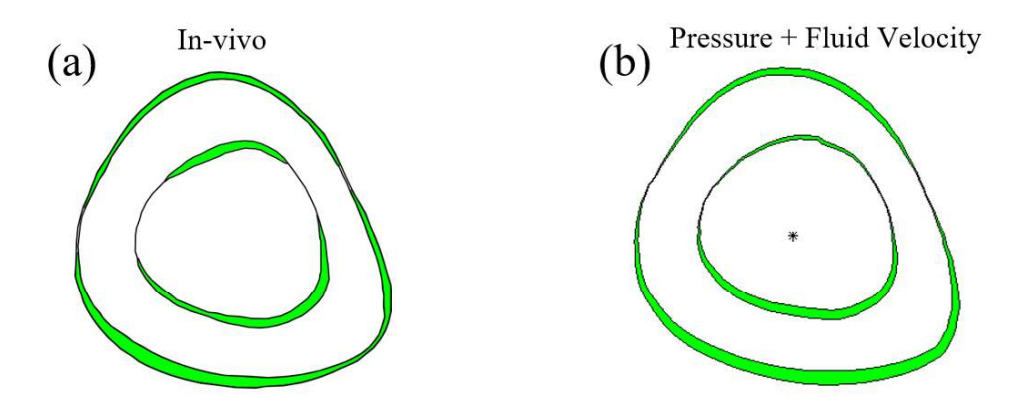


Figure 4.6 (a) In vivo new bone distribution at cortical envelops for high strain loading protocol (adapted from Berman et al. (95)) and (b) corresponding computationally estimated new bone distribution using the simplified model.

4.4.2 Sensitivity Analysis

In modeling studies, knowing how different factors affect the results is essential. In this study, we tuned the parameter A and ψ_{ref} of a mathematical model while considering the value of n = 0.5 to predict the new bone distribution. To understand the physical significance of parameters A and ψ_{ref} , the simplest form of sensitivity analysis is used. The analysis is called

local sensitivity analysis (LSA) or one-factor-at-a-time (138). In this sensitivity analysis, we vary one model parameter at a time by a given amount and examine the impact on the output results. Figure 4.7a illustrates that increasing the remodeling rate (A) (while keeping the other parameters constant) leads to a linear increase in the bone formation rate (BFR). Thus, we identify A as a parameter that amplifies the response of osteocytes. This is in accordance with the study done by Kumar et al., who found that A quantifies how much an osteocyte responds to loading (100). As far as the dependence of A on loading parameters is concerned, Eq. (2.17) shows that A is a proportionality constant that does not depend on any loading parameters. On the other hand, Fig. 4.7b demonstrates the impact of changing the parameter ψ_{ref} on the bone adaptation, while A remains constant. Interestingly, increasing the value of ψ_{ref} decreases the BFR linearly. ψ_{ref} may be identified as a threshold sensitivity of the osteocytes, which depends on the number of loading cycles and days of loading. ψ_{ref} increases as the number of loading cycles increases (see Fig. 4.7c), however, following the law of diminishing returns (54). This threshold sensitivity indicates that the osteocytes lose their sensitivity as the number of loading cycles increases. Other loading parameters, such as loading magnitude and frequency, do not change these tuning parameters as they directly influence the dissipation energy density per cycle.

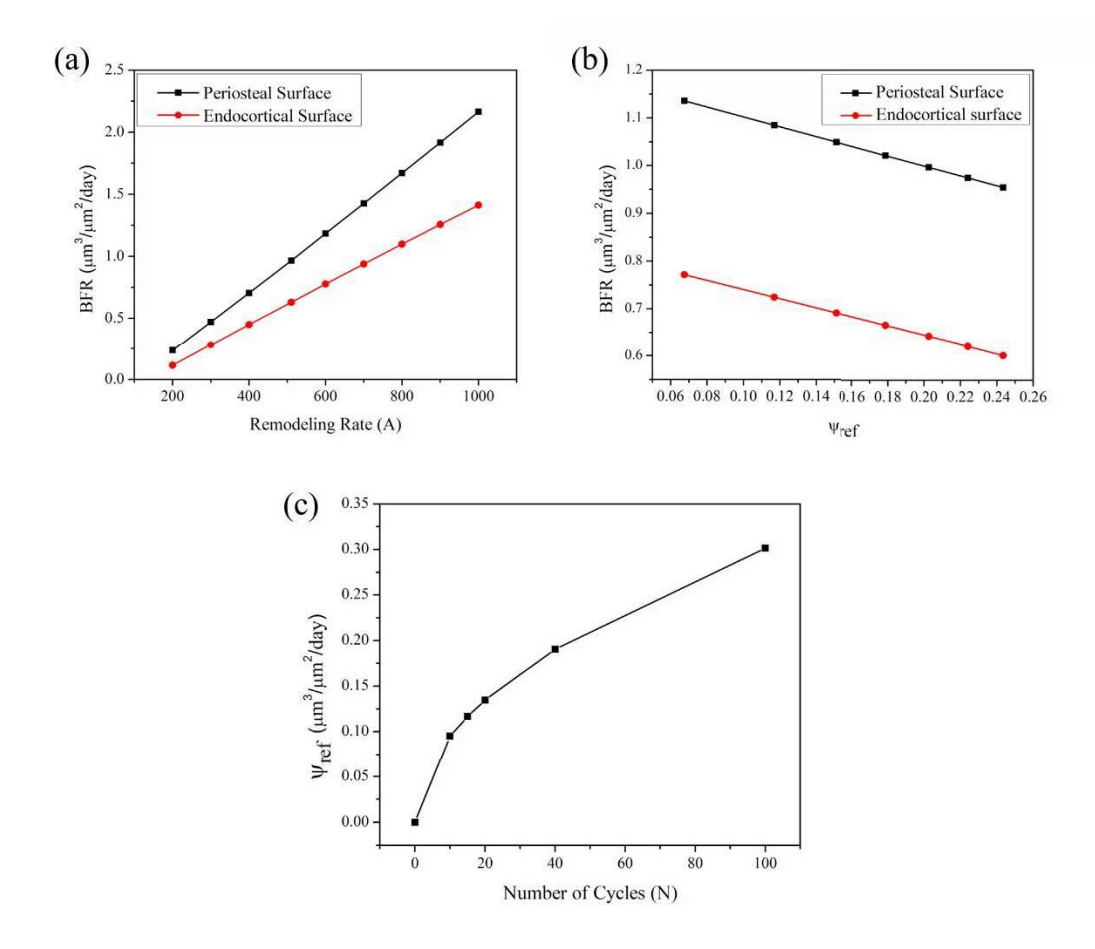


Figure 4.7 Plots showing BFR as a function of (a) remodeling rate A and (b) threshold/reference parameter ψ_{ref} , which in turn is also shown in (c) as a function of the number of loading cycles N.

4.5 Discussion

We utilize finite element analysis to determine the structural changes in the tibia middiaphyseal cross-section under the action of mechanical loading, and a novel mathematical formulation derived in the previous chapter is used to estimate the new bone formation at the cortical surfaces. The developed mathematical model exhibits that the combination of fluid flow with fluid pore pressure may be responsible for (re)modeling responses, i.e., MAR on both the periosteal and endocortical surfaces. A study by Tiwari et al. also confirms that two or more stimuli may be required to accurately predict osteogenesis at the cortical surfaces (82). It is in contrast to the studies that consider a single stimulus, such as strain, fluid velocity, etc., that find success only in predicting bone formation at the periosteal surface (100)(76)(78). Unlike previous mathematical models that measure the average bone formation rate at a cross-section (139)(106), our site-specific model provides a spatial distribution of new bone formed at both cortical surfaces, which gives our model an edge over the previous models.

In this work, we considered dissipation energy density due to both fluid flow and pore pressure as a stimulus, as numerous studies suggest that they play a prominent role in bone adaptation (88)(76)(124)(79)(63). The dissipation energy is the work done by the pore pressure or by the shear forces due to fluid flow, experienced by the osteocytes' membranes. The mathematical model results show that fluid flow alone as a stimulus predicts osteogenesis at the endocortical surface, whereas it underestimates the site-specific bone formation at the periosteal surface. The converse results were found when considering pore pressure alone as a stimulus, as it predicted bone formation at the periosteal surface and underestimated it at the endocortical surface. This was because of the drained and undrained conditions, respectively, of the endocortical and periosteal surfaces resulting in high fluid flow (or zero pressure) and negligible fluid flow (or high pressure), respectively, at the two surfaces (Fig. 4.2b, c) (112)(124). This follows the existing literature. For example, the work by Carriero et al. shows that the fluid flow correctly predicts the new bone distribution at the endocortical surface only (77). On the other hand, Gardiner et al. (86) and Scheiner et al. (124) show that the pore pressure also has the potential to act as an osteogenic stimulus. Accordingly, it may be assumed that fluid flow controls the new bone formation at the endocortical surface, whereas pore pressure controls the bone distribution at the periosteal surface.

This model tries to integrate most of the previously developed models. Cater et al. suggested a power relationship between bone adaptation and stress history, where the power exponent was an unknown value to be estimated by the quantitative analysis of in vivo studies (140). Our

model establishes a power law relationship between bone formation and stimulus with a power exponent of 0.5. The total dissipation energy density (φ) is the function of the number of loading cycles (N) and the number of loading days (d). The more cycles and days of loading, the more will be the value of φ , which means more new bone formation; however, the osteogenic potential of the current cycle will be less than the previous cycle because of the power exponent n. This is in accordance with the experimental and numerical literature that shows bone response saturates with the increase in the number of cycles (78)(56)(52)(57). Similarly, the osteogenic potential of the current day's loading will also be lower than the previous due to the exponent n, resulting in the saturation of MAR. This saturation of MAR with an increase in the number of loading cycles or days might be due to the increases in the area of bone, which leads to a reduction in stimulus (dissipation energy density) (100). The previously developed poroelasticity-based models did not capture this aspect of bone adaptation as they have considered the bone adaptation to be linearly related to a stimulus (for example, fluid velocity, dissipation energy density) (83)(76). Note that similar to the stimulus (φ) , the threshold/reference ψ_{ref} is also a function of the number of cycles (N) and the number of loading days (d). In a way, it means that the threshold value of MAR also increases as osteocytes become "deaf" to repeated mechanical loading.

The developed model has the following limitations: (i) Bone formation and its spatial distribution are only tested on the midsection of the tibia. However, the model's accuracy can be pushed to predict the new bone formation at different cross-sections along the tibial length. (ii) We have not yet examined the model for different number of loading days. However, it is worth noting that the exponent for d in the model (i.e., n = 0.5) is approximately similar to the exponent of d (i.e., $\beta = 0.465$) in the model developed by Prasad and Goyal (78), which they have validated for a range loading protocols with varying duration. Nevertheless, validation of the present model for a shorter experiment has been taken as a future work. (iii) The developed

model is also not tested for mice of different ages. (iv) The model does not account for the erosion or resorption process during loading, which is generally detected near the neutral axis on the endocortical surface rather than the periosteal surface (105). (v) The developed model does not predict woven bone formation as the mechanism differs from the lamellar bone formation (141)(142)(143). (vi) Sensitivity analysis has not been carried out for material parameters, LCN permeability, loading magnitude, etc. (vii) The newly developed model made some simplifications concerning the structure, properties, and biology of the bone, which are as follows.

Structure – Bones have porosities at different lengths, such as lacune canalicular and vascular porosity (107), affecting bone formation rate. These vascular channels act as a local sink and show their shielding effect by reducing the fluid flow in its surrounding region (144)(79). However, for simplification, we only considered the lacune canalicular porosities only. Moreover, we considered LCN porosity to be unrealistically regular, which, in reality, is spatially heterogeneous (145)(146). The LCN architecture influences the fluid flow pattern and, consequently, its effect on osteocytes (79). Incorporation of multiscale porosities may improve results.

Properties – The bone, for simplicity, has been considered a linear, isotropic, homogenous poroelastic material. However, the bone, in general, is anisotropic (147), which may affect the fluid flow in LCN (148).

Biological Factors – This newly developed tissue-level model focuses on the tissue-level response of bone adaptation and ignores the molecular and cellular elements, such as the role of integrins (66) and glycocalyx (135). Moreover, biochemical molecules such as parathyroid hormone (PTH), insulin-like growth factors (IGFs), IP, etc., believed to be involved in transmitting signals from osteocytes to osteoprogenitor cells, have not been incorporated in this model to reduce the complexity (149).

As such, spatial new bone distribution along the tibial length, testing of a model for mice of different ages, addressing erosion and woven bone formation at one or both the periosteal and endocortical surfaces, detailed sensitivity analysis, improved structure and property of bone, incorporation of more biological factors, etc. have been taken as the future work.

4.6 Conclusion

To the authors' best knowledge, a poroelasticity-based mathematical model presented here is the first of its kind to predict the site-specific lamellar bone distribution (MAR) simultaneously at both cortical surfaces (periosteal and endocortical). It shows that the site-specific mineral apposition rate is directly proportional to the square root of dissipation energy density due to both fluid flow and pore pressure minus its reference value. Analytical derivation of this relationship is also novel, and to the authors' best knowledge, such derivation is being reported for the first time. The key finding of this model is that the bone formation rate at the periosteal and endocortical surface is primarily controlled by pore pressure and fluid flow, respectively. This novel model can be improved by integrating woven bone formation at higher loads and resorption at the endocortical surface. The model can be further enhanced by considering the effect of age.

Chapter 5 – Overall Bone Adaptation Model

Declaration: Some of the contents of this chapter are published in ASME IMECE Conference

Proceedings under the title 'Investigating the Difference in Cortical Bone Adaptation at

Endocortical and Periosteal Surfaces by Fluid Flow Analysis.'

https://doi.org/10.1115/IMECE2021-71220

Abstract

Bone formation rate is crucial for assessing osteogenesis due to mechanical loading, offering insight into bone (re) modeling process and health conditions like osteoporosis. The existing model cannot predict BFR at both cortical surfaces. This study aims to fill this gap by developing a mathematical model predicting BFR at both cortical surfaces, incorporating fluid flow and pore pressure as stimuli. We present a finite element analysis based on experimental data, simulating cantilever loading effects at mid-diaphysis of a C57BL6 mouse tibia. Dissipation energy density due to fluid flow and pore pressure is computed, and a novel mathematical formulation is used to estimate the bone formation rate. The model predicts the average bone formation rate (BFR) at the periosteal and endocortical surfaces. The experimental validation and comparison show good agreement, indicating the model's efficacy. As desired, the model can differentiate between a continuous cyclic loading and a rest-inserted cyclic loading. The model establishes that bone formation at the two surfaces, viz. endocortical and periosteal, may result from the combined dissipation energy density due to fluid flow and pore pressure.

Keywords: Bone Formation Rate (BFR), Periosteal Bone Surface, Endocortical Bone Surface, Theory of Poroelasticity, and Dissipation Energy Density.

5.1 Introduction

Bone formation rate (BFR) is the most fundamental term to measure osteogenesis due to mechanical loading (90). It represents the speed at which new bone tissue is deposited and

provides valuable insight into (re)modeling processes in bone. Monitoring BFR can help diagnose and manage bone health-related issues such as osteoporosis. Guided by BFR assessments, approaches, including physical exercise and pharmacological intervention, can be tailored to enhance the BFR. The bone adaptation model developed in Chapter 4 has its advantages as it predicts the site-specific new bone formation and can be used to measure BFR indirectly from the MAR measured by the model. However, it is going to be a tedious task. Therefore, a model that directly predicts the average bone formation rate might be significantly helpful. While there are few mathematical models to predict the average BFR at the periosteal surface, no existing mathematical models can predict the bone formation rate at both cortical surfaces.

The previous chapter highlights that load-induced fluid flow and pore pressure are required to predict site-specific osteogenesis at both cortical surfaces. Hence, based on these findings, this chapter aims to develop a new mathematical model that can directly predict the BFR by considering fluid flow and pore pressure in conjugation as stimuli. Accordingly, we conducted the finite element analysis, which simulated the experimental data of Srinivasan et al. (99). We utilized the theory of poroelasticity to estimate the fluid velocity, pore pressure, and the corresponding dissipation energy density. These models were coupled to the novel mathematical formulation, predicting the average bone formation rate at the periosteal and endosteal surfaces.

The chapter is organized as follows. Section 5.2 briefly describes the methods for computing the overall bone formation rate at the periosteal and endosteal surfaces of the tibial bone of female C57BL6 mice. Section 5.3 presents the result and discussion. A conclusion is drawn in section 5.4.

5.2 Materials and Methods

5.2.1 Finite Element Model

As shown in Fig. 5.1, we used a tabular beam of 5 mm in length with a cross-section similar to the 16-week-old mice's tibial mid-diaphyseal cross-section located at 1.8mm proximal to the tibia fibula junction, which was adapted from Srinivasan et al. (99). We solved the problem using the finite element method and the commercial software ABAQUS. The periosteal surface of the bone is impermeable, and the endosteal surface is permeable (115)(116). Therefore, to simulate these conditions, we apply zero pressure boundary condition (p = 0) on the inner surface and zero velocity boundary condition, i.e., zero flow boundary condition (∇p . r = 0) on the outer surface, where r is a vector in the radial direction. After conducting the convergence study, as shown in Fig. 5.2, the beam was meshed with 96400 C3D8RP (Continuous 3 Dimensional 8-noded Reduced-integration Pore-pressure hexahedral) elements, and a coupled pore fluid diffusion and stress analysis are performed in ABAQUS. For the sake of simplicity, the material properties are considered to be the same as those used in previous chapters as laid out in Table 3.1 in Chapter 3.

5.2.2 Dissipation Energy Density

For this poroelastic model, dissipation energy density due to fluid flow and pore pressure after considering the zone of influence is computed similarly to Section 4.2.2 of Chapter 4. Accordingly, the updated stimulus (dissipation energy density, $\overline{(DE_v)}_i$, and $\overline{(DE_p)}_i$) at the surface node is defined as follows:

$$\overline{(DE_v)_i} = \frac{\int DE_v w(x) dV}{\int w(x) dV} = \frac{\sum_{j=1}^n (DE_v)_j (w(x))_j}{\sum_{j=1}^n (w(x))_j}$$
(5.1)

$$\overline{(DE_p)}_i = \frac{\int DE_p w(x) dV}{\int w(x) dV} = \frac{\sum_{j=1}^n (DE_p)_j (w(x))_j}{\sum_{j=1}^n (w(x))_j}$$
(5.2)

where $w(x) = e^{\left(\frac{-5|x|}{d}\right)}$ a weightage function, d is the average thickness of the bone at mid-diaphysis cross-section, and x is the distance from a node at the surface to the osteocyte in the zone of influence.

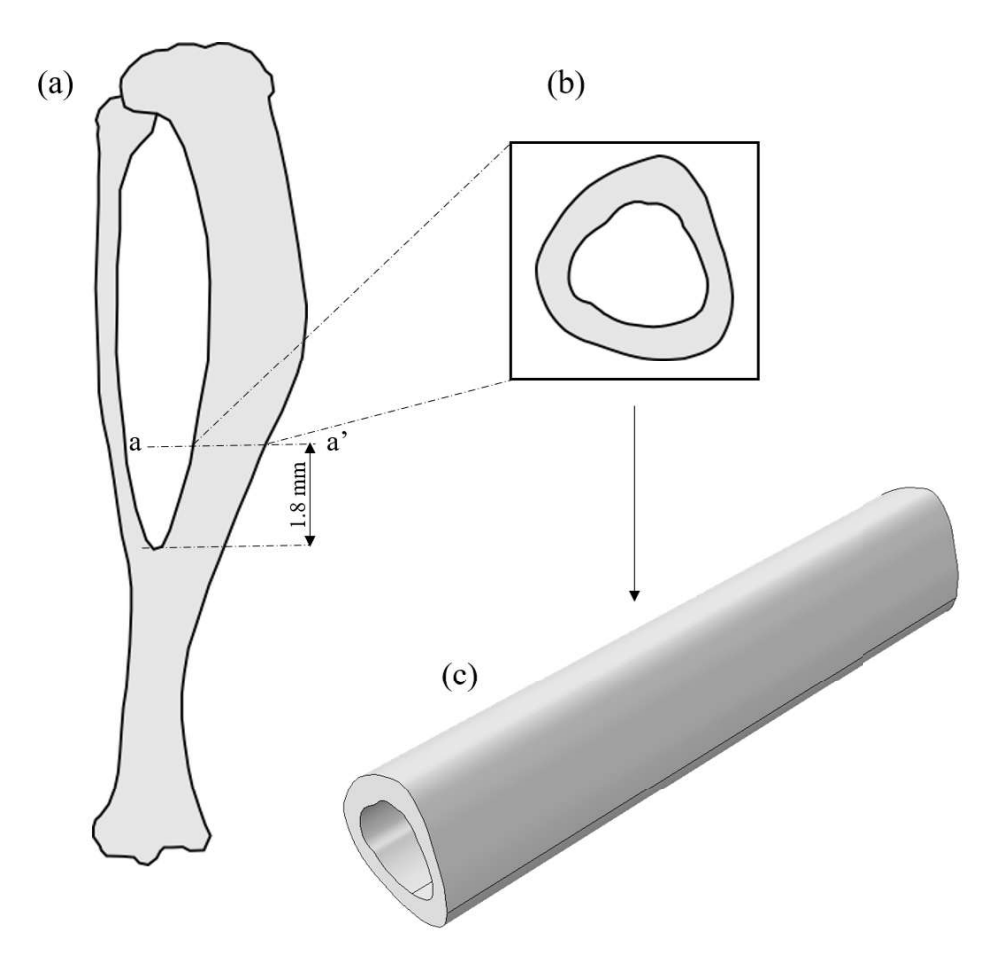


Figure 5.1 Pictorial representation of (a) C57BL/6 mouse tibia with (b) an idealized cross section at section a-a' (adapted from Srinivasan et al. (99)). (c) A simplified beam developed with a cross-section similar to the section at a-a'.

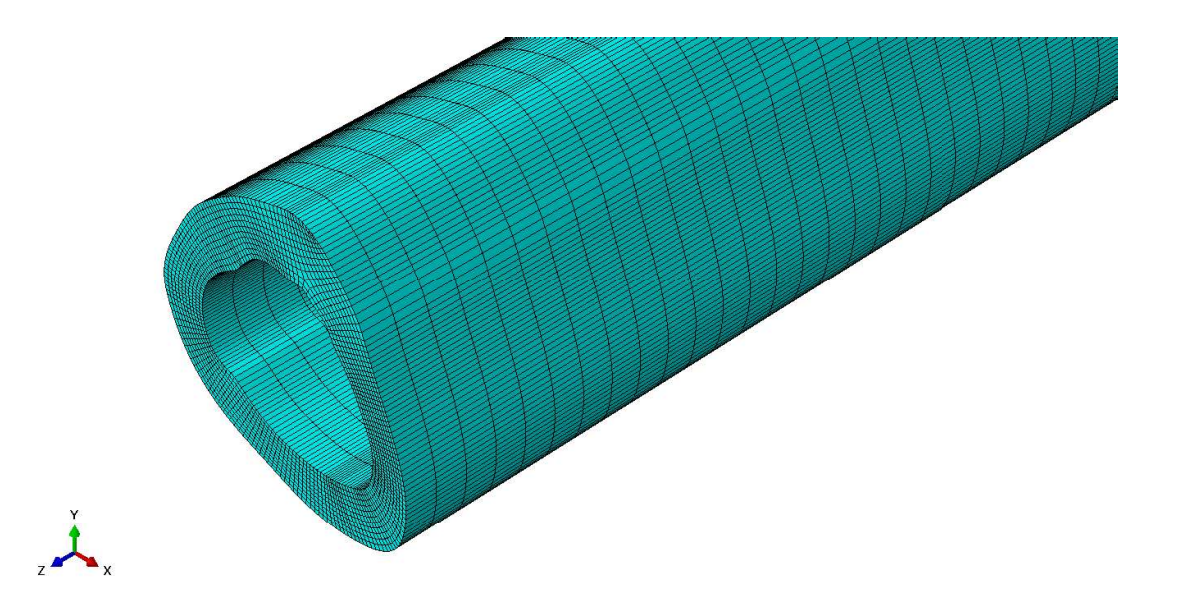


Figure 5.2 The finite element meshed beam has a cross-section similar to the midsection of the mouse tibia.

5.2.3 Estimation of Bone Formation Rate

We hypothesize that the bone formation rate (BFR) for the section in consideration may be given by:

$$BFR = A \sqrt{\sum_{i=1}^{m} (\varphi_v)_i + \left(C * \sum_{i=1}^{m} (\varphi_p)_i\right)} + \psi_{ref}$$
 (5.4)

where $(\varphi_v)_i = \overline{(DE_v)_i} * N * d$ and $(\varphi_p)_i = \overline{(DE_p)_i} * N * d$ is the total dissipation energy density due to fluid flow and pore pressure at a given node. N and d are the number of cycles applied per day and the number of days loading is applied, respectively. m is the number of nodes at the cortical surface in consideration. A, C, and ψ_{ref} are the parameters to be determined. This mathematical equation presented can fit the periosteal BFR data obtained from the experiment conducted by Srinivasan et al. (see Table 5.1) (99). This study involves 70 C57BL/6 mice (16-week-old females) divided into seven groups. All mice underwent a loading for three days a week for three-week loading protocols. The first six loading groups experienced either 50

cycles/day (with a 1 Hz trapezoidal waveform) of cyclic loading or 50 cycles/day with rest intervals of 10 seconds at three different strain magnitudes that engendered the following three strain magnitude: 1000, 1250, and 1600 μ E (see Fig. 5.3). The remaining four loading group received either cyclic or rest inserted loading (depicted in Fig. 5.3) to induce a peak periosteal longitudinal strain of 1250 μ E. The mice in these groups were also subjected to 10 or 250 load cycles daily. BFR for each loading protocol, which may be calculated by

$$BFR_{l} = \left(A \sqrt{\sum_{i=1}^{m} (\varphi_{v})_{i} + \left(C * \sum_{i=1}^{m} (\varphi_{p})_{i}\right)}\right)_{l} + \psi_{ref}$$

$$(5.5)$$

where l stands for loading protocol. The parameters A, C, and ψ_{ref} are calculated by minimizing the following squared error:

$$F(A, C, \psi_{ref}) = \sum_{l=1}^{10} (BFR_l - BFR_{el})^2$$
 (5.6)

where BFR_{el} represents the experimental bone formation rate for different loading protocols reported by Srinivasan et al. (99). Curve fitting is done using the Levenberg-Marquardt algorithm using Matlab. To simulate the loading protocols mentioned above, we set displacements to zero at one end of the beam, and the nodes at the other end are subjected to trapezoidal mechanical loading.

To validate the endosteal apposition determined by our mathematical model, we utilized in vivo BFR data at the endocortical surface for the same loading protocols from another experimental study conducted by Srinivasan et al. (150), as shown in Table 5.2.

The Student's t-test (a one-sample, two-tailed t-test) has been utilized to compare the bone formation rate predicted by the mathematical model against the experimental bone formation rate.

Table 5.1 Loading protocols adapted from Srinivasan et al. (99).

Protocols	Loading Regimen			Induced	rp. BFR
	Strain (µE)	Cycles/d	Rest (s)	Strain (με)	(μm ³ /μm ² /d)
1	1000	50	0	1022 + 40	0.029 + 0.011
2	1250	50	0	1226 + 26	0.100 + 0.032
3	1600	50	0	1567 + 49	0.215 + 0.059
4	1000	50	10	1003 + 37	0.085 + 0.032
5	1250	50	10	1275 + 40	0.168 + 0.050
6	1600	50	10	1640 + 48	0.377 + 0.084
7	1250	10	0	1268 + 49	0.042 + 0.026
8	1250	250	0	1249 + 48	0.154 + 0.054
9	1250	10	10	1266 + 38	0.133 + 0.038
10	1250	250	10	1249 + 40	0.414 + 0.067

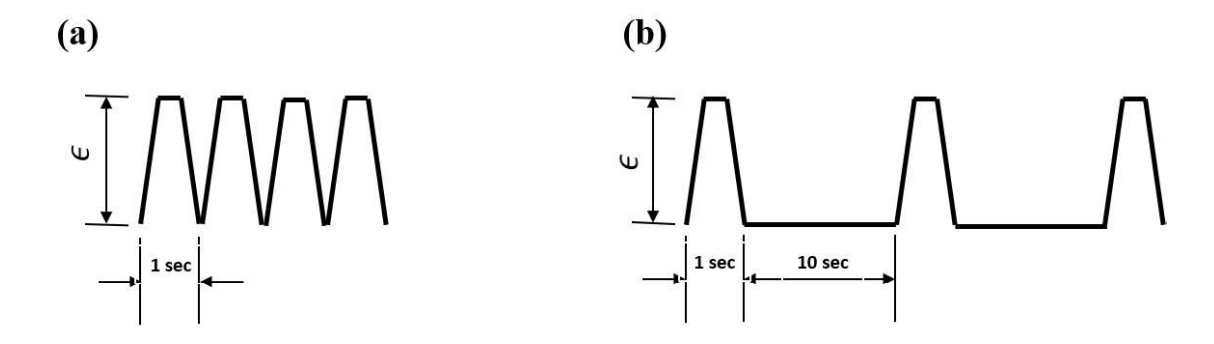


Figure 5.3 Trapezoidal loading waveform (a) with rest and (b) without rest insertion.

Table 5.2 Loading protocols adapted from Srinivasan et al. (150).

Protocols	re. BFR (μm³/μm²/d)
1	0.03 ± 0.03
2	0.04 ± 0.1
3	0.04 ± 0.18
4	0.05 ± 0.11
5	0.06 ± 0.32
6	0.15 ± 0.31
7	0.0 ± 0.05
8	0.09 ± 0.04
9	0.07 ± 0.09
10	0.3 ± 0.21

5.3 Results and Discussion

Mechanical loading of the tibia resulted in a pressure gradient, resulting in a three-dimensional flow in the lacunar-canalicular porosity. Figure 5.4 shows the vector representation of the fluid flow pattern at the mid-section of bone for loading protocol 1. During the loading, the medial surface is in compression, and the lateral surface of the bone is in tension, which results in a fluid flow in the mediolateral direction.

Figure 5.5 shows the time evolution of fluid velocity in the tibia along the radial direction under loading protocols 1 and 4. Protocol 1 applies cyclic trapezoidal loading, whereas Protocol 4 applies rest-inserted cyclic trapezoidal loading. Figure 5.5a shows the initial transient for nearly 1 sec, then follows the same profile at the same frequency as the applied load for cyclic trapezoidal loading. The presence of glycocalyx coating in the lacunar-canalicular porosity

resulted in a viscous flow of fluid (151). This suggests that repetitive cyclic loading did not provide sufficient time to recover from the damping effect of viscous flow, which resulted in an initial transient during cyclic trapezoidal loading (152). Rest-inserted loading offers enough time to recover from the damping effect of viscous flow after every cycle, and it does not show any transient state (Fig. 5.5b). Hence, considering bone to be poroelastic not only predicts the effect of loading frequency on bone adaptation, as Kumar et al. [84] show but also differentiates between continuous and rest-inserted cyclic loadings

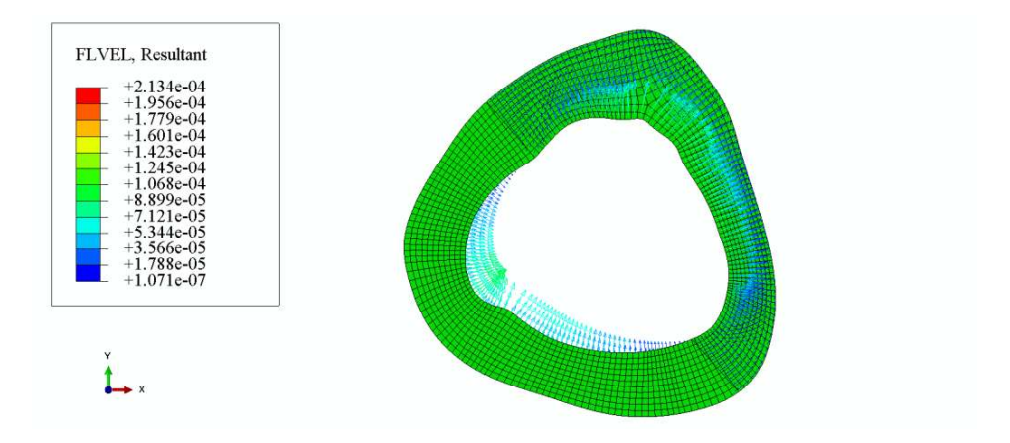


Figure 5.4 Three-dimensional fluid flow patterns when the tibia is under a loading inducing 1000 με at 1Hz frequency for the cantilever bending.

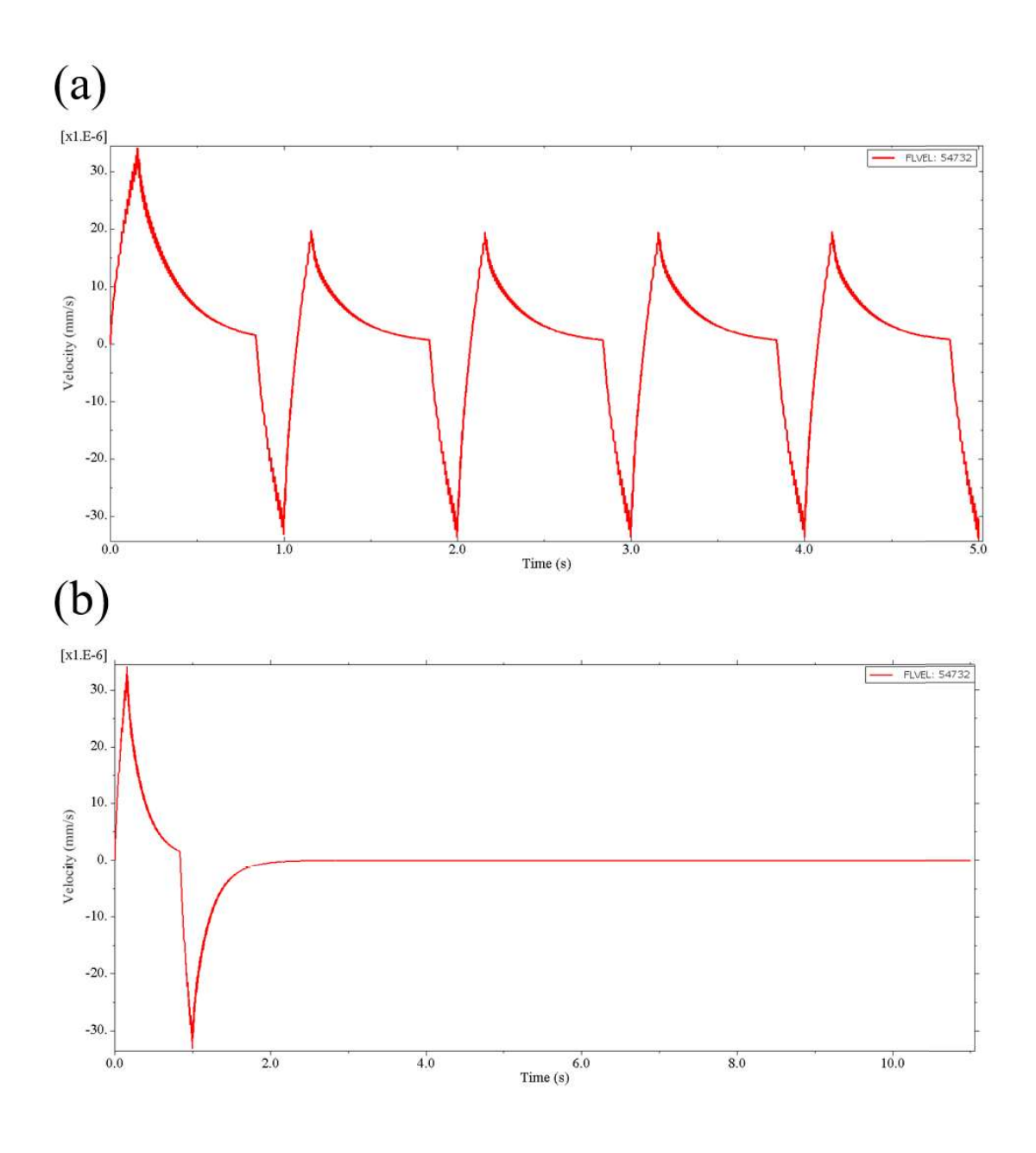


Figure 5.5 Variation of velocity with time at a node on endocortical surface for the trapezoidal cyclic loading (protocol 1) (a) and rest inserted trapezoidal cyclic loading (protocol 4) (b).

The dissipation energy density for one cycle due to fluid flow $(\overline{DE_v})_i$ and pore pressure $(\overline{DE_p})_i$ is computed at the node of interest as per Eq. (5.1) and (5.2) by extrapolating the results after the initial transient for cyclic trapezoidal loading (protocols 1, 2, 3, 7, and 8). For the rest-inserted loading, dissipation energy density is determined by extrapolating the first

cycle results (for protocols 4, 5, 6, 9, and 10). The parameters that fit the periosteal BFR data (Table 5.1) in Srinivasan et al. (99) at mid-diaphysis cross-section 1.8 mm proximal to the tibia-fibula junction are as follows:

$$A = 72.14$$
, $C = 3.50 \times 10^{-07}$, and $\psi_{ref} = -2.15 \times 10^{-04} \frac{\mu m^3}{\mu m^2/d}$.

The negative value of ψ_{ref} signifies that bone resorption occurs when there is no physical activity, i.e., no load-induced fluid flow. At the same time, A represents the bone formation rate when the load-induced dissipation energy density is unity. Figure 5.6 shows that the BFR predicted by the mathematical model for the periosteal surface is not significantly different from the experimentally measured BFR (average p-value > 0.4278 for the ten protocols). BFR predicted *in vivo* for the endocortical surface has been compared to the endocortical BFR predicted by our model, as shown in Fig. 5.7. The predicted endocortical BFR is not significantly different from the experimental endocortical BFR (average p-value = 0.6499). The model estimated the enhanced BFR for rest-inserted loading compared to cyclic loading and predicted the BFR at both the periosteal and endocortical surfaces in response to increased peak strain magnitude and cycle numbers.

We assumed the endosteal and periosteal surfaces are permeable and impermeable, respectively. This results in higher velocity at the endosteal surface relative to the periosteal surface (Fig. 5.8a). In contrast, pore pressure will be higher at the periosteal surface and lower at the endocortical surface (Fig. 5.8b). The dominance of fluid velocity on the endocortical surface and pore pressure on the periosteal surface leads to bone formation at the respective surface. This average bone formation model also confirms the hypothesis that fluid flow and pore pressure in conjugation are required to predict osteogenesis at both cortical surfaces. The developed model addresses the limitation of Prasad and Goyal's viscoelasticity-based average bone formation model, which only predicted the BFR at the periosteal surface (78).

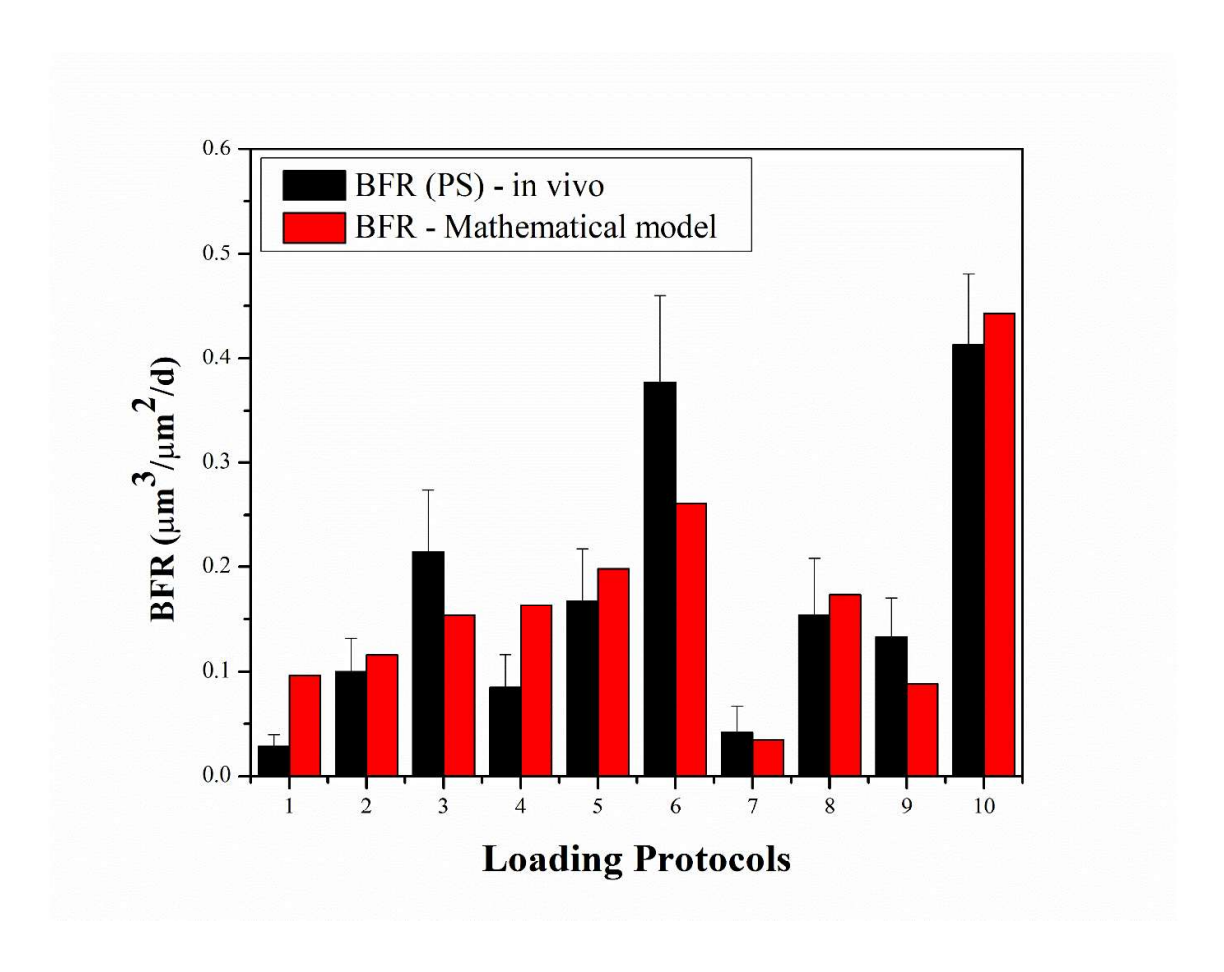


Figure 5.6 Comparison between the BFR – mathematical model and the BFR(PS) – in vivo for the periosteal surface. PS stands for the periosteal surface.

Although the developed model successfully predicts the BFR at the periosteal and the endosteal surfaces, our model has several limitations, as given below.

- 1) For simplicity, the bone matrix in this model is considered isotropic for mechanical properties. It is well known, however, that the bone matrix is anisotropic. Mechanical properties of cortical bone were reported to be transversely isotropic (147).
- 2) Small data regarding the permeability of endocortical and periosteal surfaces is available. In this model, we idealized the periosteal surface to be impermeable and the endocortical surface to be permeable. There will be an improvement in results if more data is available.

3) Cortical bone has porosities at different scales. However, we considered bone homogenous by considering the simple poroelastic model. The results may improve if the multi-scale porosity of bone is incorporated (153).

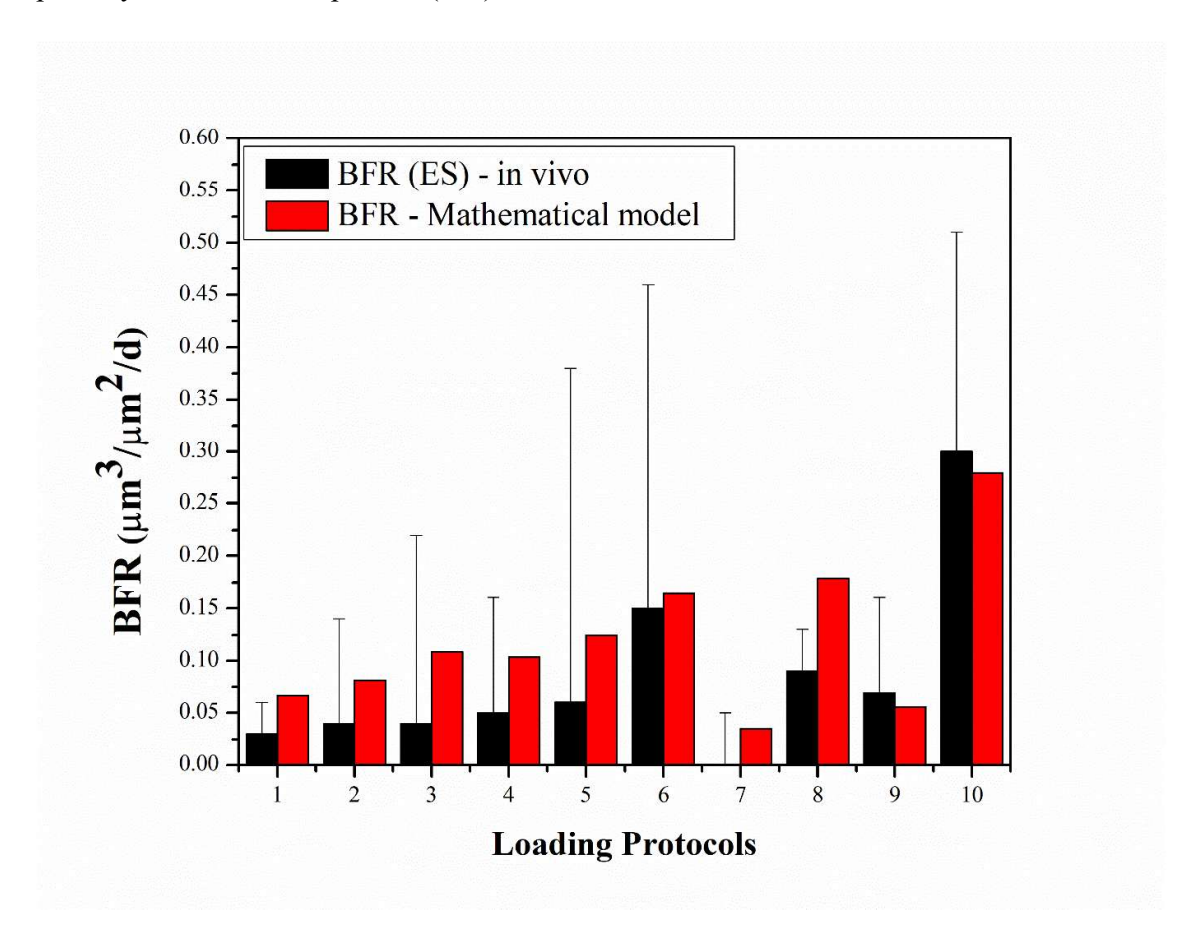


Figure 5.7 Comparison between the BFR – mathematical model and the BFR (ES) – In vivo at the endocortical surface. ES Stands for endocortical Surface.

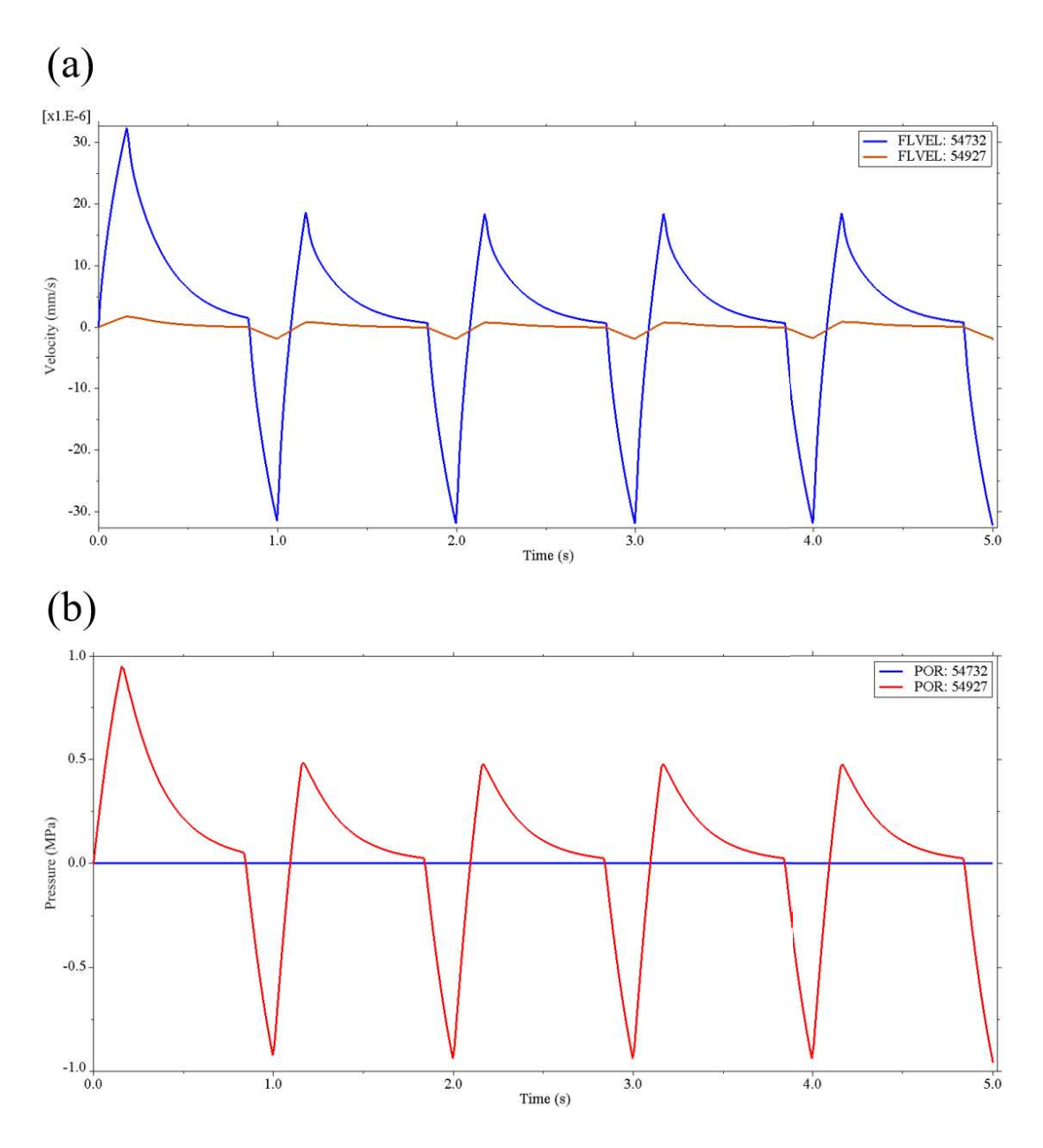


Figure 5.8 Illustration depicting (a) fluid velocity and (b) pore pressure at a node (54732) on the endocortical surface and node (54927) on the periosteal surface for protocol 1.

5.4 Conclusion

A computational model employing the theory of poroelasticity has been presented here to study load-induced bone adaptation. We have developed the dissipation energy-based mathematical model to differentiate between continuous cyclic and rest-inserted cyclic loadings. It also

reasonably accurately predicts the bone formation rate (BFR) at the endosteal and periosteal surfaces. This model suggests that load-induced fluid flow and pore pressure are essential in bone adaptation.

Chapter 6 – The Outcome of the Work

This concluding chapter delineates this thesis's specific contribution to bone adaptation. Furthermore, the chapter closes with future avenues of investigation enabled by the insights from this dissertation.

6.1 Introduction

Within the domain of bone adaptation, clinicians are diligently striving to identify the load-induced therapies (physical exercises) tailored for astronauts, SCI patients, and others to prevent bone loss (154)(1). However, despite considerable efforts, existing physical exercise regimens have proven insufficient to mitigate bone loss. For instance, prolonged standing sessions or walking with the mechanical orthosis in the case of chronic SCI patients have shown no significant effect on bone mineral density, keeping in mind that experiments were performed on patients with an injury duration of more than ten years (155)(156). Similarly, for astronauts, although ARED has partially mitigated the decline in bone mass, it has not entirely addressed the issue (154). Thus, there is a pressing need to reassess our approach toward understanding how mechanical signals regulate the bone adaptation process to elicit the desired new bone response, which forms the central focus of this thesis.

Most existing fluid flow-based in silico models for bone adaptation either predict osteogenesis at the periosteal surface or fall short in capturing dynamics at both cortical surfaces. Hence, the primary objective of this thesis is to develop a comprehensive mathematical model that can predict the new bone formation at both surfaces. Also, the model should take care of all the factors that affect the bone adaptation, such as magnitude of loading, frequency of loading, number of loading cycles and days, rest insertion, and shape of loading waveform. The research addresses the following anomalies related to existing in silico bone adaptation models:

1. Is fluid flow sufficient to predict osteogenesis at both cortical surfaces?

2. If not, what other physical stimuli should be considered to establish an in silico model capable of predicting new bone formation on both cortical surfaces?

The present study is a step ahead in understanding bone adaptation, which will aid researchers in developing new therapies for astronauts, SCI patients, and beyond.

6.2 Specific Contributions

This thesis presents a simple derivation of loading-induced site-specific new bone formation (viz. mineral apposition rate), which would be the first in the literature. The derivation demonstrated that the mineral apposition rate at both cortical surfaces is directly proportional to the square root of dissipation energy density above its reference value. While most existing models (if not all) can predict site-specific new bone formation at only one surface, the developed model surpasses this limitation by predicting new bone formation at both endocortical and periosteal surfaces. It was achieved by considering dissipation energy density due to pore pressure and fluid velocity as an osteogenic stimulus.

The overall thesis presents a plausible explanation for why tissue-level strain as a stimulus is rejected, whereas fluid flow and pore pressure are considered osteogenic stimuli. The theory also suggested that a single stimulus (fluid flow and pore pressure individually) may not adequately predict new bone formation at both cortical surfaces; instead, both should be incorporated into computer modeling of bone adaptation. Moreover, this study also highlighted that fluid flow controls the new bone formation at the endocortical surface, whereas pore pressure controls the new bone formation at the periosteal surface. Furthermore, the proposed law has been successfully tested against a different loading protocol.

Unlike previously existing models, the derived model undergoes validation with experimental data. The formulated model has three unknown parameters: remodeling rate (A), exponent of dissipation energy density (n), and threshold sensitivity (ψ_{ref}) . These parameters have been determined by minimizing a sum-square error function using the non-linear least square error

threshold sensitivity (ψ_{ref}) signifies the sensitivity of osteocytes, which further depends on the number of loading cycles and days. In addition, the exponent (n), which, according to the derivation, is 0.5, is validated using a finite element analysis (FEA) model based on in vivo study by Berman et al. (95). Based on these findings, an overall bone adaptation model has also been developed that directly measures the average bone formation rate, considering fluid flow and pore pressure as stimuli.

This thesis's findings may benefit the clinical and research field where bone health is the prime concern. This work also contributes to the research areas where the mathematical model development for bone adaptation has been attempted.

6.3 Future Scope

The findings from this work can be extended to the whole bone, providing a better understanding of whole-bone adaptation to mechanical loading. The model assumes a direct relationship between mechanical stimuli and site-specific bone adaptation. However, it is crucial to acknowledge that these mechanical signals reach the bone cells through a cascade of biochemical and cellular events. Therefore, incorporating these signal pathways via a multiscale modeling approach may provide a better understanding of bone adaptation.

We have operated under the assumption that bone is uniformly mechanosensitive. However, the sensitivity of the bone spatially varies with the distribution of mechanosensory cells, particularly osteocytes. This limitation will be addressed in the future by incorporating the osteocyte lacunae canalicular network architecture.

The *in-silico* model presented here assumes homogeneous lacunae canalicular porosity. However, it has been noticed that the lacunar canalicular network (LCN) is a complex heterogeneous network structure. Furthermore, the model overlooks the vascular porosity,

which may be a sink for fluid flow. Thus, incorporating both the vascular and heterogenous LCN porosity could enhance the model's ability to estimate the local response.

The currently developed model does not account for all the aspects of bone behavior. For instance, the model neither predicts woven bone formation at the higher mechanical loading nor anticipates inhibition in new bone formation due to static loading. In addition, the model does not look into the aspect of age-related bone loss. Hence, these works have been taken as future work.

Appendix A

Declaration: Some of the contents of this chapter are published in Bone Reports under the title 'Derivation, validation, and prediction of loading-induced mineral apposition rates at endocortical and periosteal bone surfaces based on fluid velocity and pore pressure.' https://doi.org/10.1016/j.bonr.2023.101729

1 Poroelastic-Viscoelastic Equivalence

Biological tissue such as bone is known to be composed of a porous solid matrix filled with fluid. The deformation of these tissues depends on the solid matrix and the fluid movement in and out of the pores. This tissue shows time-dependent behavior. In cases where time-dependent behavior cannot be neglected, we use either the viscoelasticity or poroelasticity theory to model these tissues. This section will show that whether we consider bone tissue viscoelastic or poroelastic material, it will offer similar time-dependent behavior.

1.2 Bone as a Viscoelastic Material

The theory of viscoelasticity can be used to interpret bone's mechanical behavior. It considers bone tissue a single phase and uses Kelvin-Voigt's models as its mechanical analog, where an elastic spring and a viscous dashpot are attached in parallel, as schematically shown in Fig. A1b. The governing equation for the deformation behavior of this model is as follows (92):

$$\sigma(t) = E\varepsilon(t) + \eta \dot{\varepsilon}(t) \tag{A1}$$

where E and η are Young's modulus and the viscosity of the material.

For a viscoelastic bar supporting a uniaxial stress $\sigma_z = -p_0$ as depicted in Fig. A1a, the strain is given as the following:

$$\varepsilon(t) = \frac{p_0}{E} \left(1 - e^{\frac{-Et}{\eta}} \right) \tag{A2}$$

where *t* is the time and $\frac{\eta}{E}$ is the time constant.

1.3 Bone as a Poroelastic Material

Poroelasticity presents a continuum framework for analyzing the deformation of porous fluid-filled material. Given that living bone shares the characteristics of fluid-filled porous material, it can be modeled as poroelastic under appropriate conditions. In the theory of poroelasticity, a small control volume is considered, which is large enough to encompass the size of pores yet small enough to be regarded as an infinitesimally small element. The symbol σ_{ij} denotes the stress acting on the surface of the control volume, while the macroscopic stain ϵ_{ij} is the infinitesimally small strain in solid. The variables p and ζ correspond to the equilibrium pore fluid pressure and mass of pore fluid per unit reference volume, respectively. Accordingly, the governing equations for the poroelastic bone are as follows (157):

$$2G\epsilon_{ij} = \sigma_{ij} - \left(\frac{\nu}{\nu+1}\right)\sigma_{ij}\delta_{ij} + \alpha\left(\frac{1-2\nu}{1+\nu}\right)p\delta_{ij}$$
 (A3)

$$2G\zeta = \alpha \left(\frac{1 - 2\nu}{1 + \nu}\right) \left(\sigma_{kk} + \frac{3p}{B}\right) \tag{A4}$$

where Shear modulus (G), passion ratio (ν) , Willis coefficient (α) , and Skemton's coefficient (B) are four independent material constants. In addition, Willis coefficient (α) and Skemton's coefficient (B) are related to K_S (bulk modulus of solid) and K_f (bulk modulus of fluid) as follows.

$$\alpha = 1 - \frac{K}{K_s} \tag{A5}$$

$$B = \frac{\frac{1}{K} - \frac{1}{K_s'}}{\frac{1}{K_f} + \frac{1}{K} - \frac{1}{K_s'} - \frac{v_0}{K_s''}}$$
(A6)

Under appropriate conditions $K_s' = K_s'' = K_s$ (157).

The constitutive Eq. A3 and A4 are completed by introducing Darcy's law, which governs the flow of fluid through a porous medium and is given by

$$q_i = -\kappa \frac{\partial p}{\partial x_i} \tag{A7}$$

where q_i is the fluid mass flow rate, κ is the hydraulic permeability ($\kappa = \frac{k}{\mu}$, where k is the intrinsic permeability and μ is the fluid's dynamic viscosity). The unit of intrinsic permeability is length square, and it is only a function of the porous structure, not the fluid inside it.

We Consider the same example as that in Fig. A1a (1D bar supporting a load $\sigma_z = -p_0$). However, this time, the bar is poroelastic. It is also assumed that only the top surface is permeable, i.e., no fluid can escape through the lateral and the bottom surfaces, while fluid can escape from the top surface. The governing Eq. A3, A4, and A7 can be simplified for the 1D poroelastic bar as follows (130):

$$\frac{1}{a}\frac{\partial^2 w}{\partial z^2} - \alpha \frac{\partial p}{\partial z} = 0 \tag{A8}$$

$$k\frac{\partial^2 p}{\partial z^2} = \alpha \frac{\partial^2 w}{\partial z \partial t} + \frac{1}{Q} \frac{\partial p}{\partial t}$$
 (A9)

$$\sigma_z = \frac{\varepsilon_z}{a} - \alpha p \tag{A10}$$

$$\theta = \alpha \Delta + \frac{p}{Q} \tag{A11}$$

where w is the displacement in the z-direction, p is the pore pressure, Δ is the volumetric strain, and a, α , and Q are the material constants.

Thus, the strain in the bar is given by

$$\varepsilon_{z} = \left[ap_{0} - \frac{4}{\pi^{2}} (a - a_{i}) p_{0} \sum_{0}^{\infty} \frac{1}{(2n+1)} e^{\left(-\left(\frac{(2n+1)\pi}{2h}\right)^{2} ct \right)} sin \frac{(2n+1)\pi z}{2h} \right]$$
 (A12)

Considering the simplest case, with n = 0, the above becomes:

$$\varepsilon_z = ap_0 \left[1 - \frac{4(a - a_i)}{\pi a} e^{-\left(\frac{\pi}{2h}\right)^2 ct} \right]$$
 (A13)

where $a_i = \frac{a}{1 - aQ\alpha^2}$.

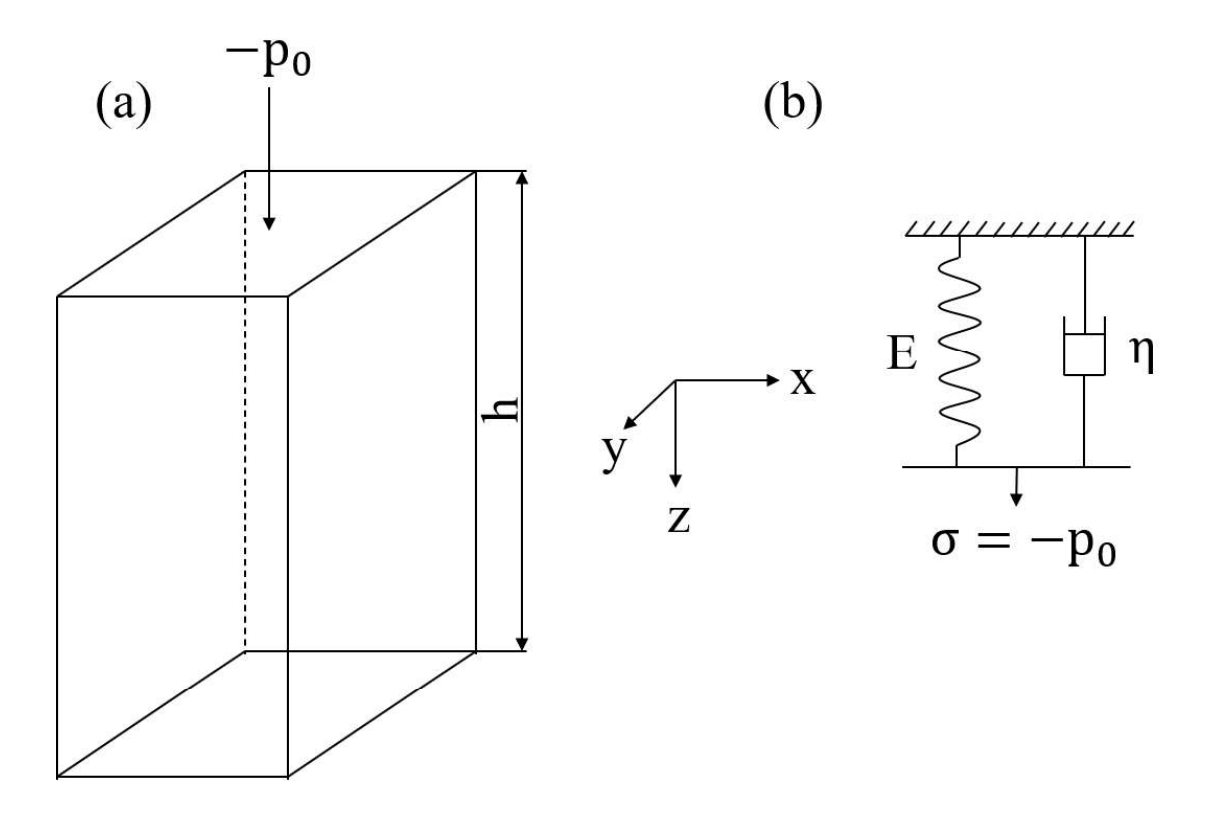


Figure A1 (a) Schematic diagram of the bar of height h supporting constant compressive stress and (b) the equivalent Kelvin-Voigt model considering the bar to be viscoelastic (E and η are the Young's modulus and viscosity of the material, respectively).

The similarity of Eq. A2 and A13 show that a fluid-filled tissue can be modeled either as a viscoelastic material or a poroelastic material, as both materials result in similar time-dependent strain responses to a step (constant) stress.

Accordingly, it can also be concluded that for a given cyclic loading condition, the energy dissipated at the tissue level will be the same regardless of whether the bone is considered viscoelastic or poroelastic.

References

- Maïmoun L, Fattal C, Micallef JP, Peruchon E, Rabischong P. Bone loss in spinal cordinjured patients: From physiopathology to therapy. *Spinal Cord* 44: 203–210, 2006. Doi: 10.1038/sj.sc.3101832.
- Vico L, Collet P, Guignandon A, Lafage-Proust MH, Thomas T, Rehailia M, Alexandre C. Effects of long-term microgravity exposure on cancellous and cortical weight-bearing bones of cosmonauts. *Lancet* 355: 1607–1611, 2000. doi: 10.1016/S0140-6736(00)02217-0.
- Rittweger J, Frost HM, Schiessl H, Ohshima H, Alkner B, Tesch P, Felsenberg D.
 Muscle atrophy and bone loss after 90 days' bed rest and the effects of flywheel resistive exercise and pamidronate: Results from the LTBR study. *Bone* 36: 1019–1029, 2005. doi: 10.1016/j.bone.2004.11.014.
- 4. Rittweger J, Simunic B, Bilancio G, Gaspare De Santo N, Cirillo M, Biolo G, Pisot R, Eiken O, Mekjavic IB, Narici M. Bone loss in the lower leg during 35 days of bed rest is predominantly from the cortical compartment. *Bone* 44: 612–618, 2009. doi: 10.1016/J.BONE.2009.01.001.
- Canalis E, Mazziotti G, Giustina A, Bilezikian JP. Glucocorticoid-induced osteoporosis: Pathophysiology and therapy. *Osteoporos Int* 18: 1319–1328, 2007. doi: 10.1007/s00198-007-0394-0.
- 6. Adami G, Saag KG. Glucocorticoid-induced osteoporosis: 2019 concise clinical review. *Osteoporos Int* 30: 1145–1156, 2019. doi: 10.1007/s00198-019-04906-x.
- LeBlanc A, Lin C, Shackelford L, Sinitsyn V, Evans H, Belichenko O, Schenkman B,
 Kozlovskaya I, Oganov V, Bakulin A, Hedrick T, Feeback D. Muscle volume, MRI
 relaxation times (T2), and body composition after spaceflight. *J Appl Physiol* 89: 2158–

- 2164, 2000. doi: 10.1152/jappl.2000.89.6.2158.
- Lang T, LeBlanc A, Evans H, Lu Y, Genant H, Yu A. Cortical and trabecular bone mineral loss from the spine and hip in long-duration spaceflight. *J Bone Miner Res* 19: 1006–1012, 2004. doi: 10.1359/JBMR.040307.
- 9. Biering-Sørensen F, Bohr HH, Schaadt OP. Longitudinal study of bone mineral content in the lumbar spine, the forearm and the lower extremities after spinal cord injury. *Eur J Clin Invest* 20: 330–335, 1990. doi: 10.1111/j.1365-2362.1990.tb01865.x.
- Dauty M, Perrouin Verbe B, Maugars Y, Dubois C, Mathe JF. Supralesional and sublesional bone mineral density in spinal cord-injured patients. *Bone* 27: 305–309, 2000. doi: 10.1016/S8756-3282(00)00326-4.
- Wilmet E, Ismail AA, Heilporn A, Welraeds D, Bergmann P. Longitudinal study of the bone mineral content and of soft tissue composition after spinal cord section. *Spinal Cord* 33: 674–677, 1995. doi: 10.1038/sc.1995.141.
- 12. Haapasalo H, Kontulainen S, Sievänen H, Kannus P, Järvinen M, Vuori I. Exercise-induced bone gain is due to enlargement in bone size without a change in volumetric bone density: A peripheral quantitative computed tomography study of the upper arms of male tennis players. *Bone* 27: 351–357, 2000. doi: 10.1016/S8756-3282(00)00331-8.
- 13. Warden SJ, Mantila Roosa SM, Kersh ME, Hurd AL, Fleisig GS, Pandy MG, Fuchs RK. Physical activity when young provides lifelong benefits to cortical bone size and strength in men. *Proc Natl Acad Sci U S A* 111: 5337–5342, 2014. doi: 10.1073/pnas.1321605111.
- Clarke B. Normal Bone Anatomy and Physiology. Clin J Am Soc Nephrol 3: S131–139,
 2008. doi: 10.2215/CJN.04151206.

- 15. Skedros JG, Holmes JL, Vajda EG, Bloebaum RD. Cement lines of secondary osteons in human bone are not mineral-deficient: New data in a historical perspective. *Anat Rec Part A Discov Mol Cell Evol Biol* 286: 781–803, 2005. doi: 10.1002/AR.A.20214.
- Mow VC, Ratcliffe A, Woo SL-Y. Biomechanics of Diarthrodial Joints. New York: Springer, 1990. doi: 10.1007/978-1-4612-3448-7.
- 17. Eriksen EF, Axelrod DW, Melsen F. Bone histomorphometry. New York: Raven Press, 1994, pp 1-12.
- Ito Y, Fitzsimmons JS, Sanyal A, Mello MA, Mukherjee N, O'driscoll SW. Localization of chondrocyte precursors in periosteum. *Osteoarthr Cartil* 9: 215–223, 2001. doi: 10.1053/JOCA.2000.0378.
- 19. Allen MR, Hock JM, Burr DB. Periosteum: biology, regulation, and response to osteoporosis therapies. *Bone* 35: 1003–1012, 2004. doi: 10.1016/J.BONE.2004.07.014.
- Islam A, Glomski C, Henderson ES. Endothelial cells and hematopoiesis: A light microscopic study of fetal, normal, and pathologic human bone marrow in plasticembedded sections. *Anat Rec* 233: 440–452, 1992. doi: 10.1002/ar.1092330311.
- 21. Buckwalter JA, Glimcher MJ, Cooper RR, Recker R. Bone biology. I: Structure, blood supply, cells, matrix, and mineralization. *Instr Course Lect* 45: 371–386, 1996.
- 22. Brodsky B, Persikov A V. Molecular structure of the collagen triple helix. *Adv Protein Chem* 70: 301–339, 2005. doi: 10.1016/S0065-3233(05)70009-7.
- 23. Boyce BF, Hughes DE, Wright KR, Xing L, Dai A. Recent advances in bone biology provide insight into the pathogenesis of bone diseases. *Lab Invest* 79: 83–94, 1999.
- 24. Crockett JC, Mellis DJ, Scott DI, Helfrich MH. New knowledge on critical osteoclast formation and activation pathways from study of rare genetic diseases of osteoclasts:

- focus on the RANK/RANKL axis. *Osteoporos Int* 22: 1–20, 2011. doi: 10.1007/S00198-010-1272-8.
- 25. Yavropoulou MP, Yovos JG. Osteoclastogenesis Current knowledge and future perspectives. *J Musculoskelet Neuronal Interact* 8: 204–216, 2008.
- 26. Sodek J, McKee MD. Molecular and cellular biology of alveolar bone. *Periodontol* 24: 99–126, 2000. doi: 10.1034/j.1600-0757.2000.2240106.x.
- 27. Matsumoto M, Kogawa M, Wada S, Takayanagi H, Tsujimoto M, Katayama S, Hisatake K, Nogi Y. Essential Role of p38 Mitogen-activated Protein Kinase in Cathepsin K Gene Expression during Osteoclastogenesis through Association of NFATc1 and PU.1. *J Biol Chem* 279: 45969–45979, 2004. doi: 10.1074/JBC.M408795200.
- 28. Boyce BF, Xing L. Functions of RANKL/RANK/OPG in bone modeling and remodeling. *Arch Biochem Biophys* 473: 139–146, 2008. doi: 10.1016/j.abb.2008.03.018.
- 29. Teitelbaum SL. Bone resorption by osteoclasts. *Science* 289: 1504–1508, 2000. doi: 10.1126/SCIENCE.289.5484.1504.
- 30. Mulari M, Vääräniemi J, Väänänen HK. Intracellular membrane trafficking in bone resorbing osteoclasts. *Microsc Res Tech* 61: 496–503, 2003. doi: 10.1002/jemt.10371.
- 31. Ducy P. Cbfa1: A Molecular Switch in Osteoblast Biology. *Dev Dyn* 219: 461–471, 2000. doi: 10.1002/1097-0177(2000)9999:9999<:::AID-DVDY1074>3.0.CO;2-C.
- 32. Bendall AJ, Abate-Shen C. Roles for Msx and Dlx homeoproteins in vertebrate development. *Gene* 247: 17–31, 2000. doi: 10.1016/S0378-1119(00)00081-0.
- Glass DA, Bialek P, Ahn JD, Starbuck M, Patel MS, Clevers H, Taketo MM, Long F,
 McMahon AP, Lang RA, Karsenty G. Canonical Wnt Signaling in Differentiated

- Osteoblasts Controls Osteoclast Differentiation. *Dev Cell* 8: 751–764, 2005. doi: 10.1016/J.DEVCEL.2005.02.017.
- 34. Nakashima K, Zhou X, Kunkel G, Zhang Z, Deng JM, Behringer RR, De Crombrugghe B. The novel zinc finger-containing transcription factor Osterix is required for osteoblast differentiation and bone formation. *Cell* 108: 17–29, 2002. doi: 10.1016/S0092-8674(01)00622-5.
- 35. Anderson HC. Matrix vesicles and calcification. *Curr Rheumatol Rep* 5: 222–226, 2003. doi: 10.1007/S11926-003-0071-Z.
- 36. Neuman WF, Neuman MW. The nature of the mineral phase of bone. *Chem Rev* 53: 1–45, 1953. doi: 10.1021/CR60164A001.
- 37. Schaffler MB, Cheung WY, Majeska R, Kennedy O. Osteocytes: Master Orchestrators of Bone. *Calcif Tissue Int* 94: 5–24, 2014. doi: 10.1007/S00223-013-9790-Y.
- 38. Feng JQ, Huang H, Lu Y, Ye L, Xie Y, Tsutsui TW, Kunieda T, Castranio T, Scott G, Bonewald LB, Mishina Y. The Dentin matrix protein 1 (Dmp1) is specifically expressed in mineralized, but not soft, tissues during development. *J Dent Res* 82: 776–780, 2003. doi: 10.1177/154405910308201003.
- 39. Nampei A, Hashimoto J, Hayashida K, Tsuboi H, Shi K, Tsuji I, Miyashita H, Yamada T, Matsukawa N, Matsumoto M, Morimoto S, Ogihara T, Ochi T, Yoshikawa H. Matrix extracellular phosphoglycoprotein (MEPE) is highly expressed in osteocytes in human bone. *J Bone Miner Metab* 22: 176–184, 2004. doi: 10.1007/S00774-003-0468-9.
- 40. Van Bezooijen RL, Roelen BAJ, Visser A, Van Der Wee-Pals L, De Wilt E, Karperien M, Hamersma H, Papapoulos SE, Ten Dijke P, Löwik CWGM. Sclerostin is an osteocyte-expressed negative regulator of bone formation, but not a classical BMP

- antagonist. J Exp Med 199: 805–814, 2004. doi: 10.1084/JEM.20031454.
- 41. Rochefort GY, Pallu S, Benhamou CL. Osteocyte: The unrecognized side of bone tissue.

 *Osteoporos Int 21: 1457–1469, 2010. doi: 10.1007/s00198-010-1194-5.
- 42. Dallas SL, Prideaux M, Bonewald LF. The Osteocyte: An Endocrine Cell ... and More. *Endocr Rev* 34: 658–690, 2013. doi: 10.1210/ER.2012-1026.
- 43. Cowin SC. Bone Mechanics Handbook. CRC Press, 2001. doi: doi.org/10.1201/b14263.
- 44. von Mayer GH. Die Architectur der Spongiosa. *Reichert und Du Bois-Reymond's Archiv*8: 615–628, 1867.
- 45. Thompson D. On growth and form. Bonner JT, Ed. Cambridge University Press 1961.
- Frost HM. Bone "mass" and the "mechanostat": A proposal. *Anat Rec* 219: 1–9, 1987.
 doi: 10.1002/ar.1092190104.
- 47. Lanyon LE, Rubin CT. Static vs dynamic loads as an influence on bone remodelling. *J Biomech* 17: 897–905, 1984. doi: 10.1016/0021-9290(84)90003-4.
- 48. Robling AG, Duijvelaar KM, Geevers J V., Ohashi N, Turner CH. Modulation of appositional and longitudinal bone growth in the rat ulna by applied static and dynamic force. *Bone* 29: 105–113, 2001. doi: 10.1016/S8756-3282(01)00488-4.
- 49. Toda H, Takata M, Ohgaki T, Kobayashi M, Kobayashi T, Uesugi K, Makii K, Aruga Y. 3-D image-based mechanical simulation of aluminium foams: Effects of internal microstructure. *Adv Eng Mater* 8: 459–467, 2006. doi: 10.1002/adem.200600035.
- 50. Rubin CT, McLeod KJ. Promotion of bony ingrowth by frequency-specific, low-amplitude mechanical strain. *Clin Orthop Relat Res* 298: 165–174, 1994. doi: 10.1097/00003086-199401000-00022.

- 51. Turner CH, Owan I, Takano Y. Mechanotransduction in bone: Role of strain rate. *Am J Physiol* 269: 438–442, 1995. doi: 10.1152/ajpendo.1995.269.3.e438.
- 52. Turner CH, Forwood MR, Otter MW. Mechanotransduction in bone: do bone cells act as sensors of fluid flow? *FASEB J* 8: 875–878, 1994. doi: 10.1096/fasebj.8.11.8070637.
- 53. Warden SJ, Turner CH. Mechanotransduction in the cortical bone is most efficient at loading frequencies of 5-10 Hz. *Bone* 34: 261–270, 2004. doi: 10.1016/j.bone.2003.11.011.
- 54. Turner CH. Three rules for bone adaptation to mechanical stimuli. *Bone* 23: 399–407, 1998. doi: 10.1016/S8756-3282(98)00118-5.
- 55. Hsieh YF, Turner CH. Effects of Loading Frequency on Mechanically Induced Bone Formation. *J Bone Miner Res* 16: 918–924, 2001. doi: 10.1359/JBMR.2001.16.5.918.
- 56. Rubin CT, Lanyon LE. Regulation of bone formation by applied dynamic loads. *J Bone Joint Surg Am.* 66: 511–513, 1984.
- 57. Umemura Y, Ishiko T, Yamauchi T, Kurono M, Mashiko S. Five jumps per day increase bone mass and breaking force in rats. *J Bone Miner Res* 12: 1480–1485, 2009. doi: 10.1359/jbmr.1997.12.9.1480.
- 58. Robling AG, Burr DB, Turner CH. Partitioning a daily mechanical stimulus into discrete loading bouts improves the osteogenic response to loading. *J Bone Miner Res* 15: 1596–1602, 2009. doi: 10.1359/jbmr.2000.15.8.1596.
- 59. Robling AG, Burr DB, Turner CH. Recovery periods restore mechanosensitivity to dynamically loaded bone. *J Exp Biol* 204: 3389–3399, 2001. doi: 10.1242/jeb.204.19.3389.
- 60. Srinivasan S, Gross TS. Intermittent rest enhances osteoblastic activation induced by

- mechanical loading. 46th Annual Meeting, Orthopaedic Research Society, March 12-15, 2000, Orlando, Florida.
- 61. You J, Yellowley CE, Donahue HJ, Zhang Y, Chen Q, Jacobs CR. Substrate Deformation Levels Associated With Routine Physical Activity Are Less Stimulatory to Bone Cells Relative to Loading-Induced Oscillatory Fluid Flow. *J Biomech Eng* 122: 387–393, 2000. doi: 10.1115/1.1287161.
- 62. Nicolella DP, Bonewald LF, Moravits DE, Lankford J. Measurement of microstructural strain in cortical bone. *Eur J Morphol* 42: 23–29, 2005. doi: 10.1080/09243860500095364.
- 63. Weinbaum S, Cowin SC, Zeng Y. A model for the excitation of osteocytes by mechanical loading-induced bone fluid shear stresses. *J Biomech* 27: 339–360, 1994. doi: 10.1016/0021-9290(94)90010-8.
- 64. You L, Cowin SC, Schaffler MB, Weinbaum S. A model for strain amplification in the actin cytoskeleton of osteocytes due to fluid drag on pericellular matrix. *J Biomech* 34: 1375–1386, 2001. doi: 10.1016/S0021-9290(01)00107-5.
- 65. Han Y, Cowin SC, Schaffler MB, Weinbaum S. Mechanotransduction and strain amplification in osteocyte cell processes. *Proc Natl Acad Sci U S A* 101: 16689–16694, 2004. doi: 10.1073/pnas.0407429101.
- 66. Wang Y, McNamara LM, Schaffler MB, Weinbaum S. A model for the role of integrins in flow induced mechanotransduction in osteocytes. *Proc Natl Acad Sci U S A* 104: 15941–15946, 2007. doi: 10.1073/pnas.0707246104.
- 67. You LD, Weinbaum S, Cowin SC, Schaffler MB. Ultrastructure of the osteocyte process and its pericellular matrix. *Anat Rec Part A Discov Mol Cell Evol Biol* 278A: 505–513,

- 2004. doi: 10.1002/AR.A.20050.
- 68. Burra S, Nicolella DP, Francis WL, Freitas CJ, Mueschke NJ, Poole K, Jiang JX. Dendritic processes of osteocytes are mechanotransducers that induce the opening of hemichannels. *Proc Natl Acad Sci U S A* 107: 13648–13653, 2010. doi: 10.1073/pnas.1009382107.
- 69. Hynes RO. Integrins: Versatility, modulation, and signaling in cell adhesion. *Cell* 69: 11–25, 1992. doi: 10.1016/0092-8674(92)90115-S.
- 70. Pavalko FM, Otey CA, Simon KO, Burridge K. α-Actinin: a direct link between actin and integrins. *Biochem Soc Trans* 19: 1065–1069, 1991. doi: 10.1042/BST0191065.
- Pavalko FM, Norvell SM, Burr DB, Turner CH, Duncan RL, Bidwell JP. A Model for mechanotransduction in bone cells: The load-bearing mechanosomes. *J Cell Biochem* 88: 104–112, 2003. doi: 10.1002/JCB.10284.
- 72. Hung CT, Allen FD, Pollack SR, Brighton CT. Intracellular Ca2+ stores and extracellular Ca2+ are required in the real-time Ca2+ response of bone cells experiencing fluid flow. *J Biomech* 29: 1411–1417, 1996. doi: 10.1016/0021-9290(96)84536-2.
- 73. Brambilla R, Abbracchio MP. Modulation of Cyclooxygenase-2 and Brain Reactive Astrogliosis by Purinergic P2 Receptors. *Ann N Y Acad Sci* 939: 54–62, 2001. doi: 10.1111/J.1749-6632.2001.TB03612.X.
- 74. Koolpe M, Pearson D, Benton HP. Expression of both P1 and P2 purine receptor genes by human articular chondrocytes and profile of ligand-mediated prostaglandin E2 release. *Arthritis Rheum* 42: 258–267, 1999. doi: 10.1002/1529-0131(199902)42:2<258::AID-ANR7>3.0.CO;2-O.

- 75. Chennimalai Kumar N, Dantzig JA, Jasiuk IM. Modeling of cortical bone adaptation in a rat ulna: Effect of frequency. *Bone* 50: 792–797, 2012. doi: 10.1016/j.bone.2011.12.008.
- Pereira AF, Javaheri B, Pitsillides AA, Shefelbine SJ. Predicting cortical bone adaptation to axial loading in the mouse tibia. *J R Soc Interface* 12: 20150590, 2015. doi: 10.1098/rsif.2015.0590.
- 77. Carriero A, Pereira AF, Wilson AJ, Castagno S, Javaheri B, Pitsillides AA, Marenzana M, Shefelbine SJ. Spatial relationship between bone formation and mechanical stimulus within cortical bone: Combining 3D fluorochrome mapping and poroelastic finite element modelling. *Bone Reports* 8: 72–80, 2018. doi: 10.1016/j.bonr.2018.02.003.
- 78. Prasad J, Goyal A. An Invertible Mathematical Model of Cortical Bone's Adaptation to Mechanical Loading. *Sci Rep* 9: 1–14, 2019. doi: 10.1038/s41598-019-42378-5.
- 79. Van Tol AF, Schemenz V, Wagermaier W, Roschger A, Razi H, Vitienes I, Fratzl P, Willie BM, Weinkamer R. The mechanoresponse of bone is closely related to the osteocyte lacunocanalicular network architecture. *Proc Natl Acad Sci U S A* 117: 32251–32259, 2020. doi: 10.1073/pnas.2011504117.
- 80. Iolascon G, Resmini G, Tarantino U. Mechanobiology of bone. In: *Aging Clin Exp Res* 25: 3–7. 2013. doi: 10.1007/s40520-013-0101-2.
- 81. Turner CH, Pavalko FM. Mechanotransduction and functional response of the skeleton to physical stress: The mechanisms and mechanics of bone adaptation. *J Orthop Sci* 3: 346–355, 1998. doi: 10.1007/s007760050064.
- 82. Tiwari AK, Prasad J. Computer modelling of bone's adaptation: the role of normal strain, shear strain and fluid flow. *Biomech Model Mechanobiol* 16: 395–410, 2017. doi:

- 10.1007/s10237-016-0824-z.
- 83. Kumar NC, Jaisuk T, Dantzig J. Dissipation energy as a stimulus for cortical bone adaptation. *Biomech Model Mechanobiol* 16: 303–319, 2011.
- 84. Singh S, Singh SJ, Prasad J. Investigating the Difference in Cortical Bone Adaptation at Endocortical and Periosteal Surfaces by Fluid Flow Analysis. *ASME Int Mech Eng Congr Expo Proc* 5, 2022. doi: 10.1115/IMECE2021-71220.
- 85. Murray DW, Rushton N. The effect of strain on bone cell prostaglandin E2 release: a new experimental method. *Calcif Tissue Int* 47: 35–39, 1990. doi: 10.1007/BF02555863.
- 86. Gardinier JD, Majumdar S, Duncan RL, Wang L. Cyclic hydraulic pressure and fluid flow differentially modulate cytoskeleton re-organization in MC3T3 osteoblasts. *Cell Mol Bioeng* 2: 133–143, 2009. doi: 10.1007/s12195-008-0038-2.
- 87. Lu XL, Huo B, Park M, Guo XE. Calcium response in osteocytic networks under steady and oscillatory fluid flow. *Bone* 51: 466–473, 2012. doi: 10.1016/J.BONE.2012.05.021.
- 88. Liu C, Zhao Y, Cheung WY, Gandhi R, Wang L, You L. Effects of cyclic hydraulic pressure on osteocytes. *Bone* 46: 1449–1456, 2010. doi: 10.1016/J.BONE.2010.02.006.
- 89. Takai E, Mauck RL, Hung CT, Guo XE. Osteocyte viability and regulation of osteoblast function in a 3D trabecular bone explant under dynamic hydrostatic pressure. *J Bone Miner Res* 19: 1403–1410, 2004. doi: 10.1359/JBMR.040516.
- 90. Parfitt AM, Drezner MK, Glorieux FH, John KA, Malluche H, Meunier PJ, Ott SM, Recker RR. Bone histomorphometry: Standardization of nomenclature, symbols and units. *J BONE Miner Res Vol* 2: 595–610, 1987.
- 91. Mano JF. Viscoelastic properties of bone: Mechanical spectroscopy studies on a chicken

- model. Mater Sci Eng C 25: 145–152, 2005. doi: 10.1016/j.msec.2005.01.017.
- 92. Gurtin ME, Fried E, Anand L. The Mechanics and Thermodynamics of Continua.

 Cambridge University Press, 2009.
- 93. Cho JR, Lee HW, Jeong WB, Jeong KM, Kim KW. Numerical estimation of rolling resistance and temperature distribution of 3-D periodic patterned tire. *Int J Solids Struct* 50: 86–96, 2013. doi: 10.1016/J.IJSOLSTR.2012.09.004.
- 94. Wolff J. Ueber die innere Architectur der Knochen und ihre Bedeutung für die Frage vom Knochenwachsthum. *Arch für Pathol Anat und Physiol und für Klin Med* 50: 389–450, 1870. doi: 10.1007/BF01944490.
- 95. Berman AG, Clauser CA, Wunderlin C, Hammond MA, Wallace JM. Structural and mechanical improvements to bone are strain dependent with axial compression of the tibia in female C57BL/6 mice. *PLoS One* 10: e0130504, 2015. doi: 10.1371/journal.pone.0130504.
- Roschger P, Misof B, Paschalis E, Fratzl P, Klaushofer K. Changes in the degree of mineralization with osteoporosis and its treatment. *Curr Osteoporos Rep* 12: 338–350, 2014. doi: 10.1007/s11914-014-0218-z.
- 97. Rubin CT, Lanyon LE. Regulation of bone mass by mechanical strain magnitude. *Calcif Tissue Int* 37: 411–417, 1985. doi: 10.1007/BF02553711.
- 98. Schulte FA, Ruffoni D, Lambers FM, Christen D, Webster DJ, Kuhn G, Müller R. Local Mechanical Stimuli Regulate Bone Formation and Resorption in Mice at the Tissue Level. *PLoS One* 8: e62172, 2013. doi: 10.1371/journal.pone.0062172.
- 99. Srinivasan S, Ausk BJ, Prasad J, Threet D, Bain SD, Richardson TS, Gross TS. Rescuing loading induced bone formation at senescence. *PLoS Comput Biol* 6: e1000924, 2010.

- doi: 10.1371/journal.pcbi.1000924.
- 100. Chennimalai NK, Dantzig JA, Jasiuk IM, Robling AG, Turner CH. Numerical modeling of long bone adaptation due to mechanical loading: Correlation with experiments. *Ann Biomed Eng* 38: 594–604, 2010. doi: 10.1007/s10439-009-9861-4.
- 101. Klein-Nulend J, Bakker AD, Bacabac RG, Vatsa A, Weinbaum S. Mechanosensation and transduction in osteocytes. *Bone* 54: 182–190, 2013. doi: 10.1016/j.bone.2012.10.013.
- 102. Huo B, Lu XL, Hung CT, Costa KD, Xu Q, Whitesides GM, Guo XE. Fluid Flow Induced Calcium Response in Bone Cell Network. *Cell Mol Bioeng* 1: 58–66, 2008. doi: 10.1007/s12195-008-0011-0.
- 103. Knothe Tate ML, Knothe U. An ex vivo model to study transport processes and fluid flow in loaded bone. *J Biomech* 33: 247–254, 2000. doi: 10.1016/S0021-9290(99)00143-8.
- 104. Willie BM, Birkhold AI, Razi H, Thiele T, Aido M, Kruck B, Schill A, Checa S, Main RP, Duda GN. Diminished response to in vivo mechanical loading in trabecular and not cortical bone in adulthood of female C57Bl/6 mice coincides with a reduction in deformation to load. *Bone* 55: 335–346, 2013. doi: 10.1016/j.bone.2013.04.023.
- 105. Birkhold AI, Razi H, Duda GN, Weinkamer R, Checa S, Willie BM. The Periosteal Bone Surface is Less Mechano-Responsive than the Endocortical. *Sci Rep* 6: 23480, 2016. doi: 10.1038/srep23480.
- 106. Weatherholt AM, Fuchs RK, Warden SJ. Cortical and trabecular bone adaptation to incremental load magnitudes using the mouse tibial axial compression loading model.
 Bone 52: 372–379, 2013. doi: 10.1016/j.bone.2012.10.026.

- Cowin SC. Bone poroelasticity. J Biomech 32: 217–238, 1999. doi: 10.1016/S0021-9290(98)00161-4.
- 108. Gailani G, Benalla M, Mahamud R, Cowin SC, Cardoso L. Experimental determination of the permeability in the lacunar-canalicular porosity of bone. *J Biomech Eng* 131: 101007, 2009. doi: 10.1115/1.3200908.
- 109. Lemaire T, Lemonnier S, Naili S. On the paradoxical determinations of the lacuno-canalicular permeability of bone. *Biomech Model Mechanobiol* 11: 933–946, 2012. doi: 10.1007/s10237-011-0363-6.
- 110. Smit TH, Huyghe JM, Cowin SC. Estimation of the poroelastic parameters of cortical bone. *J Biomech* 35: 829–835, 2002. doi: 10.1016/S0021-9290(02)00021-0.
- 111. Zhang D, Weinbaum S, Cowin SC. Estimates of the peak pressures in bone pore water. *J Biomech Eng* 120: 697–703, 1998. doi: 10.1115/1.2834881.
- 112. Gardinier JD, Townend CW, Jen KP, Wu Q, Duncan RL, Wang L. In situ permeability measurement of the mammalian lacunar-canalicular system. *Bone* 46: 1075–1081, 2010. doi: 10.1016/j.bone.2010.01.371
- 113. Zhou X, Novotny JE, Wang L. Modeling Fluorescence Recovery After Photobleaching in Loaded Bone: Potential Applications in Measuring Fluid and Solute Transport in the Osteocytic Lacunar-Canalicular System. *Ann Biomed Eng* 36: 1961–1977, 2008. doi: 10.1007/S10439-008-9566-0.
- 114. Evans SF, Parent JB, Lasko CE, Zhen X, Knothe UR, Lemaire T, Knothe Tate ML. Periosteum, bone's "smart" bounding membrane, exhibits direction-dependent permeability. *J Bone Miner Res* 28: 608–617, 2013. doi: 10.1002/jbmr.1777.
- 115. Li G, Bronk JT, An KN, Kelly PJ. Permeability of cortical bone of canine tibiae.

- Microvasc Res 34: 302–310, 1987. doi: 10.1016/0026-2862(87)90063-X.
- 116. Steck R, Niederer P, Knothe Tate ML. A finite element analysis for the prediction of load-induced fluid flow and mechanochemical transduction in bone. *J Theor Biol* 220: 249–259, 2003. doi: 10.1006/jtbi.2003.3163.
- 117. Price C, Zhou X, Li W, Wang L. Real-time measurement of solute transport within the lacunar-canalicular system of mechanically loaded bone: Direct evidence for load-induced fluid flow. *J Bone Miner Res* 26: 277–285, 2011. doi: 10.1002/jbmr.211.
- 118. Patel TK, Brodt MD, Silva MJ. Experimental and finite element analysis of strains induced by axial tibial compression in young-adult and old female C57Bl/6 mice. *J Biomech* 47: 451–457, 2014. doi: 10.1016/j.jbiomech.2013.10.052.
- 119. Zhang D, Cowin SC. Oscillatory bending of a poroelastic beam. *J Mech Phys Solids* 42: 1575–1599, 1994. doi: 10.1016/0022-5096(94)90088-4.
- 120. Palumbo C, Ferretti M, Marotti G. Osteocyte Dendrogenesis in Static and Dynamic Bone Formation: An Ultrastructural Study. *Anat Rec Part A Discov Mol Cell Evol Biol* 278: 474–480, 2004. doi: 10.1002/ar.a.20032.
- 121. Mullender MG, Huiskes R. Proposal for the regulatory mechanism of Wolff's law. *J Orthop Res* 13: 503–512, 1995. doi: 10.1002/JOR.1100130405.
- 122. WATSON GS. Goodness-of-fit tests on a circle. *Biometrika* 48: 109–114, 1961. doi: 10.1093/biomet/48.1-2.109.
- 123. Watson GS. Biometrika Trust Goodness-Of-Fit Tests on a Circle II. *Biometrika* 49: 57–63, 1962.
- 124. Scheiner S, Pivonka P, Hellmich C. Poromicromechanics reveals that physiological bone strains induce osteocyte-stimulating lacunar pressure. *Biomech Model*

- Mechanobiol 15: 9-28, 2016. doi: 10.1007/s10237-015-0704-y.
- 125. Cowin SC, Weinbaum S, Zeng Y. A case for bone canaliculi as the anatomical site of strain generated potentials. *J Biomech* 28: 1281–1297, 1995. doi: 10.1016/0021-9290(95)00058-P.
- 126. Klein-Nulend J, Van Der Plas A, Semeins CM, Ajubi NE, Frangos JA, Nijweide PJ, Burger EH. Sensitivity of osteocytes to biomechanical stress in vitro. *FASEB J* 9: 441–445, 1995. doi: 10.1096/fasebj.9.5.7896017.
- 127. Qin L, Liu W, Cao H, Xiao G. Molecular mechanosensors in osteocytes. *Bone Res* 8: 23, 2020. doi: 10.1038/s41413-020-0099-y.
- 128. Fritton SP, J. McLeod K, Rubin CT. Quantifying the strain history of bone: spatial uniformity and self-similarity of low-magnitude strains. *J Biomech* 33: 317–325, 2000. doi: 10.1016/S0021-9290(99)00210-9.
- 129. Liu C, Zhao Y, Cheung WY, Gandhi R, Wang L, You L. Effects of cyclic hydraulic pressure on osteocytes. *Bone* 46: 1449–1456, 2010. doi: 10.1016/j.bone.2010.02.006.
- Biot MA. General theory of three-dimensional consolidation. *J Appl Phys* 12: 155–164,
 1941. doi: 10.1063/1.1712886.
- 131. Kameo Y, Adachi T, Hojo M. Fluid pressure response in poroelastic materials subjected to cyclic loading. *J Mech Phys Solids* 57: 1815–1827, 2009. doi: 10.1016/j.jmps.2009.08.002.
- 132. Bratengeier C, Liszka A, Hoffman J, Bakker AD, Fahlgren A. High shear stress amplitude in combination with prolonged stimulus duration determine induction of osteoclast formation by hematopoietic progenitor cells. *FASEB J* 34: 3755–3772, 2020. doi: 10.1096/fj.201901458R.

- 133. Ethier CR, Simmons CA. Introductory Biomechanics: From Cells to Organisms.

 Cambridge University Press, 2012. doi: 10.2017/CBO9780511809217.
- 134. Sato M, Theret DP, Wheeler LT, Ohshima N, Nerem RM. Application of the Micropipette Technique to the Measurement of Cultured Porcine Aortic Endothelial Cell Viscoelastic Properties. *J Biomech Eng* 112: 263–268, 1990. doi: 10.1115/1.2891183.
- 135. Sansalone V, Kaiser J, Naili S, Lemaire T. Interstitial fluid flow within bone canaliculi and electro-chemo-mechanical features of the canalicular milieu: A multi-parametric sensitivity analysis. *Biomech Model Mechanobiol* 12: 533–553, 2013. doi: 10.1007/s10237-012-0422-7.
- 136. Bergula AP, Huang W, Frangos JA. Femoral vein ligation increases bone mass in the hindlimb suspended rat. *Bone* 24: 171–177, 1999. doi: 10.1016/S8756-3282(98)00165-3.
- 137. Sanchez-Ricart L, Garcia-Pelaez J. Viscous dissipative power density function for poroelastic saturated materials at high frequencies. *Mech Mater* 73: 11–27, 2014. doi: 10.1016/j.mechmat.2013.07.001.
- 138. Hamby DM. A review of techniques for parameter sensitivity analysis of environmental models. *Environ Monit Assess* 32: 135–154, 1994. doi: 10.1007/BF00547132.
- 139. De Souza RL, Matsuura M, Eckstein F, Rawlinson SCF, Lanyon LE, Pitsillides AA. Non-invasive axial loading of mouse tibiae increases cortical bone formation and modifies trabecular organization: A new model to study cortical and cancellous compartments in a single loaded element. *Bone* 37: 810–818, 2005. doi: 10.1016/j.bone.2005.07.022.
- 140. Carter DR, Fyhrie DP, Whalen RT. Trabecular bone density and loading history:

- Regulation of connective tissue biology by mechanical energy. *J Biomech* 20: 785–794, 1987. doi: 10.1016/0021-9290(87)90058-3.
- 141. Gorski JP. Is all bone the same? Distinctive distributions and properties of non-collagenous matrix proteins in Lamellar vs. Woven bone imply the existence of different underlying osteogenic mechanisms. *Crit Rev Oral Biol Med* 9: 201–223, 1998. doi: 10.1177/10454411980090020401.
- 142. Goyal A, Prasad J. An in silico model for woven bone adaptation to heavy loading conditions in murine tibia. *Biomech Model Mechanobiol* 21: 1425–1440, 2022. doi: 10.1007/s10237-022-01599-w.
- 143. Sugiyama T, Meakin LB, Browne WJ, Galea GL, Price JS, Lanyon LE. Bones' adaptive response to mechanical loading is essentially linear between the low strains associated with disuse and the high strains associated with the lamellar/woven bone transition. *J. Bone Miner. Res.* 27: 1784–1793, 2012. doi: 10.1002/jbmr.1599.
- 144. Gatti V, Azoulay EM, Fritton SP. Microstructural changes associated with osteoporosis negatively affect loading-induced fluid flow around osteocytes in cortical bone. *J Biomech* 66: 127–136, 2018. doi: 10.1016/j.jbiomech.2017.11.011.
- 145. Genthial R, Beaurepaire E, Schanne-Klein MC, Peyrin F, Farlay D, Olivier C, Bala Y, Boivin G, Vial JC, Débarre D, Gourrier A. Label-free imaging of bone multiscale porosity and interfaces using third-harmonic generation microscopy. *Sci Rep* 7: 3419, 2017. doi: 10.1038/s41598-017-03548-5.
- 146. Repp F, Kollmannsberger P, Roschger A, Kerschnitzki M, Berzlanovich A, Gruber G, Roschger P, Wagermaier W, Weinkamer R. Spatial heterogeneity in the canalicular density of the osteocyte network in human osteons. *Bone Reports* 6: 101–108, 2017. doi: 10.1016/j.bonr.2017.03.001.

- 147. Akhter MP, Raab DM, Turner CH, Kimmel DB, Recker RR. Characterization of in vivo strain in the rat tibia during external application of a four-point bending load. *J Biomech* 25: 1241–1246, 1992. doi: 10.1016/0021-9290(92)90082-C.
- 148. Knothe Tate ML, Steck R, Anderson EJ. Bone as an inspiration for a novel class of mechanoactive materials. *Biomaterials* 30: 133–140, 2009. doi: 10.1016/J.BIOMATERIALS.2008.09.028.
- 149. Duncan RL, Turner CH. Mechanotransduction and the functional response of bone to mechanical strain. *Calcif Tissue Int* 57: 344–358, 1995. doi: 10.1007/BF00302070.
- 150. Srinivasan S, Ausk BJ, Poliachik SL, Warner SE, Richardson TS, Gross TS. Rest-inserted loading rapidly amplifies the response of bone to small increases in strain and load cycles. *J Appl Physiol* 102: 1945–1952, 2007. doi: 10.1152/japplphysiol.00507.2006.
- 151. Canè V, Marotti G, Volpi G, Zaffe D, Palazzini S, Remaggi F, Muglia MA. Size and density of osteocyte lacunae in different regions of long bones. *Calcif Tissue Int* 34: 558–563, 1982. doi: 10.1007/BF02411304.
- 152. Srinivasan S, Gross TS. Canalicular fluid flow induced by bending of a long bone. *Med Eng Phys* 22: 127–133, 2000. doi: 10.1016/S1350-4533(00)00021-7.
- 153. Wang L, Fritton SP, Cowin SC, Weinbaum S. Fluid pressure relaxation depends upon osteonal microstructure: Modeling an oscillatory bending experiment. *J Biomech* 32: 663–672, 1999. doi: 10.1016/S0021-9290(99)00059-7.
- 154. Sibonga J, Matsumoto T, Jones J, Shapiro J, Lang T, Shackelford L, Smith SM, Young M, Keyak J, Kohri K, Ohshima H, Spector E, LeBlanc A. Resistive exercise in astronauts on prolonged spaceflights provides partial protection against spaceflight-

- induced bone loss. *Bone* 128: 112037, 2019. doi: 10.1016/j.bone.2019.07.013.
- 155. Kunkel CF, Scremin AM, Eisenberg B, Garcia JF, Roberts S, Martinez S. Effect of "standing" on spasticity, contracture, and osteoporosis in paralyzed males. *Arch Phys Med Rehabil* 74: 73–78, 1993.
- 156. Klose KJ, Jacobs PL, Broton JG, Guest RS, Needham-Shropshire BM, Lebwohl N, Nash MS, Green BA. Evaluation of a training program for persons with SCI Paraplegia using the Parastep®1 ambulation system: Part 1. Ambulation performance and anthropometric measures. *Arch Phys Med Rehabil* 78: 789–793, 1997. doi: 10.1016/S0003-9993(97)90188-X.
- 157. Rice JR, Cleary MP. Some Basic Stress Diffusion Solutions for Fluid-Saturated Elastic Porous Media With Compressible Constituents. *Rev. Geophys. Sp. Physic* 14: 227–241, 1976. doi: 10.1029/RG014i002p00227.